DISSERTATION

AN EXAMINATION OF THE LARGE-SCALE DRIVERS OF NORTH ATLANTIC VERTICAL WIND SHEAR AND SEASONAL TROPICAL CYCLONE VARIABILITY

Submitted by

Jhordanne J. Jones

Department of Atmospheric Science

In partial fulfillment of the requirements

For the Degree of Doctor of Philosophy

Colorado State University

Fort Collins, Colorado

Fall 2021

Doctoral Committee:

Advisor: Michael M. Bell
Co-Advisor: Philip J. Klotzbach

Elizabeth A. Barnes
Eric D. Maloney
Gregory L. Florant

ABSTRACT

AN EXAMINATION OF THE LARGE-SCALE DRIVERS OF NORTH ATLANTIC VERTICAL WIND SHEAR AND SEASONAL TROPICAL CYCLONE VARIABILITY

This dissertation characterizes and examines the large-scale sources of variability driving tropical North Atlantic deep-layer vertical wind shear (VWS). VWS is a key variable for the seasonal prediction of tropical cyclone (TC) activity and can be used to assess sources of predictability within a given season. Part 1 of the dissertation examines tropical versus subtropical impacts on TC activity by considering large-scale influences on boreal summer tropical zonal VWS variability, a key predictor of seasonal TC activity. Through an empirical orthogonal function analysis, I show that subtropical anticyclonic wave breaking (AWB) activity drives the second mode of variability in tropical zonal VWS, while El Niño-Southern Oscillation (ENSO) primarily drives the leading mode of tropical zonal VWS variability. Linear regressions of the four leading principal components against tropical North Atlantic zonal VWS and accumulated cyclone energy show that, while the leading mode holds much of the regression strength, some improvement can be achieved with the addition of the second and third modes. Furthermore, an index of AWB-associated VWS anomalies, a proxy for AWB impacts on the large-scale environment, may be a better indicator of summertime VWS anomalies. The utilization of this index may be used to better understand AWB's contribution to seasonal TC activity.

Part 2 shows that predictors representing the environmental impacts of subtropical AWB on seasonal TC activity improve the skill of extended-range seasonal forecasts of TC activity. There is a significant correlation between boreal winter and boreal summer AWB activity via AWB-forced phases of the quasi-stationary North Atlantic Oscillation (NAO). Years with above-normal boreal summer AWB activity over the North Atlantic region also show above-normal AWB activity in the preceding boreal winter that forces a positive phase of the NAO that persists through the

spring. These conditions are sustained by continued AWB throughout the year, particularly when ENSO plays less of a role at forcing the large-scale circulation. While individual AWB events are synoptic and nonlinear with little predictability beyond 8-10 days, the strong dynamical connection between winter and summer wave breaking lends enough persistence to AWB activity to allow for predictability of its potential impacts on TC activity. We find that the winter-summer relationship improves the skill of extended-range seasonal forecasts from as early as an April lead time, particularly for years when wave breaking has played a crucial role in suppressing TC development.

Part 3 characterizes VWS variability within the Community Earth System Model version 1 Large Ensemble (CESM1-LE). The 35 historical runs of the CESM1-LE provide substantially larger samples of the environment and various large-scale drivers than the ERA5 reanalysis that spans 1979 to present. Firstly, ENSO is shown to be the leading mode of tropical Atlantic variability and explains most, if not all, of the structured variance. Secondly, while the CESM1-LE shows robust physical representations of known climate phenomena, their relationships with tropical Atlantic VWS remain marginal except for ENSO. Eigenanalysis applied to the CESM1-LE shows that the principal components are ill-defined and gives no distinct pattern for non-ENSO associated large-scale drivers. Thirdly, composite analyses show that despite the narrow range of VWS variability associated with non-ENSO large-scale drivers, their individual contribution to VWS is noticeably stronger during ENSO-neutral conditions as represented by the large ensemble.

ACKNOWLEDGEMENTS

I would first like to thank my advisors Dr. Michael Bell and Dr. Philip Klotzbach for being great mentors and trusting me with media interviews. Not only did you take a chance on a scientist from the Caribbean, you gave me an opportunity to learn so much from you both. I've taken part in a field campaign, spent three incredible weeks at sea, visited places I've never been before, and contributed to seasonal forecasts for the entire Atlantic basin. I'd say that's a PhD experience! Thank you to my committee members Dr. Elizabeth Barnes, Dr. Eric Maloney and Dr. Gregory Florant for taking the time to serve on my PhD committee and for your guidance and feedback.

Thank you to the current and previous members of the Bell Research Group - to Chelsea, Bruno, Naufal, Ellie, Ting Yu, Rung, Jon, Ben, Ali, Alex, Dan Dan, Ya Chien, Jen, Kate, and Brianna. With such a diverse, supportive and close-knit group of people, the past four years of this PhD program were fun and memorable. Also, special thanks to the Department of Atmospheric Science for always providing me with a supportive haven for study. It has been my absolute honor and delight to learn from an amazing group of professors, students, research scientists, and professionals.

And to my biggest supporters and cheerleaders: to my father Donald, my mother Juliet, and my sister Ashley. This has been one of the longest journeys I've been on and your love and support have kept me going. You have been my greatest source of strength even from miles away. Thank you for staying up with me even with a time difference, for countless telephone calls, and for messaging me everyday for the last four years.

This dissertation was sponsored by the Fulbright Foreign Student Program, the Office of Naval Research (ONR) Award N000141613033, and the G. Unger Vetlesen Foundation. Data used in the analsyses presented here are publically available via the National Center for Atmospheric Research (NCAR) Climate Data Gateway (https://www.earthsystemgrid.org/) and the European Centre for Medium-Range Weather Forecasts (ECMWF) Climate Data Store (https://cds.climate.copernicus.eu/).

DEDICATION

This dissertation is dedicated to my family: to Donald, Juliet and Ashley.

Thank you so much for your love and support, even when I'm miles away.

TABLE OF CONTENTS

LIST OF TABLES

LIST OF FIGURES

Chapter 1

Introduction

1.1 Motivation

Statistical seasonal outlooks are oftentimes the vanguard of tropical cyclone (TC) forecasts within a given year. They provide the first insights into an impending tropical cyclone season and its potential impact. These statistical hurricane outlooks are powerful tools as they leverage the predictability of the environment to determine the level of expected seasonal storm activity and showcase impressive extended-range forecast skill at lead times up to 3 months. Many statistical outlooks comprise simple predictors of atmospheric and oceanic parameters such as sea surface temperatures, trade winds, and sea level pressures associated with known large-scale atmospheric phenomena and drivers of the general circulation (Karnauskas and Li 2016; Klotzbach et al. 2017, 2020b).

While the skill of statistical forecast schemes have improved substantially over the course of a decade, there remain occasional forecast busts that expose the limitations in current forecast methods. Forecast busts do vary with seasonal outlooks, however, there have been common ones, such as the 2007 and 2013 North Atlantic hurricane seasons, across the major statistical outlooks from Tropical Storm Risk (TSR) in the United Kingdom, the National Oceanic and Atmospheric Administration (NOAA), and Colorado State University (CSU; Klotzbach et al. 2017). A review of the literature indicates that these busts may be due to aspects of large-scale dynamical forcing that remain unaccounted for in current outlooks, such as the forcing of the tropical environment by equatorward intrusions of dry midlatitude air or anticyclonic Rossby wave breaking (AWB; Zhang et al. 2016; Papin et al. 2020) or non-linear impacts on the large-scale circulation due to different flavors of El Niño-Southern Oscillation (ENSO; Chand et al. 2013; Patricola et al. 2018).

Examining these blindspots in environmental predictability is essential for the improvement of forecast schemes and accounting for busts in future forecasts.

A popular way of examining large-scale dynamical impacts on seasonal TC activity is to consider the variability of the deep-layer vertical wind shear (VWS), defined as the difference between the upper-atmospheric (200-hPa) and lower-atmospheric (850-hPa) wind fields. Deep-layer VWS is an important modulator of seasonal TC activity. TC activity tends to occur in regions and seasons of climatologically low VWS (Gray 1968). Figure 1.1 illustrates that the location of TC occurrence is collocated with regions of reduced VWS (in white), while sparser TC occurrence is associated with regions of high VWS (shaded and contoured). In regions of large environmental wind shear, the low-level and upper-level vortices of a developing TC are unable to properly align and strengthen as the strong shear forces them apart. In contrast, a moderately sheared environment is too weak to prevent the alignment of the TC vortex and may even help TC development by re-aligning the vortex in a process known as precession (Jones 1995). An environment with little to zero large-scale wind shear tend to have similar but less favorable impacts on TC activity as moderate shear (Nolan and McGauley 2012). Some shear (though not too much) is shown to be more favorable for TC activity, as wind shear aids the organization of deep convection around the TC vortex (Corbosiero and Molinari 2002, 2003; DeHart et al. 2014). Therefore, large shear magnitudes suppress TC activity by making the environment unfavorable for development, while smaller shear magnitudes indicate an environment favorable for enhanced TC activity.

Another reason supporting the usefulness of VWS is that its variability harbors much of the key environmental requirements for either enhanced or suppressed TC development. VWS is associated with variations in surface relative vorticity, low-level convergence, and upper-level divergence, variables which mark the ability of the environment to organize and sustain mid-level moisture and deep convection (Gray 1968). The shear is also directly influenced by i) low-level trade winds (westward-oriented surface winds) represented by the 850-hPa wind field, and ii) upper-level winds (represented by the 200-hPa wind field) that both control the convergence and divergence of wind flow that can either enhance or suppress TC formation. And while the use of the 200hPa and

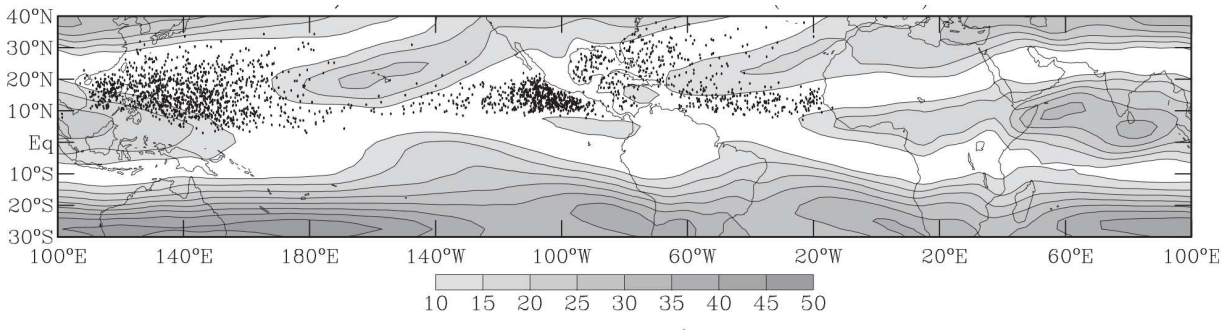

Figure 1.1: An overlay of mean 200-850-hPa VWS magnitude (m s^{-1}, shaded), and Pacific and Atlantic tropical cyclone genesis locations (black dots). Data is averaged over July-October for the period 1948-2004. Shaded regions indicate regions of large shear magnitudes. Sourced from Aiyyer and Thorncroft (2011).

850hPa wind fields in earlier works prior to reanalyses was due to these two levels being mandatory radiosonde reporting levels, these fields have proven to be exceptionally skillful at simulating the overall evolution of the tropical circulation. These two levels have been used extensively in later works to examine the effect of large-scale dynamical forcing on the local environment and TC activity. Studies that question the use of the 200-hPa and 850-hPa wind fields have found little change in modeling the dynamic impact of VWS on TC activity (Velden and Sears 2014; Rios-Berrios and Torn 2017). In the sections to follow, we focus our attention on VWS variability in the tropical North Atlantic region.

1.2 Large-scale VWS variability

Many studies have used VWS to examine the response of the atmosphere to dynamical drivers such as ENSO (Goldenberg and Shapiro 1996), African Sahel rainfall variability (Aiyyer and Thorncroft 2006), Rossby wave breaking (Zhang et al. 2016, 2017), the Saharan Air Layer (Dunion 2011), and the Atlantic Meridional Mode (Vimont and Kossin 2007). Aiyyer and Thorncroft (2006) examined the impacts of two tropical drivers, ENSO and African Sahel precipitation, on tropical North Atlantic TC activity through their individual influences on July-October tropical 200-850hPa VWS. Their main finding was that the large-scale drivers of shear controlled very different patterns in space and time. The signals were isolated using two types of regressions: an empirical orthogonal function (EOF) analysis of global tropical VWS between 30^oS-30^oN, where

orthogonal and seemingly unrelated modes of variability were isolated by considering the maximum variance explained. The second method included was a least-squares linear regression against the 1958-2003 Niño-3 and Sahel rainfall indices to examine the patterns of VWS explained by each climate index. Both methods indicated that ENSO drives the greater portion of deep-layer VWS variability. Furthermore, the study highlighted that these large-scale drivers controlled shear in different regions within the North Atlantic basin. In a follow-up paper, ENSO was observed to control much of the interannual variability in VWS, while Sahel rainfall forced decadal variability in VWS (Aiyyer and Thorncroft 2011).

1.3 Subtropical drivers of tropical VWS

The impacts of tropical large-scale drivers on VWS, particularly ENSO, are well-documented in the scientific literature. Fewer studies have documented subtropical drivers of VWS. Dunion (2011) analyzed atmospheric soundings within the North Atlantic region only and found that the vertical profiles could be categorized into three distinct groups: tropical moist air, dry air originating from the midlatitudes or subtropics, and air originating from the Sahel. He confirmed the influence of tropical drivers like ENSO (tropical moist) and the Sahel on the Atlantic, but also indicated that the subtropics had a role to play in driving deep-layer VWS variability.

More recent studies of the seasonal TC environment also suggest subtropical contributions to the large-scale circulation. Zhang et al. (2016) examined the effect of anticyclonic Rossby wave breaking (AWB) variability on the 2013 tropical Atlantic environment, and found that it may have caused the anomalous drying and high vertical wind shear in August, thus suppressing TC activity. AWB produces potential vorticity intrusions that inject dry subtropical air into the moister tropical region. This exchange of moist tropical air and dry midlatitude air increases the deep-layer shear along the downstream edge of the breaking wave. The tropical North Atlantic region is defined here as the region equatorward of 30^{o}N. Zhang et al. (2017) and Papin (2017) further showed that AWB activity may have a consistent role in forcing shear and moisture within the tropical cyclone environment. Both studies showed strong relationships between AWB activity and environmental VWS, as well as TC activity.

A review of previous literature on AWB activity indicates that there is no consistent standard by which wave breaking may be detected. Different studies have utilized different wave breaking detection methods. Furthermore, while AWB activity has a strong correlation with TC activity through its modulation of deep-layer shear, it is unclear how influential AWB activity is against the strong driving force of ENSO.

1.4 ENSO-neutral VWS Variability

Many studies indicate that the evolution of ENSO is not always a linear one. While the peak or mature phase of an El Niño event can reasonably be expected to occur in the boreal winter (December-February), the timing and duration of an ENSO transition shows considerable irregularity (Larkin et al. 2002; Dommenget et al. 2013; Horii and Hanawa 2004). Several asymmetries (quasi-periodic or inconsistent variations) may be observed throughout the warm pool (defined as SST anomalies in the region 5^oS-5^oN and 160^oE-150^oW) and cold tongue ENSO (defined as SST anomalies in the region 5^oS-5^oN and 150^oW-90^oW) indices (Patricola et al. 2016). These asymmetries are more noticeable during ENSO's phase change (Larkin et al. 2002). Chand et al. (2013) indicates that ENSO-neutral may be further categorized into positive-neutral or negative-neutral conditions, and these two phases were shown to force Australian TC activity differently.

These findings may have implications for the driving of the large-scale circulation and TC activity during ENSO neutral conditions. These asymmetries, that are dependent on both location and timing of warming events, have been shown to drive significantly different patterns within both the large-scale circulation and TC activity (Chand et al. 2013; Ha et al. 2013).

1.5 Dissertation Objectives and Outline

In this dissertation, we examine VWS variability associated with subtropical drivers and ENSO-neutral phases, and explore the implications for TC predictability. The guiding hypothesis of this research is that by identifying and understanding the key large-scale drivers of deep-layer VWS, we will be able to assess the sources of predictability for the summertime large-scale environment

and consequently improve the forecast skill of seasonal TC activity. This dissertation attempts to address the following science questions:

1. What are the main drivers impacting tropical North Atlantic VWS?
2. Do subtropical drivers of tropical North Atlantic VWS improve the skill of current seasonal TC outlooks?
3. What large-scale drivers characterize VWS variability during ENSO-neutral conditions?

Chapter 2 examines via eigenanalysis the modes of variability characterizing summer tropical North Atlantic VWS from 1979-2016. The results of this study show that not only are there tropical large-scale drivers of VWS like El Niño-Southern Oscillation (ENSO) but subtropical drivers like subtropical Rossby wave breaking (RWB) are also a consistent feature at interannual and seasonal timescales. An index representing AWB impacts on shear is also created and is shown to add skill to simple linear regressions against accumulated cyclone energy (ACE) during the peak of the Atlantic hurricane season.

Chapter 3 examines the use of AWB-associated VWS outlined in Chapter 2 and the second leading mode of summer VWS variability as an additional predictor in a seasonal TC forecast scheme. A correlation analysis across seasonal environmental fields shows that summer AWB-associated shear has strong persistence within the zonal wind field. This persistence adds skill to an early-April extended-range statistical hurricane model.

Chapter 4 outlines an analysis of summer VWS variability within a global climate model (GCM) large ensemble. Leveraging the large sample size of the ensemble, the variability in tropical North Atlantic VWS under ENSO-neutral conditions is examined.

Chapter 5 provides a summary of the dissertation's findings and outlines its conclusions and implications for future work.

Chapter 2

Tropical versus Subtropical Large-scale Drivers of Tropical North Atlantic Vertical Wind Shear[1]

2.1 Introduction

While forecast schemes predicting North Atlantic basin seasonal tropical cyclone (TC) activity have skill (Klotzbach et al. 2017), there remain gaps in our current understanding of the large-scale mechanisms that influence overall activity within the ocean basin. A key influence on TC activity is vertical wind shear (VWS), which acts to disrupt the TC circulation and reduce overall activity (Nolan and McGauley 2012). Until recently, the scientific literature indicated that the drivers of VWS on seasonal time-scales were predominantly tropical in origin with El Niño-Southern Oscillation (ENSO) being one of the leading drivers of interannual zonal VWS variability within the tropical North Atlantic (Goldenberg and Shapiro 1996; Wang 2004; Aiyyer and Thorncroft 2006). However, extratropical sources of shear resulting from Rossby wave breaking (RWB) have recently been identified as an important dynamical influence on TC activity (Zhang et al. 2016; Papin et al. 2020). In this study, we examine the physical drivers of VWS variability in the tropical North Atlantic, with the aim of improving our understanding of both tropical and extratropical sources of VWS and their impacts on TC activity.

A common mechanism proposed for ENSO forcing of the Atlantic tropical circulation is through its modulation of the Walker circulation over the Pacific and North Atlantic basins (Wang 2004). Anomalously warm SSTs in the equatorial central and eastern Pacific associated with El Niño result in an eastward-shift of the Walker Circulation from the tropical western Pacific towards the

[1]The results outlined in Chapter 2 have been published in the *Journal of Climate*: Jones, J. J., M. M. Bell, and P. J. Klotzbach, 2020: Tropical and subtropical North Atlantic vertical wind shear and seasonal tropical cyclone activity. *J. Climate*, **33 (13)**, 5413–5426, https://doi.org/10.1175/JCLI-D-19-0474.1.

International Date Line with associated anomalous downdrafts over the tropical Atlantic. This shift produces anomalous westerly upper-level winds and an associated increase in westerly VWS that inhibits TC development across the tropical North Atlantic MDR (Gray 1984; Zhang et al. 2016, 2017), generally defined as the region between 10^oN-20^oN and 80^oW-20^oW. The reverse effect occurs with an anomalously cold equatorial central and eastern Pacific (e.g., La Niña).

Atlantic SST variability is also a major driver of tropical North Atlantic VWS (Chelliah and Bell 2004; Chiang and Vimont 2004; Kossin and Vimont 2007; Klotzbach and Gray 2008). The Atlantic Meridional Mode (AMM) is the leading dynamical mode in tropical Atlantic climate variability, identified from a maximum covariance analysis of Atlantic sea surface temperature (SST) and 10-m winds (Chiang and Vimont 2004). The AMM is known to drive both interannual and decadal variability of vertical wind shear through its modulation of meridional gradients in SSTs and subsequent shifts in the Inter-tropical Convergence Zone (ITCZ) and the Hadley circulation. A positive phase of the AMM is associated with an anomalously warm northern tropical Atlantic relative to the southern tropical Atlantic. When the AMM is positive, the ITCZ and ascending arm of the Hadley cell shifts further north, reducing upper-level westerly winds throughout the Atlantic MDR. With a negative phase of the AMM, the ascending branch of the Hadley circulation shifts further south, increasing upper-level westerlies and thus increasing westerly shear over the MDR.

In contrast to the tropical forcing of shear by ENSO and the AMM, the mid-latitude forcing arises primarily from RWB events characterized by an irreversible deformation of potential vorticity (PV) contours on an isentropic surface forced by a strong temperature or pressure gradient (McIntyre and Palmer 1983; Strong and Magnusdottir 2008; Papin et al. 2020). RWB events often result in the exchange of air between the drier midlatitudes and moister tropics via intrusions of equatorward high PV midlatitude tropospheric air and poleward low PV tropical air (Postel and Hitchman 1999). RWB activity also shows a strong inter-relationship with seasonal variations in both tropical North Atlantic VWS and TC activity (Papin et al. 2020; Zhang et al. 2017). Anticyclonic RWB (AWB) occurs more frequently in the summer than in the winter over the North Atlantic basin and has been examined in recent studies with a focus on Rossby wave breaking dy-

namics and their relationship with large-scale climate phenomena (Homeyer and Bowman 2013; Papin et al. 2020; Zhang et al. 2016, 2017; Zavadoff and Kirtman 2019).

Seasonal TC forecast verifications have previously highlighted the role of midlatitude interactions in suppressing TC development, such as the 2007 North Atlantic hurricane season (Klotzbach et al. 2007) and the 2013 hurricane season (Klotzbach and Gray 2013; Saunders and Lea 2014). Zhang et al. (2016) indicated that enhanced RWB frequency in 2013 was associated with strong VWS and reduced precipitable water within the North Atlantic MDR that effectively suppressed TC development. As with the 2007 hurricane season, strong suppression in 2013 occurred despite otherwise favorable environmental conditions, such as anomalously warm tropical Atlantic sea surface temperatures (SSTs) and a persistent ENSO-neutral phase (Klotzbach and Gray 2013). However, modulations in RWB-induced shear occur on much faster timescales than SST or ENSO, with RWB events and their impacts typically lasting no more than a couple of days (Li et al. 2018).

Another driver of VWS and TC variability within the tropical North Atlantic is atmospheric variability closely tied to African Sahel rainfall dynamics (Landsea and Gray 1992; Aiyyer and Thorncroft 2006). Earlier seasonal forecast schemes included African Sahel rainfall as a robust predictor of TC activity (Gray et al. 1994). While Sahelian rainfall variability and its impacts are not fully understood (e.g. Janicot et al. 1998, Janicot et al. 2001), it is generally held that Sahelian rainfall has a positive correlation with North Atlantic TC activity and a negative correlation with VWS (Landsea and Gray 1992). Enhanced convection over the Western Sahel results in upper-tropospheric easterly wind anomalies and a reduction of the climatological westerly shear within the NA region, promoting both TC development and intensification (Landsea and Gray 1992). Chelliah and Bell (2004) also suggest that VWS may be driven by a stationary wave response in the upper-level winds to anomalous heating from West African convection. Earlier work identified the effect of both ENSO and Sahel rainfall on the variability of the North Atlantic tropical circulation (Goldenberg and Shapiro 1996; Aiyyer and Thorncroft 2006) but did not fully explore extratropical influences on the variability. Dunion (2011) highlighted that midlatitude dry-air intrusions comprised a small but significant percentage of tropical North Atlantic atmospheric soundings and

suggested that dry-air intrusions from the subtropics were a persistent feature within the tropical circulation.

In the analysis that follows, we further examine the respective contributions of tropical and extratropical factors on tropical North Atlantic VWS variability. We examine the physical drivers of tropical VWS variability in the North Atlantic and propose a way of quantifying how much extratropical AWB activity contributes to seasonal VWS. We show that VWS anomalies associated with AWB explain a significant portion of tropical VWS variability and may lend another perspective to the predictability of the seasonal TC environment. The paper is organized as follows: Section 2.2 outlines the data and procedures used to characterize the different drivers of VWS variability. Section 2.3 characterizes mean spatial VWS variability in high versus low seasons of ENSO and RWB activity. Section 2.4 outlines the different spatial and temporal effects of tropical versus subtropical drivers of seasonal tropical VWS anomaly. Section 2.5 provides a discussion of the results outlined in Section 2.4 and summarizes the implications for improved seasonal predictions of North Atlantic TC activity.

2.2 Data and Methods

2.2.1 Data

All atmospheric field data employed in this study are sourced from the European Center for Medium-Range Weather Forecasts (ECMWF) ERA-Interim Reanalysis (Berrisford et al. 2011; Dee et al. 2011). Monthly fields are gridded with a resolution of 0.75^o x 0.75^o and extend from January 1979 to August 2019. Six-hourly datasets in which AWB-induced anomalies are identified are gridded with a resolution of 2.5^o x 2.5^o to remove small-scale disturbances (Postel and Hitchman 1999; Zhang et al. 2016; Papin et al. 2020). A lowpass-filtered version of the data that suppresses cycles less than four months is subtracted from the original data to remove signals on longer timescales, as suggested by Wang et al. (2010). The seasonal cycle is then removed by subtracting the 1981-2010 monthly climatology to obtain seasonal anomaly fields.

Monthly SST anomalies from 1982 to 2016 are derived from the National Oceanic and Atmospheric Administration's Optimum Interpolation Sea Surface Temperature version 2 (NOAA

OI-SSTv2) dataset (Reynolds et al. 2002). Monthly Sahel precipitation indices are taken from the Joint Institute of the Study of the Atmosphere and Ocean archive (JISAO; Mitchell 2013). The analysis regions over which the climate indices are averaged are outlined in Table 2.1.

Table 2.1: Regions used to define the four ENSO indices (Niño-1+2, Niño-3, Niño-3.4, and Niño-4), the African Sahel index, the anticyclonic Rossby wave breaking (AWB) index, the Atlantic Meridional Mode (AMM), and the Walker Circulation index. All indices are standardized relative to the 1981-2010 base period.

Index	Region	Reference
Niño-1+2	10^oS-0^o, 90^oW-80^oW	NOAA (2017)
Niño-3	5^oS-5^oN, 150^oW-90^oW	
Niño-3.4	5^oS-5^oN, 170^oW-120^oW	
Niño-4	5^oS-5^oN, 160^oE-150^oW	
Sahel	10^oN-20^oN, 20^oW-10^oE	Mitchell (2013)
AWB	20 ^{o}N-40^oN, 100^oW-5^oW	Zhang et al. (2016); Papin et al. (2020)
AMM	21 ^{o}S-32^oN, 74^oW-15^oE	Zhang et al. (2016); Chiang and Vimont (2004)
Walker Index	equatorial eastern Pacific: 5^oS-5^oN, 160^oW-120^oW equatorial western Pacific: 5^oS-5^oN, 120^oE-160^oE	Wang (2004)

Tropical North Atlantic VWS is defined here as the difference between the 200hPa and 850hPa zonal wind fields over the region 10^oN-30^oN and 90^oW-20^oW and are standardized over the period 1981-2010. We have chosen to use a domain larger than the canonical MDR to ensure that the impacts of large-scale drivers are fully captured within the spatiotemporal analysis, as will be discussed further in Sections 2.4 and 2.5. For this study, we only utilize the zonal component of VWS as much of the observed variability in VWS is zonally modulated (Thorncroft et al. 1993; Aiyyer and Thorncroft 2006; Nolan and McGauley 2012). Furthermore, changes in the circulation due to RWB are associated with variations in the strength and position of the subtropical upper-tropospheric westerly jet (Homeyer and Bowman 2013).

The Accumulated Cyclone Energy (ACE) index is used to represent overall seasonal TC activity and is defined as the sum of the squares of the six-hourly maximum wind speed for each tropical and sub-tropical cyclone where they at least possess one-minute maximum sustained winds of 34 knots (Bell et al. 2000). The ACE index from July-September was calculated from the National Hurricane Center's best track database (HURDAT2; Landsea and Franklin 2013). Note that we assessed VWS and AWB activity over the shorter July-September (JAS) season, in contrast to the overall hurricane season from June-November as in Papin et al. (2020) or July-October as in Zhang et al. (2017). We chose July-September, as both VWS and AWB activity show distinct summertime peaks during these months. To focus on the impacts of tropical VWS, only TCs that were named south of 35^oN were considered in the calculation of ACE.

2.2.2 Climate Indices

Table 2.1 presents the climate indices used to investigate the physical mechanisms driving the leading modes of tropical zonal VWS variability. Based on previous studies, for example Aiyyer and Thorncroft (2006), we analyze the correlations with indices representing ENSO, Sahelian rainfall, the AMM and AWB. Though the Walker Circulation is closely associated with ENSO in the tropical North Atlantic atmospheric circulation, we examine it as a separate index in order to determine the extent to which it is correlated with tropical zonal VWS variability. For Atlantic SST variability, Chiang and Vimont (2004)'s AMM index is applied. The AMM index is calculated using detrended and smoothed SSTs and low-level winds within the region 21^oS-32^oN and 74^oW-15^oE. Once ENSO variability is removed, a maximum covariance analysis is applied to obtain the AMM index. Chiang and Vimont (2004)'s method is used extensively within the scientific literature (Kossin and Vimont 2007; Vimont and Kossin 2007). The strength of the Pacific Walker cell is used as a proxy for the influence of the Walker circulation over the North Atlantic region and is defined as the difference between the 500hPa vertical velocity averaged over the equatorial eastern Pacific (5^oS-5^oN and 160^oW-120^oW) and the equatorial western Pacific (5^oS-5^oN and 120^oE-160^oE) (Wang 2004). All indices are standardized over 1981-2010, except for SST indices which are standardized over 1982-2010.

2.2.3 Detecting AWB

To detect AWB activity, we employ a simplified potential vorticity streamer (PVS) detection algorithm based on the technique outlined by Papin et al. (2020), where the PVS intensity index is calculated. AWB-associated PVSs are detected along the 2-PVU (1 PVU $\equiv 10^{-6}$ K m^2 s^{-1} kg^{-1}) contour in the 350-K potential vorticity field using the following steps:

- The algorithm detects more than two consecutive points along the 2-PVU contour with an eastward (west to east) PV gradient ($\frac{\partial PV}{\partial x} > 0$) and a reversal in the poleward meridional PV gradient ($\frac{\partial PV}{\partial y} < 0$). This defines the upstream edge of a PV tongue. Similarly, the downstream edge may be identified with conditions ($\frac{\partial PV}{\partial x} < 0$) and ($\frac{\partial PV}{\partial y} > 0$).

- Once the points outlining the PV tongue are identified, a line connects the two end points to capture the PVS polygon and as much of the PVS area as possible. We do not assess the PVS area for a perimeter distance threshold or 3:1 aspect ratio of PV tongues as is done by Papin et al. (2020). This may lead to slight differences in the results obtained in this study relative to Papin et al. (2020).

- The PVSI intensity is then found by calculating the standardized PV anomaly relative to a six-hourly climatological mean integrated across all grid points within the PVS polygon and then integrated over time.

- The VWS anomaly along both the upstream and downstream edges of the detected PV tongue are collected.

For the years 1979-2016, our detection algorithm finds 32, 014 AWB events in the ERA-Interim dataset. This is somewhat high compared with Papin et al. (2020)'s total of 21, 149 between 1979-2015. However, for the July-September focus of our study, the average number of events is 337, similar to **?**'s value of 355 for the same season. The climatology for the total number of PV streamers detected each month (not shown) is comparable to the climatological mean intensity of AWB activity over the North Atlantic region.

Papin et al. (2020) pointed out that the detection algorithms are sensitive not only to the reanalysis datatset used, but also to the method in which the PVS area is detected. The detection method and the PVS area captured varies across studies (Postel and Hitchman 1999; Abatzoglou and Magnusdottir 2006b; Wernli and Sprenger 2007; Barnes and Hartmann 2012; Kunz et al. 2015). However, the AWB climatology shown in Figure 2.1 is in good agreement with previous assessments of AWB variability over the North Atlantic region (Postel and Hitchman 1999; Abatzoglou and Magnusdottir 2006b; Papin et al. 2020; Zhang et al. 2017). The index also correlates positively with ENSO and negatively with North Atlantic ACE. There are some differences in the years detected with above-normal or below-normal AWB activity compared with the results of both Papin et al. (2020) and Zhang et al. (2017). The differences may be due to the season chosen for our assessment. The results also show a sensitivity to the domain chosen. Similar to Zhang et al. (2017), we restrict our detection region to 20^o-40^oN and 100^o-5^oW, where AWB is most frequent, to better quantify the effect of AWB activity on the tropical circulation. While Zhang et al. (2017) varies the northern boundary of the detection domain, we opt to set the northern boundary at 40^oN.

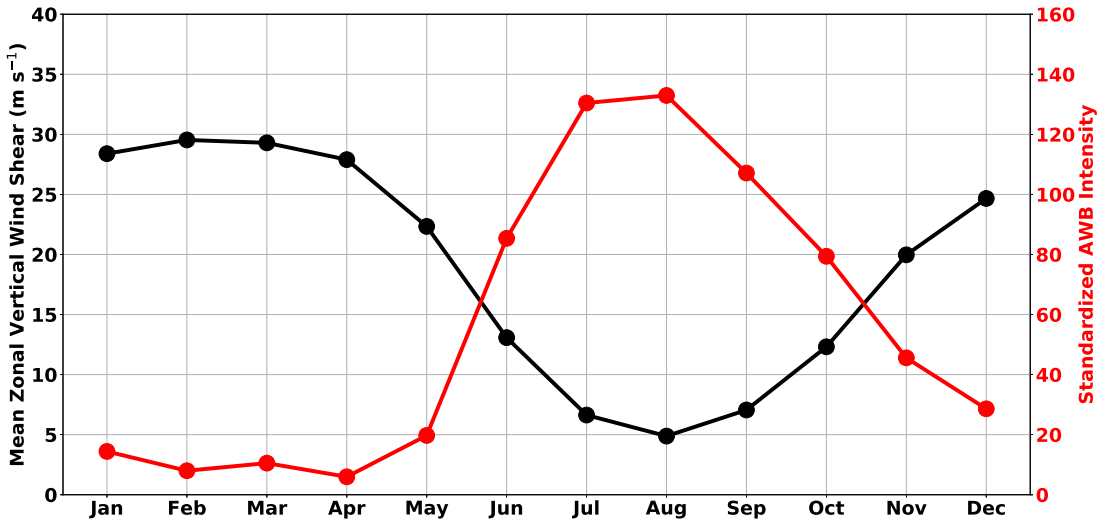

Figure 2.1: 1979-2016 monthly climatology of 200-850 hPa tropical North Atlantic zonal VWS (black) and North Atlantic AWB (red). AWB is calculated as the potential vorticity (PV) streamer intensity, in which the standardized PV anomaly is integrated over the area covered by the PV streamer (Papin et al. 2020).

2.2.4 EOF Analysis

To analyze the various modes of variability in tropical North Atlantic VWS, the leading empirical orthogonal functions (EOFs) are calculated via an eigenanalysis of the covariance matrix for July-September anomalous tropical North Atlantic VWS over the domain 10^o-30^oN and 90^o-20^oW. The VWS data is standardized prior to the EOF calculation; only the annual cycle is removed. The first four leading modes are retained for analysis as will be discussed in Section 2.4 and are regressed against global VWS anomalies to assess possible remote versus local forcing on tropical North Atlantic VWS. The Pearson correlation coefficients between the principal components derived from the EOF analysis and the climate indices outlined in Table 2.1 are calculated and used to assess how large-scale subtropical forcing differs from large-scale tropical forcing of tropical North Atlantic VWS.

2.3 VWS Composites of low versus high AWB years

2.3.1 VWS and AWB Climatology

Figure 2.1 shows a comparison of the 1979-2016 monthly climatology of mean zonal VWS and AWB activity over the tropical North Atlantic region. The VWS climatology (where positive values indicate westerly zonal shear and negative values indicate easterly zonal shear) exhibits maximum westerly shear in January-February. From March onwards, there is a steady decline in westerly shear in conjunction with the onset of the North Atlantic hurricane season in June. This westerly shear reaches its climatological minimum in July-September, as observed in previous studies of mean shear within the North Atlantic MDR (Gray 1968; Aiyyer and Thorncroft 2006). Figure Figure 2.2 shows a spatial plot of the 1979-2016 July-September mean zonal VWS across the Atlantic region. There is strong mean westerly shear cutting through the North Atlantic, stretching from the Caribbean northeast to the subtropical northeastern Atlantic. The strong westerly shear is flanked by strong easterly shear south of 10^oN and weaker westerly shear just north of 25^oN in the western subtropical North Atlantic, similar to the observations of Gray (1968) for the mean boreal summer shear.

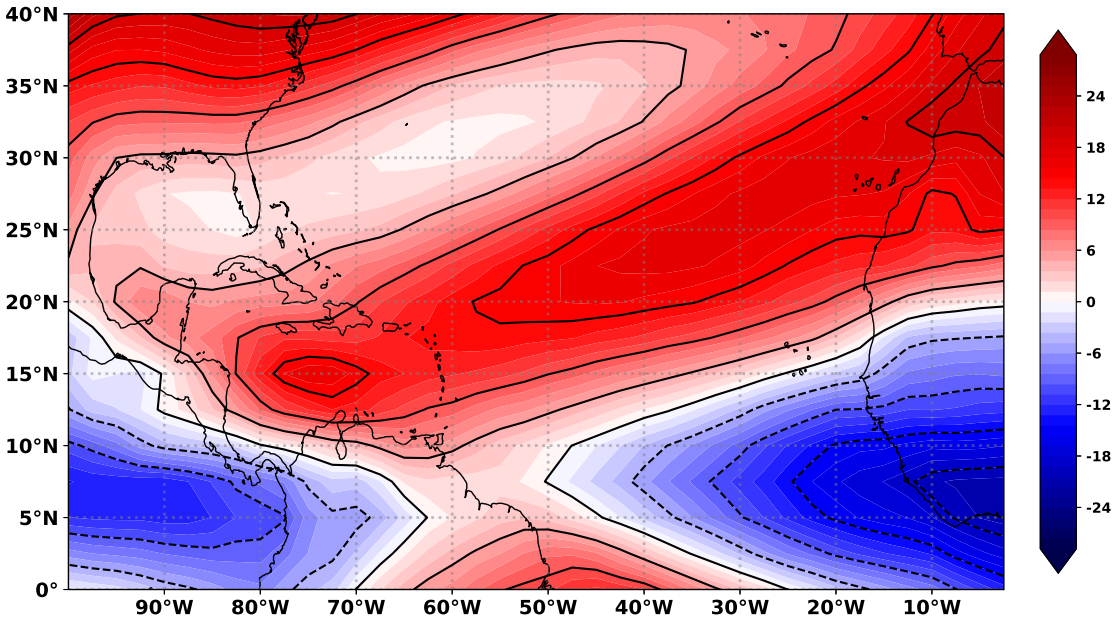

Figure 2.2: July-September 1979-2016 mean zonal 200-850 hPa VWS (in m s^{-1}); black contours indicate 4 m s^{-1} intervals.

Collocated with the peak weakening of westerly shear during July-September is a peak occurrence in North Atlantic AWB activity identified along the +2-PVU contour on the 350K isentrope. This is consistent with previous studies that identified peak anomalies on or around 350K (Postel and Hitchman 1999; Abatzoglou and Magnusdottir 2006b; Homeyer and Bowman 2013). Homeyer and Bowman (2013) and Kunz et al. (2015) further explained that equatorward AWB tends to occur in regions of weak mean westerly winds resulting from a weakening and a poleward shift of the subtropical jet over the North Atlantic. The increase in AWB activity is also collocated with mean northerly meridional shear (not shown).

In order to maximize the relationship with tropical VWS and subtropical AWB activity, we focus on the July-September season since this is when AWB shows a distinct peak. In the subsection below, we compare the dynamical variations in July-September VWS influenced by ENSO with variations associated with AWB activity.

2.3.2 Spatial variability in VWS composites

Figure 2.3 shows composites of July-September North Atlantic VWS anomalies in years associated with the 12 warmest El Niño events versus the 13 years with the most intense AWB activity (AWB(+)). For AWB, our choice of years are based on the PVSI index outlined in Section 2.2.3; the years chosen are consistent with those identified by Zhang et al. (2016) and Papin et al. (2020). During the warmest El Niño seasons (shown in Figure 2.3a), VWS is enhanced over the Atlantic MDR. A similar pattern in the VWS anomaly field is observed in years of intense AWB (Figure 2.3b). The difference between the composites (Figure 2.3c) shows that ENSO dominates tropical VWS variability. The most significant differences between AWB and ENSO on VWS (assessed using the Wilcoxon signed rank test) occur between 20^o-35^oN. The non-parametric Wilcoxon signed rank test categorizes the ranked differences between two time series into positive (W+) and negative (W-), and calculates the sum of each category. If the difference between the W+ and W- metrics are larger than the threshold corresponding to $\alpha = 0.05$, the null hypothesis that the differences are similar can be rejected (Wilks 2011).

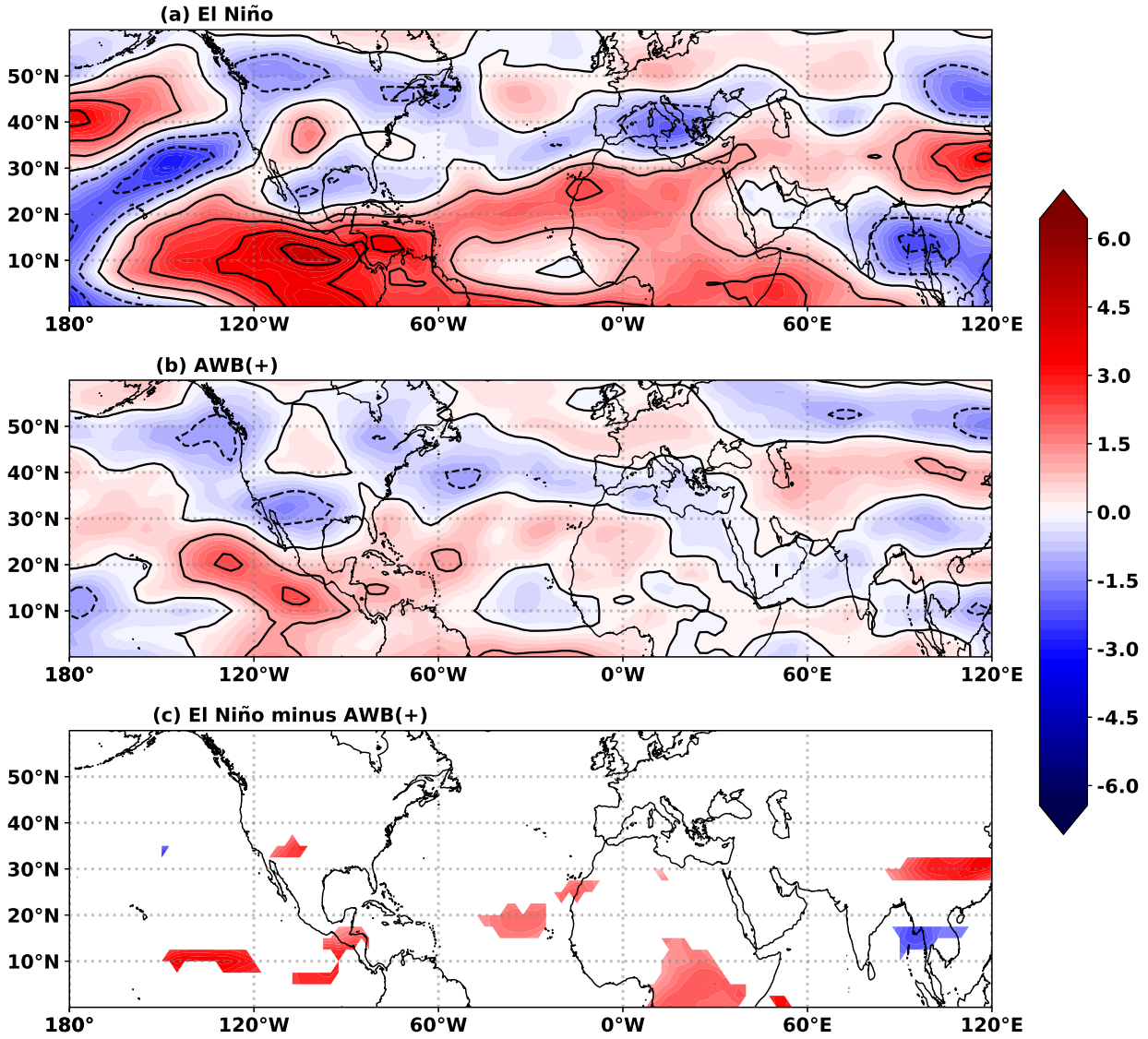

Figure 2.3: Comparison of the July-September zonal VWS composites in m s^{-1} for (a) the 12 warmest El Niño seasons vs (b) the 13 most active AWB seasons. Black contours indicate shear anomalies at 2 m s^{-1} intervals. Years used for the El Niño composite are 1982, 1986, 1987, 1990, 1991, 1993, 1994, 1997, 2002, 2004, 2009, and 2015; years used in the AWB(+) composite are 1982, 1985, 1986, 1993, 1994, 2000, 2001, 2003, 2007, 2009, 2011, 2013, and 2014.

Based on separate EOF analyses of mean July, August and September VWS anomalies, we find that both July and September have AWB patterns (similar to those for August) for their second leading monthly modes. This is consistent with the findings of Zhang et al. (2016) who conducted a similar EOF analysis for the North Atlantic environment in August. We further suggest that the effects of AWB on the Atlantic environment and consequently, TC activity, may also be observed not only in August but in July and September as well. The August composites (not shown) show similar features to the July-September composites, with a pronounced stretch of westerly shear associated with anomalously warm SSTs driven by El Niño. The anomalously strong subtropical jet stream, just north of the African Sahel, is also more evident in the August composites. However, there are few areas with significant differences between the August El Niño and AWB composites within the North Atlantic region.

In Figure 2.4, the shear anomaly composite for the 12 coldest La Niña years is compared with a composite of the 13 years with the least intense AWB activity. Figure 2.4 composites show a similar but opposite effect on VWS from those in Figure 2.3. As expected, there is very little difference between the La Niña and AWB(-) composites shown in Figure 2.4c. Unlike the El Niño-AWB(+) composites, the most significant vertical wind shear difference in the La Niña-AWB(-) composite occurs in the North Atlantic north of 35^{o}N.

There is a great deal of overlap between extreme ENSO seasons and AWB activity, as indicated by the years used to create the composites. Further attempts to separate the two effects indicate that the impacts of tropical and subtropical drivers are not completely separable due to strong tropical-subtropical teleconnections, for example, the AMM-NAO relationship (Grossmann and Klotzbach 2009). The VWS field minus the regressed influences of ENSO and the AMM show no significant correlation with the JAS PVSI index (not shown). Similarly, a frequency separation by applying a highpass filter on the frequency of days shows little evidence of the characteristic wave breaking pattern.

This suggests that the mechanisms of the two drivers are related, and that ENSO may drive part of AWB variability (Lau and Nath 1996; Martius et al. 2008) or that the effects of ENSO and

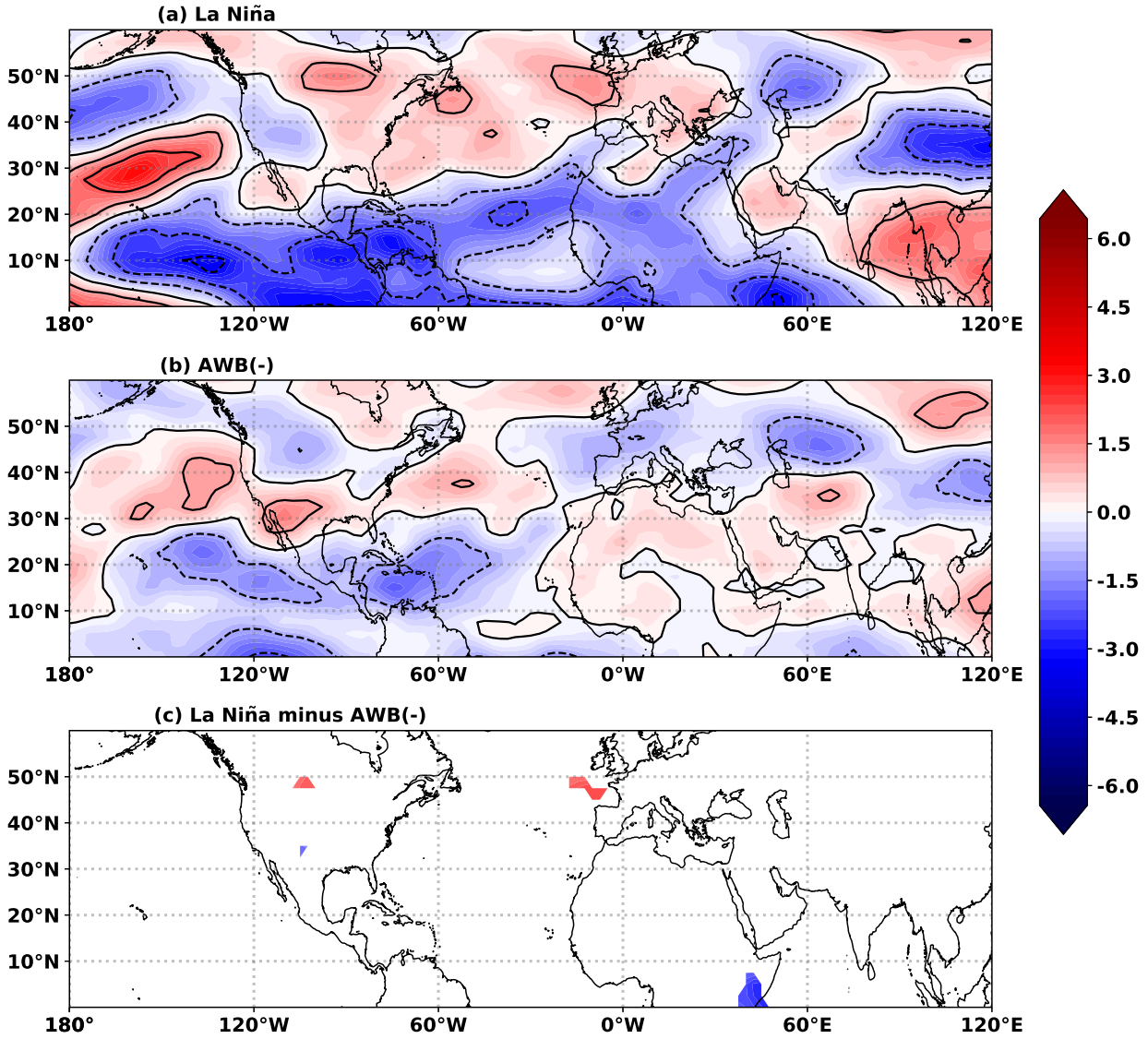

Figure 2.4: Comparison of the July-September zonal VWS composites in m s^{-1} for (a) the 11 coolest La Niña seasons vs (b) the 13 least active AWB seasons. Black contours indicate shear anomalies at 2 m s^{-1} intervals. Years used for the La Niña composite are 1985, 1988, 1995, 1998, 1999, 2000, 2007, 2010, 2011, 2013, and 2016; years used in the AWB(-) composite are 1981, 1987, 1989, 1995, 1997, 1998, 2002, 2004, 2005, 2008, 2010, 2012, and 2016.

its teleconnections partially overshadow the effects of other possible drivers. Our AWB activity index has a correlation of 0.14 with the Niño 3.4 index. Zhang et al. (2016) and Papin et al. (2020) showed a correlation of $\sim$ -0.3 between ENSO and AWB activity. While ENSO and AWB activity are not strongly correlated, ENSO dominates VWS variability and masks the effect of AWB on VWS anomalies in both Figures 2.3 and 2.4. Also, significant differences in the composites are observed within the Niño-4 region associated with warm-pool (WP) ENSO events (Ashok et al. 2007). This may suggest that WP ENSO has a role to play in driving North Atlantic AWB and its effects on tropical VWS. In Section 2.4, we discuss the results of an EOF analysis of mean tropical VWS anomalies to further explore the different effects of ENSO and AWB on VWS in the North Atlantic region. Note that for the remainder of the study, the abbreviation "EOF" refers to the spatial patterns of the leading modes observed in Figure 2.6, while "PC" refer to the principal components or temporal variations associated with each EOF mode, shown in Figure 2.7.

2.4 Eigenanalysis of tropical vertical wind shear

2.4.1 Eigenanalysis of tropical North Atlantic VWS anomaly

Figure 2.5 illustrates the variance explained by the first 20 EOFs of July-September tropical North Atlantic zonal VWS. Most of the structured variability in tropical VWS can be accounted for in the first two EOFs which together explain $\sim$59% of the explained variance. While EOFs 3 and 4 show some continuity with the tail end of the spectrum (explaining 12% and 8% of the variance, respectively), we believe that EOFs 3 and 4 are sufficiently separated from the remaining EOFs to have some physical significance in explaining VWS variability. Based on the criteria outlined by North et al. (1982), we opt to retain the first four EOFs that together account for 79% of the total variance in zonal VWS in the tropical North Atlantic.

Figure 2.6 shows a regression of the first four PCs onto July-September global zonal VWS anomalies. The first leading mode of variability (EOF1) shown in Fig. 2.6a accounts for 36% of the observed variance. The strongest spatial signal, that extends well outside the North Atlantic region, is mostly confined to the tropical belt and exhibits a tongue-like feature within the Niño-3 region reminiscent of the ENSO signal exhibited in Figs. 2.3a and 2.4a and the tropical interannual mode

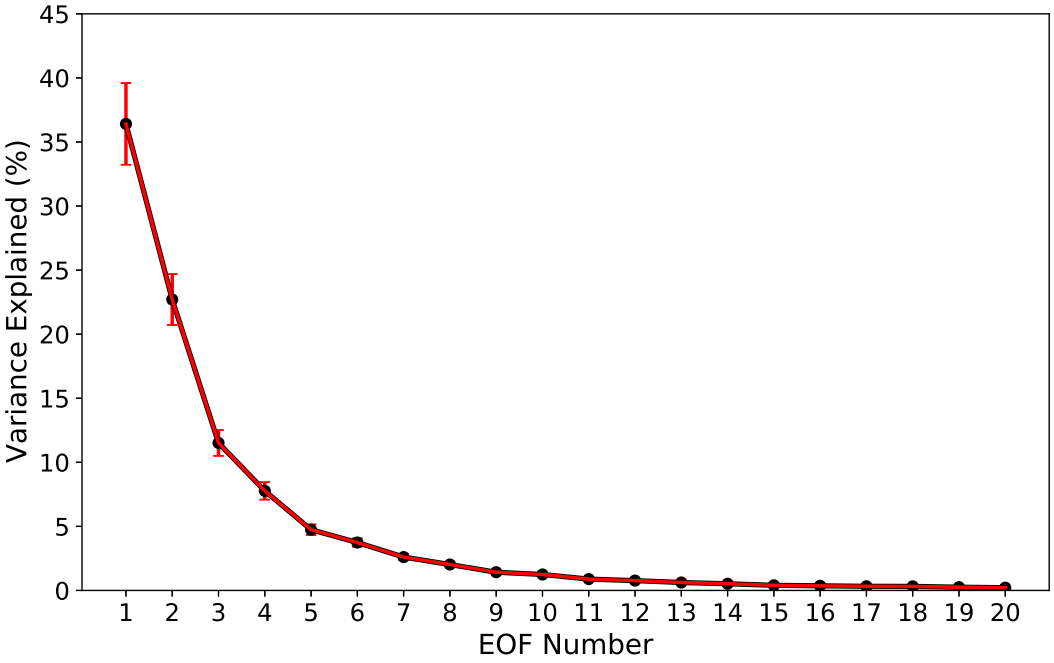

Figure 2.5: Spectrum of the covariance matrix showing the percentage variance explained by the first 20 EOFs with the bars representing the 95% error bounds for each EOF. The error distribution of each EOF is calculated using North et al. (1982)'s "rule of thumb."

examined in Chelliah and Bell (2004). Correlations with SST anomalies within the four ENSO regions indicate a strong association of temporal variations of EOF1 (PC1) with ENSO variations, as shown in Table 2.2. We note that PC1 shows a significant correlation with all indices used in the analyses. This may be due to PC1 accounting for most of the structured variance in tropical VWS. Variations in both the Walker Circulation and Sahel rainfall are known to have teleconnections with equatorial Pacific and Atlantic SST variability, as shown in Janicot et al. (1998, 2001). Of the four ENSO indices, the July-September Niño-3.4 index has the strongest correlation with PC1 (r = 0.73). PC1 also shows a significant correlation of r = -0.53 with the Atlantic Meridional Mode (AMM). Based on Fisher's r-to-z transformation (Lee and Preacher 2013), the correlation between Niño-3.4 and PC1 is significantly higher than the correlation between the AMM and PC1. This result is expected as ENSO is the dominant driver of tropical interannual variability, and the influence of the AMM-VWS relationship is less dominant at high-frequency timescales, as shown in Chelliah and Bell (2004) and Vimont and Kossin (2007).

Figure 2.6b displays the second leading mode (EOF2) that accounts for 23% of the structured variance. The EOF2 pattern shows a locally confined lobe of westerly shear (positive zonal anomalies) sandwiched between regions of easterly shear (negative zonal anomalies) stretching across the North Atlantic region. EOF2 exhibits features associated with active subtropical wave breaking that have been identified in zonal anomalies by Homeyer and Bowman (2013) and Zhang et al. (2016). In contrast to PC1, correlations with the tropical indices outlined in Table 2.2 are substantially reduced for PC2, further suggesting that the driver of the second mode of variability is subtropical in nature. AWB activity spurs anomalous easterly shear over the northernmost section of the tropical Atlantic with westerly VWS in the southernmost section of the Atlantic MDR as shown in Figure 2.3b. Therefore, AWB(+) years are indicated by strong positive anomalies within the PC2 time series. It is also notable that AWB-associated shear shows a correlation of r = 0.43 with PC1. We expect that PC1 will capture much of the variability in tropical VWS including impacts from AWB activity. ENSO and the AMM may also be indirect drivers of AWB activity by modulating large-scale temperature gradients and driving large-scale features such as the Walker

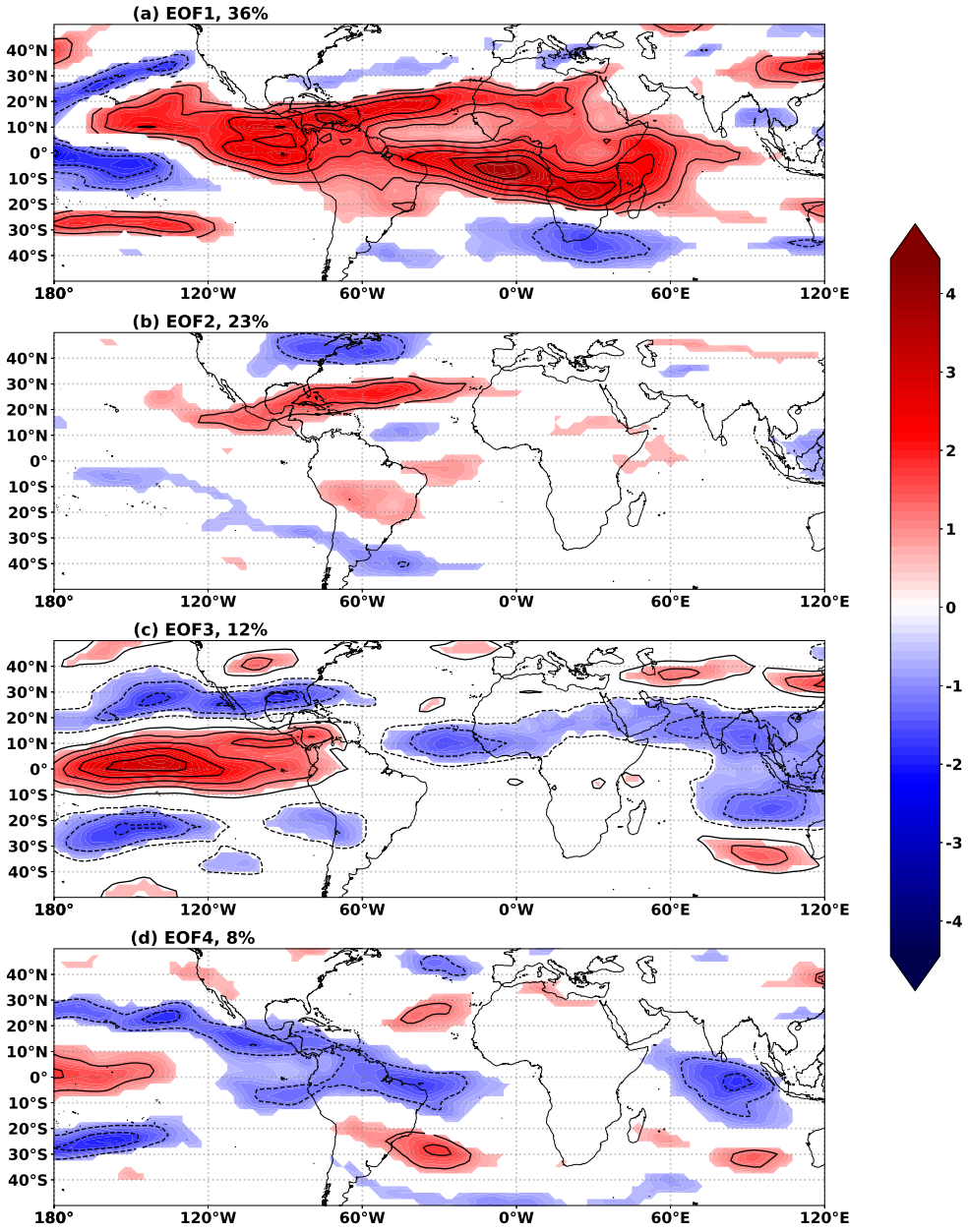

Figure 2.6: Regression of the first four principal components onto global zonal VWS anomalies (in m s^{-1}). Shaded regions and black contours at 0.5 m s^{-1} intervals indicate standard deviations of $\geq \pm 1$ for westerly (solid) shear anomalies and easterly (dashed) shear anomalies.

and Hadley Circulations and thereby triggering AWB events (Matthews and Kiladis 1999; Papin et al. 2020; Zavadoff and Kirtman 2019; Zhang and Wang 2019).

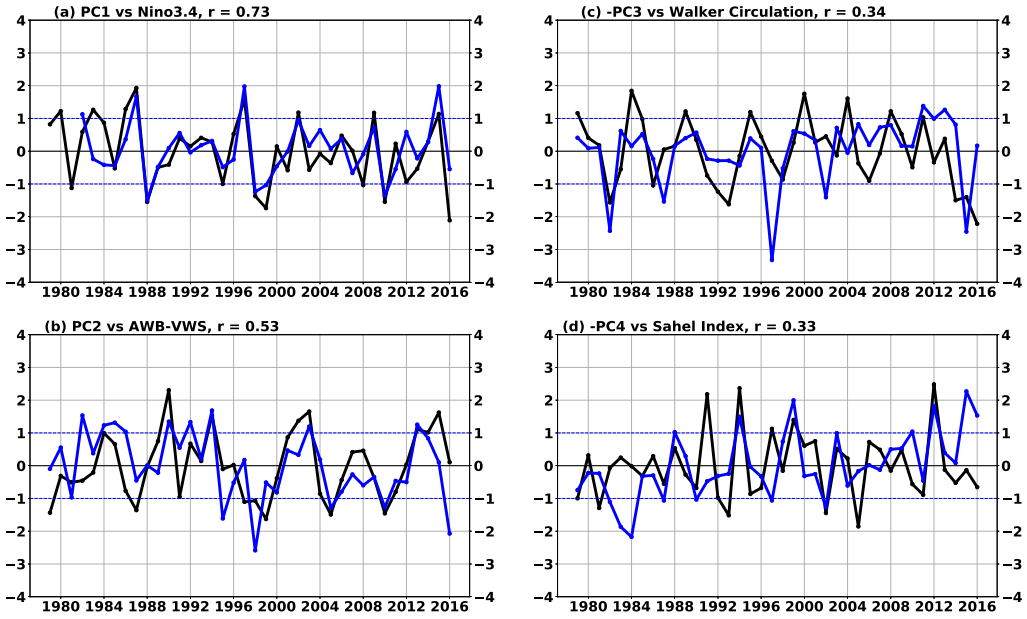

Figure 2.7: The first four principal components (PC) of July-September tropical North Atlantic zonal VWS anomalies. The PCs are expressed as a unit variance from the zero-mean. Each PC (in black) is plotted along with the July-September climate index (in blue) showing the largest correlation with the PC. PCs 3 and 4 are multiplied by a factor of -1 to better highlight the correlation between the corresponding climate index. The Walker circulation and Sahel rainfall indices are standardized to be comparable to PCs 3 and 4. The blue dashed lines indicate ± 1 standard deviation.

EOF3 in Figure 2.6c shows a region with strong westerly VWS anomalies, flanked to the north and south by anomalous easterly shear in the equatorial eastern Pacific region, indicative of an anticyclonic circulation. This strong westerly shear anomaly extends into the western North Atlantic region, while the eastern North Atlantic region is affected by anomalous easterly shear. We hypothesize that the EOF3 pattern is related to the tropical North Atlantic VWS's response to variations in the Walker Circulation. The third principal component (PC3) has a correlation of -0.34 with the Walker Circulation index (see Table 2.2). Also, Arkin (1982) found that the anticyclonic pattern shown in EOF3 was generally associated with a warm ENSO phase and a weak

Table 2.2: Pearson correlation between the four leading principal component (PC) time series of tropical North Atlantic VWS with ENSO, PVSI, Sahel, and AMM indices. Correlations statistically significant (based on the two-tailed p-value) are highlighted in italics. The strongest correlation with each PC is highlighted in bold.

Index	VWS	PC1	PC2	PC3	PC4
Niño-1+2	*0.46*	*0.54*	-0.13	***0.42***	-0.11
Niño-3	*0.65*	*0.69*	-0.02	*0.37*	-0.09
Niño-3.4	*0.73*	***0.73***	0.10	0.29	-0.09
Niño-4	*0.73*	*0.63*	0.27	*0.35*	-0.09
Walker Index	*-0.38*	*-0.48*	0.07	*-0.34*	0.04
Sahel	*-0.41*	*-0.56*	0.07	0.28	***-0.33***
AMM	*-0.49*	*-0.53*	-0.20	-0.12	0.17
AWB-VWS	*0.57*	*0.43*	***0.53***	-0.01	-0.21

phase of the Walker Circulation. PC3 also shows a moderate relationship with North Atlantic SSTs (Figure 2.8c), which is not surprising given its relationship to anomalous variations in the Walker Circulation (Figure 2.7c). We further point out that for PC3, the North Atlantic drives the pressure gradient shown in Figure 2.9c and may indicate the possible role of the state of the equatorial Pacific relative to the tropical North Atlantic in modulating North Atlantic VWS variability.

The fourth leading mode (EOF4) shown in Figure 2.6d features a tongue of anomalous zonal shear extending from the African Sahel into the tropical North Atlantic MDR. Figure 2.6d shows easterly shear with a wetter-than-normal Sahel, consistent with the studies of Karnauskas and Li (2016) and Dunion (2011) that highlighted the role of Sahel dynamics in influencing the tropical North Atlantic environment. EOF4 explains 8% of the variability in zonal shear in the North Atlantic region. African Sahel rainfall may likely contribute more to variations in meridional shear as rainfall over Africa is often modulated by a north-south shift of the Intertropical Convergence Zone (ITCZ). A wetter-than-normal Sahel induces anomalously easterly 200-hPa winds (resulting in anomalous easterly shear) while drought-like conditions over the Sahel favor westerly 200-hPa zonal wind and shear anomalies (Zhang and Delworth 2006). Therefore, tropical VWS has an

inverse relationship with Sahel rainfall (r = -0.41, as shown in Table 2.2). This is mirrored in correlations between PC4 and Sahel rainfall (r = -0.33).

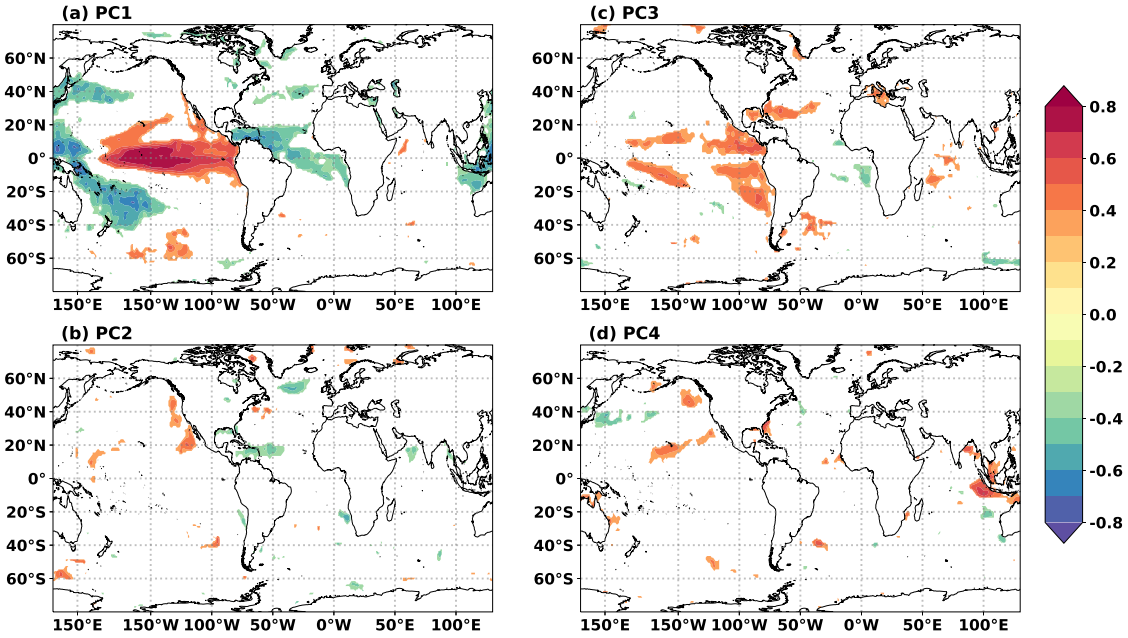

Figure 2.8: Spatial Pearson correlations of the first four principal components (PC1, PC2, PC3 and PC4) of tropical North Atlantic VWS with global mean sea surface temperatures. Colored shading indicates correlations statistically significant at the 95% level.

We note here that the AWB signal featured in EOF2 does not appear in EOF analyses of VWS averaged over the Atlantic MDR generally defined by the area 10^{o}N-20^{o}N and 80^{o}W-20^{o}W. In the EOFs formed from MDR VWS, more than 50% of the explained variance is accounted for by the leading mode of variability that is closely related to ENSO. African Sahel rainfall is also identified as a major driver, consistent with Goldenberg and Shapiro (1996) and Aiyyer and Thorncroft (2006). Our results suggest that variability between 20^{o}N-30^{o}N is necessary to fully capture the impacts of AWB on VWS.

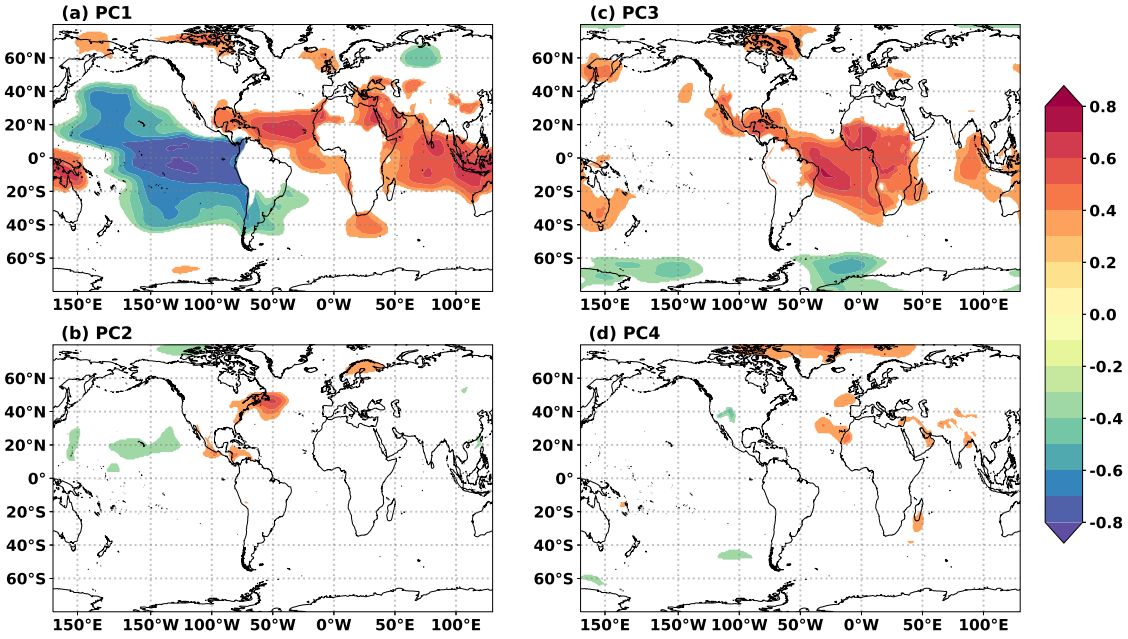

Figure 2.9: As in Figure 2.8, but for global mean sea level pressure. Colored shading indicates correlations statistically significant at the 95% level.

2.5 AWB-associated VWS anomaly (AWB-VWS) as a predictor of summertime shear

Various studies have shown that the environmental impact of AWB events can be observed in the modulation of deep-layer VWS (Zhang et al. 2016; Papin et al. 2020; Li et al. 2018). I next create an index of the sum of the shear anomalies collected along the downstream edge of potential vorticity streamers, which is the edge most associated with an increase in westerly shear in the North Atlantic MDR (Papin et al. 2020; Zhang et al. 2017). The index, referred to as AWB-VWS, shows AWB(+) years to have positive (westerly) anomalies within the North Atlantic, while AWB(-) years have negative (easterly) anomalies indicating a weak downstream anticyclonic circulation. The AWB-VWS index shows a strong positive correlation with tropical VWS and its first and second modes of variability, consistent with the dynamical explanations of EOF1 and EOF2. As shown in Table 2.2, AWB-VWS has a 0.57 correlation with tropical North Atlantic VWS anomalies and a 0.53 correlation with PC2. Therefore, EOF2 is strongly influenced by the

large easterly shear anomalies lining the northern edge of the tropical North Atlantic region (see Figure 2.6b).

Table 2.3: Correlations of the four principal components (PC1, PC2, PC3, PC4) and the AWB-VWS index with seasonal tropical North Atlantic VWS and North Atlantic ACE south of 35^{o}N. Correlations statistically significant at the 95% level are highlighted in bold.

	$PC1$	$PC2$	$PC3$	$PC4$	AWB-VWS
JJA VWS	**0.82**	**0.35**	-0.13	-0.08	**0.48**
JAS VWS	**0.86**	**0.40**	-0.14	-0.16	**0.57**
ASO VWS	**0.72**	**0.35**	-0.31	-0.08	**0.53**
SON VWS	**0.45**	0.09	**-0.40**	-0.23	0.18
JJA ACE	-0.30	-0.29	-0.23	0.26	**-0.49**
JAS ACE	**-0.46**	-0.32	**-0.42**	0.17	**-0.50**
ASO ACE	**-0.56**	-0.26	-0.32	0.16	**-0.58**
SON ACE	**-0.65**	-0.21	**-0.32**	0.11	**-0.53**

Table 2.3 outlines the correlations of the time series of PCs1-4 and the AWB-VWS index with seasonal tropical North Atlantic shear and ACE south of 35^{o}N. As expected, PC1 shows the strongest correlations with JAS VWS, but also shows strong correlations with shear prior to and after the shear's peak in the JAS season. Correlations with PC2 are weak prior to JAS and show little correlation with tropical VWS in SON. This is also reflected in correlations with the AWB-VWS index and suggests that AWB activity has the greatest impact on contemporaneous seasonal shear anomalies. This relationship was also observed for subseasonal modulations of shear by AWB activity (Li et al. 2018). Compared to PC2, the AWB-VWS index shows a stronger correlation with shear outside of the contemporaneous shear season. Correlations with PC3 and PC4 are weaker than the PC1, PC2 and AWB-VWS indices. PC3 has stronger correlations with shear in the ASO and SON seasons, while PC4 has weak seasonal correlations.

While the second leading mode of variability only accounts for 23% of the explained variance, previous studies (Papin et al. 2020; Zhang et al. 2016, 2017) have already indicated the likely influence of AWB-associated VWS on seasonal TC activity. We expect that a better understanding

Table 2.4: The average number of named storms, hurricanes, major hurricanes and ACE in the five years with the highest (lowest) standardized values for PC1 and PC2.

	PC1-top five	PC1-bottom five	PC2-top five	PC2-bottom five
Named storms	9	14	13	12
Hurricanes	3	8	5	6
Major hurricanes	2	4	1	3
ACE	44.3	142.5	72.4	80.0

of the contribution of each driver to summertime VWS variability will ultimately improve our understanding of the drivers of seasonal TC activity in the North Atlantic. Tropical zonal VWS has a correlation of -0.43 with July-September ACE (see Table 2.3). We further examine the ability of the AWB-VWS index as a predictor of TC seasonal variability in Tables 2.4 and 2.5. Table 2.4 shows the average number of various metrics of TC activity for years corresponding to the five highest and lowest values for PC1 and PC2. As expected, changes in PC1 show a stronger change in the TC metrics. The PC2-TC relationship is less consistent, with only modest changes in the TC metrics.

Table 2.5: Root mean squared error (RMSE), variance explained (r^2), and F-statistic associated with the stepwise regression of VWS, AWB-VWS and the four leading modes against the July-September ACE index.

Combination	RMSE	r^2	F
VWS only	14.30	0.17	8.61
AWB-VWS only	13.74	0.24	12.37
PC 1 only	14.35	0.17	8.33
PCs 1+2	13.36	0.27	8.09
PCs 1+2+3	11.75	0.44	10.70
PCs 1+2+3+4	11.88	0.43	7.91

We further quantify the contribution of PC2 and AWB-VWS to a statistical linear prediction model for ACE based on zonal VWS. The four leading modes are regressed against ACE using

stepwise regression, and the contribution of each mode to the regression strength is outlined in Table 2.5. A major contribution to the regression is indicated by a decrease in the root mean squared error (RMSE), an increase in the variance explained (r^2) and an increase in the significance of the variance or F-statistic of the linear combination. PC1 holds most of the regression strength and is capable of being a stand-alone predictor. The addition of PCs 2 and 3 further lowers the RMSE, and improves the variance explained, though changes to the F-statistic are modest. The F-statistic weakens with the addition of PC4. The AWB-VWS index shows similar skill at simulating ACE compared to the PC1-PC2 model combination. While the contribution may be modest, the inclusion of AWB impacts on shear into statistical schemes for operational seasonal prediction shows improvement in accounting for years driven predominantly by AWB. In the next chapter, we analyze the inclusion of an AWB-VWS index in Colorado State University's early April statistical TC forecast scheme.

Table 2.5 also shows that PC3 contributes a significant increase to the regression strength against the July-September ACE index, increasing the variance explained from 27% to 44%. Following a similar stepwise regression approach as described above, with PC3 as the only predictor, PC3 explains $\sim 15\%$ of the observed variance with a regression strength of 7.3. Based on these values, the Walker circulation-associated PC3 may not be the most suitable stand-alone predictor for ACE, but it does seem to explain an important portion of variance not already covered by PCs 1 and 2. In contrast to the other PCs, PC3 has a strong tropical eastern Atlantic signal (Fig. 2.6c), possibly due to SLP variations over the tropical South Atlantic (Fig. 2.9c). The regression statistics suggest that the PC-1+2+3 combination is a stronger representation of the overall impact of VWS on seasonal TC variability.

2.6 Discussion and Conclusions

In this study, both tropical and extratropical contributions to the variability of seasonal 200-850 hPa zonal vertical wind shear in the tropical North Atlantic region are identified using compositing and EOF analysis. Major findings of this analysis include:

1. The first leading mode of variability in tropical North Atlantic zonal VWS accounts for 36% of the structured variance and is driven by interannual variations in ENSO and the AMM, suggesting that tropical sources of shear are the dominant contributor to VWS.

2. Anti-cyclonic wave breaking (AWB) activity is shown to be associated with the second EOF mode and accounts for 23% of the structured variance. While not as strong as ENSO, this extratropical source of shear is a significant contributor to VWS variability and TC activity.

3. The third leading mode is associated with a pressure gradient that is likely modulated by the Walker Circulation, accounting for 12% of tropical VWS.

4. African Sahel rainfall is associated with the fourth mode of variability in high-frequency variations of tropical North Atlantic zonal VWS, accounting for 8% of the structured variance.

While the leading EOF modes are by design orthogonal, there remains some shared physical relationships between the drivers of each of the four leading modes. As observed in Section 2.3 above, the influence of AWB on VWS activity is difficult to characterize due to ENSO's strong influence on the tropical North Atlantic region (see Figs. 2.3 and 2.4). One limitation of the study was the inability to separately analyze the contributions of AWB to tropical VWS variability due to substantial overlap with strong ENSO events. Even if the threshold definitions of ENSO and AWB events are relaxed, there are still not enough samples of anomalous AWB years with neutral ENSO conditions or anomalous ENSO years with neutral AWB conditions to fully differentiate their impacts on the observed environment. The overlap raises a question about how much ENSO imprints on AWB variability and the subsequent relationship with seasonal TC activity. Therefore, a complete separation of the tropical and subtropical influences has not been achieved. The dominance of ENSO may be a key reason for the inability to observe significant impacts of AWB on seasonal TC activity during all years with anomalous AWB, as observed by Li et al. (2018).

The results presented in Section 2.4 suggest that the tropical sources of VWS from ENSO are indeed dominant, but that extratropical sources of VWS from AWB are an important contribution

to tropical and subtropical VWS variability and TC activity. The present analysis shows that the second mode of variability of tropical North Atlantic VWS may be attributed to subtropical AWB activity (Galarneau et al. 2015; Zhang et al. 2017). Our results are consistent with Zhang et al. (2016) and Zhang et al. (2017), who previously highlighted the dynamical role of AWB in driving seasonal TC variability through modulations of VWS. The current study adds to their findings by quantifying the AWB impact on the tropical North Atlantic VWS relative to ENSO's strong influence on the tropical North Atlantic summertime circulation.

Another key result is the overshadowing of an AWB signal in the leading modes of interannual variability when restricting analyses of unfiltered tropical North Atlantic VWS to only the MDR. The MDR does not fully encompass the spatiotemporal patterns driving VWS within the North Atlantic region, where TCs are prevalent. The MDR domain is large enough to incorporate the impacts of both ENSO and the African Sahel on VWS (Aiyyer and Thorncroft 2006), but not the impacts of AWB. Extending the domain to 30^{o}N better captures the full extent of the leading modes of VWS variability that impact TCs.

This study has focused on zonal VWS due to the fact that meridional VWS variability accounts for a smaller portion of the overall horizontal shear variability. There may be impacts from large-scale variations in the Atlantic Multidecadal Mode (Patricola et al. 2016) that modulate meridional variations in VWS over the wider North Atlantic (Vimont and Kossin 2007). Further analysis of meridional shear variability is recommended for future work.

While recent studies have improved our understanding of the variability of both deep-layer shear and AWB activity, their impacts on TC activity are not well-documented and warrant further research. By examining the deep-layer shear directly, we take the first step to assessing the predictability of VWS and quantifying the response of the environment, and consequently TC activity, with respect to each large-scale driver. VWS anomalies induced by AWB activity (AWB-VWS) may be a better indicator of AWB's impacts on VWS compared to directly using the second leading EOF mode as an index. The AWB-VWS index calculated has a significant correlation with both tropical North Atlantic VWS (r = 0.57) and seasonal ACE (r = -0.50), suggesting its possible

use as a predictor in seasonal TC forecasting. The results of this study highlight the importance of AWB on seasonal North Atlantic TC activity in the summertime, in addition to the impacts of ENSO, the Walker circulation, and Sahel rainfall. In the next chapter, I investigate the inclusion of boreal winter AWB into an early April operational Atlantic seasonal hurricane prediction scheme.

Chapter 3

Wintertime Rossby Wave Breaking Persistence in Extended-range Seasonal Forecasts of Atlantic Tropical Cyclone activity[2]

3.1 Introduction

Atlantic seasonal TC prediction is complex due to the overlapping driving forces of several large-scale climate phenomena. The main large-scale drivers of the Atlantic atmospheric circulation include the Atlantic Meridional Mode (AMM; Kossin and Vimont 2007; Patricola et al. 2014) and El Niño-Southern Oscillation (ENSO; Gray 1984; Camargo et al. 2007) on interannual timescales and the Atlantic Multidecadal Oscillation (AMO; Goldenberg et al. 2001; Klotzbach and Gray 2008) on multidecadal timescales. Through their influence on the large-scale atmospheric circulation, these oscillations provide substantial predictability of the tropical environment, accounting for more than 30% of the explained variance (Chelliah and Bell 2004; Aiyyer and Thorncroft 2006; Jones et al. 2020). Consequently, environmental metrics closely related to ENSO and the AMM are frequently used as predictors for seasonal TC activity (Klotzbach and Gray 2008; Klotzbach et al. 2017). However, these drivers are at times insufficient to account for certain changes that occur from month-to-month that may be attributed to intraseasonal variability.

Recently, several studies have identified a strong relationship between seasonal TC activity and boreal summer (hereafter summertime) subtropical anticyclonic Rossby wave breaking (Zhang et al. 2016, 2017; Jones et al. 2020; Papin et al. 2020). AWB is the irreversible overturning of potential vorticity (PV) contours against a strong PV gradient that results in the mixing of dry

[2]The analysis and results presented in this chapter are currently under review for the *Journal of Climate*: Jones, J.J. M.M. Bell, P.J. Klotzbach, E.A. Barnes, 2021: Wintertime Rossby wave breaking persistence in extended-range seasonal forecasts of Atlantic tropical cyclone activity, *Journal of Climate (In Review)*.

midlatitude high-PV air into lower latitudes (McIntyre and Palmer 1983). The reverse dynamical effect can be observed with cyclonic wave breaking where moister low-PV air is mixed into the midlatitude atmosphere. Synoptic-scale AWB episodes on the 350-K isentropic surface occur frequently over the subtropical Atlantic (Zhang et al. 2017; Papin et al. 2020), peaking between July-September (Fig. 3.1). Further description of how AWB is detected and quantified is given in section 3.2. Anomalously intense AWB is associated with increased vertical wind shear (known hereafter as VWS) and decreased moisture content over the tropical Atlantic, conditions that typically suppress the development of TCs (Jones et al. 2020). Anomalous westerly VWS is generally introduced to the tropical environment via the downstream edge of equatorward PV streamers.

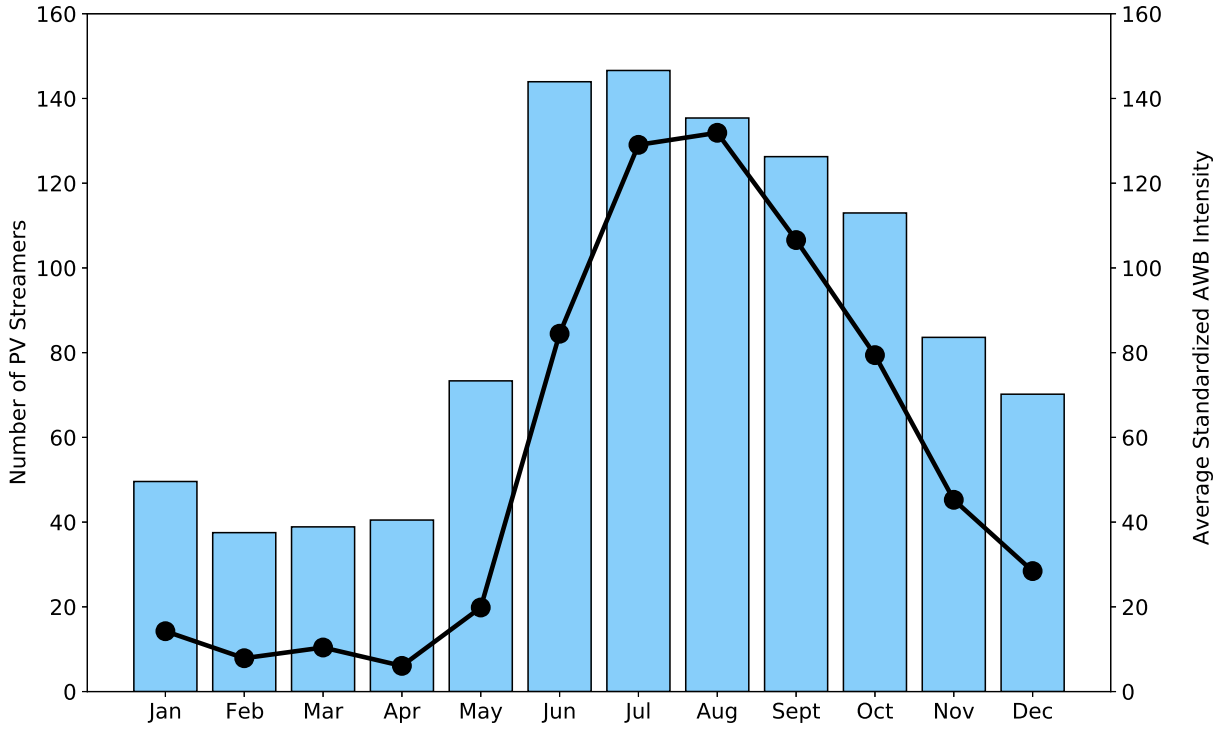

Figure 3.1: Average monthly anticyclonic wave breaking intensity (black solid line) and number of equatorward potential vorticity (PV) streamers (blue bars) over the North Atlantic from 1979-2019.

The 2013 Atlantic hurricane season was characterized by warm tropical Atlantic SSTs, sustained cool neutral ENSO conditions, and anomalously low sea level pressure over the Caribbean basin (Klotzbach and Gray 2013; Saunders et al. 2020), conditions that suggested a favorable en-

vironment for enhanced TC activity. However, Klotzbach and Gray (2013) also observed that the 2013 August-October environment was characterized by strong upper-level convergence indicating subsidence and reduced rainfall over the Atlantic. Zhang et al. (2016) later showed that the 2013 season was suppressed through anomalously frequent subtropical AWB in August due to a stronger and more eastward-shifted Atlantic midlatitude jet. Anomalous AWB continued into September, consequently reducing moisture and relative humidity over the Atlantic Main Development Region (MDR). These observations suggest that metrics of subseasonal AWB impacts can be useful in current prediction schemes to account for years in which subtropical Atlantic dynamics drive the tropical environment.

The intrinsic predictability of weather states and extremes based on certain large-scale atmospheric phenomena are oftentimes intermittent and inconsistent over time (Mariotti et al. 2020), depending on the forecast window. Klotzbach and Gray (2004) observed a degradation in the African rainfall relationship with Atlantic TCs, while Camargo and Sobel (2010) noted that the Quasi-Biennial Oscillation (QBO)-Atlantic TC relationship was no longer significant. Both predictors had a strong relationship with seasonal TC activity in the Atlantic from the 1950s to the mid-1990s but have shown little skill in recent years. A similar situation exists with AWB variability. Subtropical Atlantic AWB dynamics are synoptic and nonlinear in nature (Abatzoglou and Magnusdottir 2006b; Bach et al. 2019), and their predictability depends in large part on the background state, the dominant subseasonal or seasonal atmospheric influence – for example subseasonal influences of the Madden-Julian Oscillation (MJO; Madden and Julian 1972) – and consequent evolution of the environment via eddy fluxes. AWB activity shows significant negative correlations with TC activity on both subseasonal and seasonal timescales, but the strength of the AWB-TC relationship may vary from year to year (Li et al. 2018; Zhang and Wang 2019).

The scientific literature currently provides little guidance for predicting the impacts of AWB on TC activity. Zhang and Wang (2019) have suggested that AWB over the western Atlantic has a stronger influence on TC activity than AWB farther east. Western Atlantic AWB activity has a negative correlation with the AMM (Zhang and Wang 2019) and the AMM's modulation

of Caribbean precipitation anomalies. A positive phase of the AMM and increased precipitation over the Caribbean is typically associated with less frequent AWB. Drouard et al. (2013) and Zavadoff and Kirtman (2019) indicated that subtropical Pacific dynamics may influence Atlantic wave breaking via modulation of the Rossby wave train that propagates synoptic waves farther downstream. The results of these studies further suggest that dynamical oscillations such as the Pacific Decadal Oscillation (PDO) or the Pacific-North American Oscillation (PNA) can be used to assess wave breaking impacts on Atlantic convective events (Drouard et al. 2015; Zavadoff and Kirtman 2019).

Several studies have examined AWB's association with large-scale oscillations over the Atlantic region. Of note is the relationship between wave breaking and the North Atlantic Oscillation (NAO) in the boreal winter (hereafter winter). Benedict et al. (2004) indicated that sustained wave breaking in the winter could determine the phase of synoptic NAO variations. Intense AWB on the equatorward side of the subtropical jet stream displaces the jet northward and forces a positive phase of the NAO over the Atlantic, while cyclonic wave breaking along the poleward side of the jet forces an equatorward displacement of the jet stream and a negative phase of the NAO (Abatzoglou and Magnusdottir 2006a,b; Franzke et al. 2004).

Scaife et al. (2014) observed that the NAO, driven largely by internal atmospheric variability, has an intrinsic limit of predictability of around 3 weeks. However, there is also evidence of persistence beyond this limit through quasistationary regimes associated with the variability of the Azores High and Aleutian Low (Czaja et al. 2003) or through persistent SST anomalies (Ogi et al. 2003). Persistence is defined here as the degree of dependence among successive values in time of a given phenomenon, and is often a measure of the time interval between independent events (Wilks 2011). Given AWB's association with NAO variability, we hypothesize that there is a significant relationship between winter and summer wave breaking and investigate this hypothesis in this chapter.

The purpose of our study is to assess winter-summer AWB variability and mechanisms by which we can infer possible AWB impacts on seasonal TC activity. Unlike previous studies, we

show that AWB not only has a subseasonal relationship with the NAO, but also a statistically significant seasonal relationship that has persistence on seasonal timescales. We also show that this seasonal AWB-NAO relationship has a strong association with TC activity. Including AWB impacts in seasonal Atlantic TC prediction accounts for anomalously suppressed seasons such as 2013 (Saunders et al. 2020) and for strong subtropical Atlantic forcing of the Atlantic environment. Depending on the intensity of wave breaking, AWB impacts may enhance or sustain current tropical environmental conditions. Alternatively, AWB may dominate tropical variability and TC activity when other large-scale drivers are relatively weak.

Jones et al. (2020) showed that subtropical AWB is associated with the second leading mode of tropical vertical wind shear anomalies averaged over the Atlantic Main Development Region (MDR). Generally defined as 10^{o}N-20^{o}N, 85^{o}W-20^{o}W, Jones et al. (2020) extended the MDR to include the subtropics between 20^{o}N-30^{o}N. The subsequent AWB-shear (AWB-S) index correlated at -0.58 with August-October accumulated cyclone energy (ACE; Bell et al. 2000), statistically significant at the 95% level. As a single predictor regressed against July-September ACE values from 1979-2016, the AWB-S index exhibited a higher correlation compared with vertical wind shear anomalies averaged for the Atlantic MDR. The correlation between July-September ACE and the AWB-S index was $r = -0.57$, while the correlation between July-September ACE and VWS anomalies averaged over the Atlantic MDR was $r = -0.50$ (Jones et al. 2020). Additionally, the second principal component associated with AWB improved the variance explained in ACE when combined with the leading principal component (associated mainly with ENSO) from $R^2 = 0.17$ to $R^2 = 0.27$.

In the sections that follow, we explore the relationship between winter and summer wave breaking episodes, how it manifests within the environment, and its consequent impact on seasonal TC predictability. The paper is organized as follows: Section 3.2 outlines the data and methods used to further analyze the persistence of AWB impacts on the tropical environment. Section 3.3 describes the winter environmental precursors associated with summer AWB, while Section 3.4 examines the

use of a winter AWB-associated index as a predictor in an extended-range forecast model. Section 3.5 provides some concluding remarks.

3.2 Data and Methods

3.2.1 Data

The TC analysis that follows uses ACE as the metric to classify overall seasonal activity levels. ACE is defined as the sum of the squares of the six-hourly maximum wind speeds for each tropical and subtropical cyclone with one-minute maximum sustained winds of at least 34 knots (Bell et al. 2000). The index is calculated using the National Hurricane Center's best track database (HURDAT2; Landsea and Franklin 2013).

Environmental fields on both six-hourly (0Z, 6Z, 12Z, 18Z) and monthly timescales were obtained from the ECMWF's fifth generation reanalysis dataset (ERA5) of the global climate (Hersbach et al. 2020). Reanalysis data are currently available from 1 January 1979 to the present. The gridded ERA5 reanalysis has a horizontal resolution of 0.25^o x 0.25^o for the atmosphere and 0.5^o x 0.5^o for ocean waves. Six-hourly potential vorticity and zonal wind anomaly fields used in the AWB detection algorithm were obtained with a resolution of 2.5^o x 2.5^o to remove small-scale disturbances (Postel and Hitchman 1999). We obtained the 2.5^o x 2.5^o fields directly from the ECMWF's Climate Data Store (CDS) online platform (https://cds.climate.copernicus.eu/). Monthly sea surface temperature anomalies were obtained from the National Oceanic and Atmospheric Administration's (NOAA) Optimum Interpolation Sea Surface Temperature version 2 (NOISSTv2) dataset from 1982-2019 (Reynolds et al. 2002). Anomalies for all fields are calculated relative to the 1981-2010 base period except for SST which is calculated from a 1982-2010 base period.

Monthly indices were obtained for the NAO, ENSO and AMM. The NOAA Climate Prediction Center (CPC)'s monthly NAO index is calculated from daily indices. The daily NAO index is defined by the leading rotated principal component of Atlantic 500-hPa height anomalies between 20^oN-90^oN (Barnston and Livezey 1987). Daily height anomalies are standardized by the monthly mean and standard deviations from the principal component analysis. Variations in ENSO are

assessed using the Niño 3.4 index (5^oS-5^oN, 170^o-120^oW) from 1982-2019 and are calculated from the NOISSTv2 dataset (Trenberth 2020). The AMM is defined as the principal leading mode of a maximum covariate analysis applied to Atlantic SSTs and 10-m surface wind speeds over the region 21^oS-32^oN and 74^oW-15^oE (Chiang and Vimont 2004; Kossin and Vimont 2007).

3.2.2 Methods

Following Jones et al. (2020), tropical zonal Atlantic VWS is defined as the difference between the 200-hPa and 850-hPa zonal wind fields and averaged over the region 10^oN-30^oN and 85^oW-20^oW. We note that, while the zonal component of shear captures much of the structured variability in the total shear vector, this does not mean the meridional component does not contribute. Anomalies were calculated relative to the 1981-2010 to remove both the seasonal cycle and the climatological mean. The 1981-2010 period is the 30-year climatological normal used in this study to assess anomalies within the seasonal environment (WMO 2017). An empirical orthogonal function (EOF) analysis was applied to July-September VWS fields from 1979 to 2019 and the second leading mode (PC2) previously associated with AWB activity was extracted, extending the time series of the second leading mode from the 1979-2016 period used in Jones et al. (2020).

We generated spatial correlations between the July-September PC2 index and seasonal sea level pressure (SLP), sea surface temperature (SST), and 850-hPa (U850) and 200-hPa (U200) zonal wind anomaly fields for the seasons January-March (JFM), April-June (AMJ), July-September (JAS), and October-December (OND). The JAS season is considered to be at zero-lag (hereafter referred to as T), while the JFM, AMJ, and OND seasons are considered lags at T-2, T-1, and T+1 seasons, respectively.

Statistical significance within the study is assessed in two ways. The significance of correlations are measured at the 95% confidence level corresponding to a p-value <0.05 based on a two-sided Student's t-test. The statistical significance of the differences between high and low composites are measured using the non-parametric Wilcoxon signed rank test. The Wilcoxon signed rank test categorizes the signed ranked differences into positive (W+) and negative (W-) groups, and calculates the sum of each category. If the difference between W+ and W- metrics are

larger than the threshold of 14 for $\alpha = 0.05$ and a sample size of 12, the null hypothesis that the differences are similar can be rejected (Wilks 2011).

For the present study, to assess the persistence of AWB's impact on the seasonal Atlantic environment, we projected an index of 200-hPa zonal wind anomalies onto the characteristic split-jet signal of AWB in the upper-level zonal wind field. The wave breaking or split-jet signal consists of a meridional tripole of zonal winds. This method of pattern projection, outlined in detail by Baldwin et al. (2009), was calculated using Equation (3.1) below:

$$\mathbf{U200_{proj}} = \frac{\mathbf{Xe}}{\mathbf{e^T e}} \tag{3.1}$$

where $U200_{proj}$ is the index obtained from projecting the 200-hPa wind field $\mathbf{X}$ onto the flattened correlation pattern between the AWB-S index (or the second loading pattern in summertime VWS anomalies) and the wintertime upper-level zonal wind anomalies. The correlation pattern is denoted by $\mathbf{e}$. The $U200_{proj}$ index is then a pattern vector, much like the principal components from an EOF analysis, and indicates in standard deviations how similar the observed wintertime zonal upper-level wind field is to the correlation pattern. Alternatively, U200proj is a measure of the presence of the summer AWB-S precursor signal within winter upper-level zonal winds. The index is used to further explore AWB's association with variations in 200-hPa zonal wind anomalies over the Atlantic region. Both the JFM and JAS AWB-S indices and the projected index are standardized over the 1981-2010 period. A more detailed description of the variability associated with the projected index is given in Section 3.3.

A cross-spectrum analysis was applied with a Hanning window to examine shared frequencies (Storch 1999) of variability in the monthly 1979-2019 $U200_{proj}$, NAO and Niño 3.4 indices. Shared frequencies refer to periods of variability in which two variables are related within the spectral domain. To calculate the power spectrum of each index, the indices were separated into 6 chunks of 76 months with an overlap of 50% to avoid loss of information. The means of each chunk were removed to eliminate the zero-frequency signals. A chunk length of 76 months is chosen to maximize the number of chunks and degrees of freedom for the cross-spectrum analysis,

while maintaining many samples in each chunk. A shared frequency was considered statistically significant at the 95% level if the coherence squared (Coh^2) was above 0.45.

Lastly, we compare the skill of Colorado State University (CSU)'s 2019 and 2020 early April statistical schemes at extended range predictions of seasonal ACE. Unlike the 2019 early April scheme, the most recent 2020 scheme comprises an AWB-S associated predictor (Klotzbach et al. 2019, 2020a). The predictors are ranked based on the strength of their regression against ACE (via the *F*-value) and the statistical significance of the regression strength (via the *p*-value). The *F*-value is the ratio of the mean sum of squares to the mean squared error (Wilks 2011) and measures whether an unrestricted model (e.g., a combination of predictors thought to be most appropriate for the data) performs better than a restricted model with the slope equal to zero. If the unrestricted model performs better than the restricted model, *F* is larger. The *p*-value assesses how significant the *F*-value is. The threshold for a statistically significant *F*-value (F_{critical}) is 2.01 for a sample size $n = 41$ and is associated with a 90% significance level (p=0.1).

A revised statistical model is created by selecting the top four predictors with the largest F-value. The performance of the revised model is measured using the mean absolute error (MAE) and the explained variance (R^2) scores and is compared to the performance of the original early April statistical scheme.

3.2.3 Detecting AWB and AWB-associated VWS (AWB-S)

Wave breaking indices in this study were generated using an algorithm based on the techniques of Papin et al. (2020) and detailed in Jones et al. (2020). The algorithm calculates the potential vorticity streamer intensity (PVSI) from each PV anomaly detected. PVS intensity is defined as the standardized PV anomaly relative to a six-hourly climatological mean and is integrated over the areal extent of the PV streamer detected along the 2-PVU (1 PVU $\equiv 10^{-6}$ K m^2 s^{-1} kg^{-1}) contour on the 350-K isentropic surface. The algorithm detects more than two consecutive points along the 2-PVU contour with an eastward (west to east) PV gradient $\left(\frac{\partial PV}{\partial x} > 0\right)$ and a reversal in the poleward meridional PV gradient $\left(\frac{\partial PV}{\partial y} < 0\right)$ for the upstream edge of the PV tongue. The opposite criteria is applied for detection of the downstream edge $\left(\frac{\partial PV}{\partial x} < 0\,,\ \frac{\partial PV}{\partial y} > 0\right)$ (Abatzoglou

and Magnusdottir 2006b; Papin et al. 2020). As done in Jones et al. (2020) and Papin et al. (2020), once the points outlining the PV tongue are identified, a line connects the two end points to capture the PVS polygon and as much of the PVS area as possible.

In addition to the count and intensity, the same detection algorithm collects the vertical wind shear anomalies from the zonal shear field at consecutive points along the downstream edge of each detected PV streamer (Jones et al. 2020). We note that the shear patterns associated with AWB can extend well into the tropics producing large VWS anomalies along both the upstream and downstream edges. Correlations of the sum of the downstream and upstream AWB-S anomalies with VWS averaged over the MDR (not shown) are very similar to correlations for the downstream AWB-S only. Therefore, we opt to use the downstream AWB-S in calculating the AWB-S indices. The VWS anomaly is then summed to obtain an index of AWB-associated VWS (AWB-S). The AWB-S index can be used to examine the level of sustained impact to the tropical environment by intense wave breaking.

3.3 Evidence for a strong winter-summer AWB connection

3.3.1 PC2 correlations with the seasonal environment

Figure 3.2 shows correlations, significant at the 95% confidence level based on the two-sided Student's t-test, between the 1979-2019 JAS second leading mode of tropical Atlantic VWS (PC2) and seasonal SLP, SST, U850 and U200 anomaly fields. The JFM, AMJ, JAS and OND seasons represent lags of T-2, T-1, T-0 and T+1 seasons, respectively. AWB – identified by upper-level anticyclonically sheared wind anomalies that are hereafter referred to as the wave breaking signal – is associated with higher SLP anomalies (Figs. 3.2a-d) and lower SST anomalies (Figs. 3.2e-h) across the tropical and subtropical Atlantic region. These associations are evident in the concurrent environmental fields (Figs. 3.2c,g,k,o). We further observe that summer AWB impacts, quantified using the PC2 index, have strong associations with the seasonal environments preceding and following JAS. Of note, several JFM environmental fields correlate strongly with JAS AWB. Of particular note are the winter U850 and U200 patterns (see Figs.3.2i,m) that suggest a physical link between winter and summer AWB.

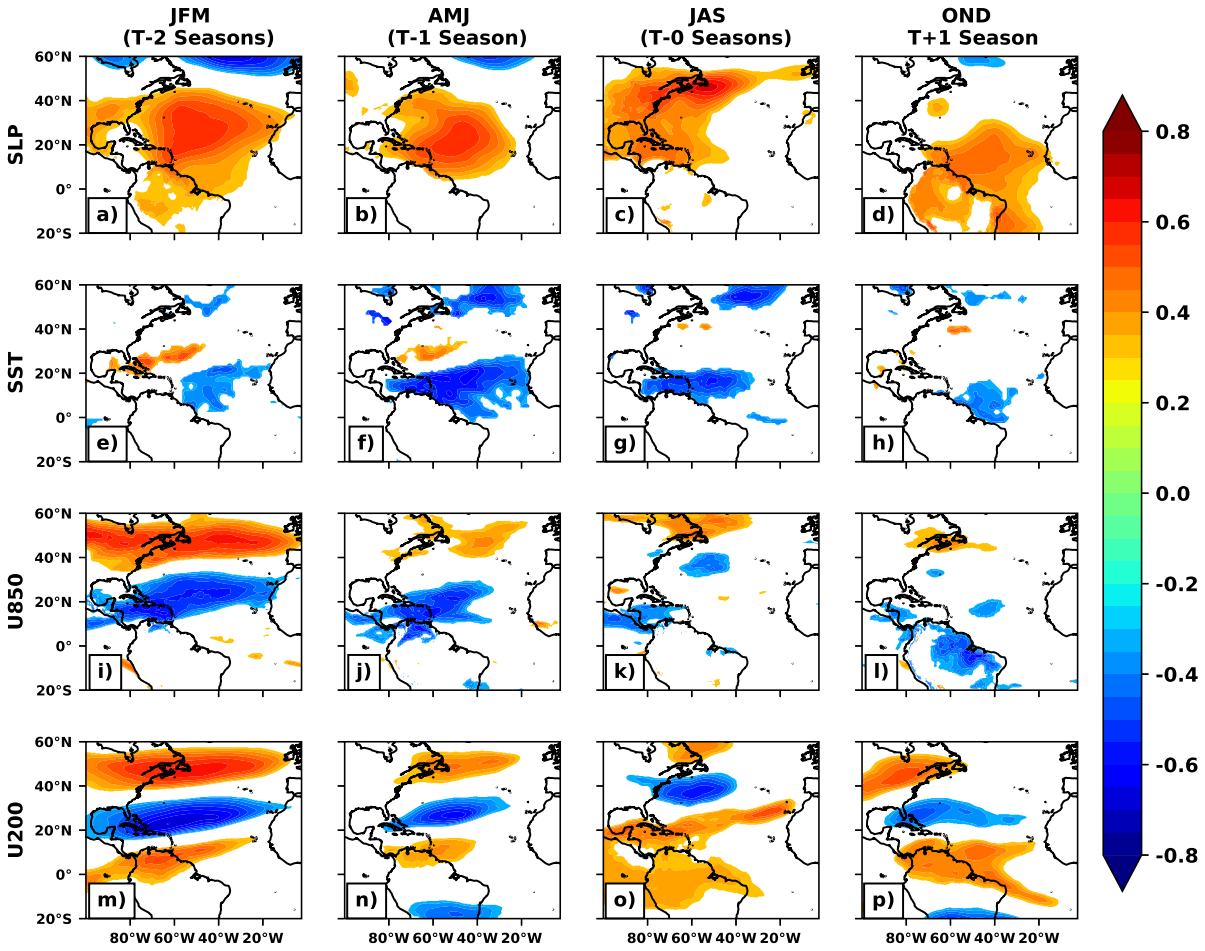

Figure 3.2: Spatial correlations between the second leading mode (PC2) of 1979-2019 July-September (zero-lag, T-0 seasons) North Atlantic vertical wind shear (10-30^{o}N, 85-20^{o}W) and seasonal anomalies in SST, SLP, 200-hPa and 850-hPa winds for January-March (T-2 seasons), April-June (T-1 season), and October-December (T+1 season). Only correlations statistically significant at the 95% confidence level are shaded. Green contours highlight correlations $\geq \pm 0.4$ or greater with intervals of 0.2.

n Figures 3.2a-d, summertime AWB activity shows strong positive correlations with Atlantic SLP anomalies, meaning SLP anomalies increase over the central Atlantic with more intense wave breaking. The correlation pattern is consistently strong across the tropical and subtropical Atlantic region from JFM through OND. This result is consistent with previous studies of winter AWB activity. Abatzoglou and Magnusdottir (2006b) and Bowley et al. (2019) found correlations >0.5 between winter AWB and the NAO. There is a noticeable shift in the position of the SLP correlation maximum from the eastern Atlantic during the boreal winter and spring to the western Atlantic during JAS. Increased SLP anomalies over the Caribbean and northeastern US coast indicate strong AWB activity. In OND, the signal weakens over the western Atlantic and migrates back towards the eastern Atlantic. The eastern position of the SLP signal generally indicates weaker AWB (**?**Papin et al. 2020). The seasonal AWB-SLP correlations show that there are robust precursor signals that may be used to predict summer AWB-associated shear impacts. These strong signals within SLP may also suggest that summer AWB activity is in some way connected to the state of the NAO in preceding seasons via its modulation of large-scale SLP anomalies.

Figures 3.2e-h show that the JAS PC2 index is anti-correlated with tropical Atlantic SSTs. Above-normal AWB activity is associated with negative SST anomalies along the downstream edge of a PV streamer and positive SST anomalies along the upstream edge (Zhang et al. 2017; Papin et al. 2020). Zhang and Wang (2019) show that these negative SST anomalies are predominantly due to an anomalous low-level circulation imposed by sustained AWB that also facilitates the low-level advection of warm tropical air poleward and cool midlatitude air equatorward. Negative SST anomalies are evident in the JFM and AMJ SST correlation fields. There is also a second region of negative correlations in the subpolar gyre region, collocated with the correlation observed in U850. Correlations with Atlantic SSTs are also stronger in AMJ, indicating that the AWB-SST signal is a response to intense and persistent signals during the previous season.

Figure 3.3 shows the differences in composites of JFM environmental fields for the 12 highest values versus the 12 lowest values of the JAS PC2 index. The highest composites comprise the years 1990, 2018, 2003, 2015, 1994, 2002, 2014, 1984, 1989, 2013, 1992 and 2001; the lowest

composites comprise 2005, 2010, 1999, 1998, 1987, 1991, 2004, 1981, 1997, 2011, 1980 and 2006. The 'highest' composite years are listed in descending order from the highest PC2 value while the 'lowest' composite years are listed in ascending order from the lowest PC2 value. Winters with the highest values show signatures of wave breaking. Figure 3.3a displays two pronounced regions of high SLP anomalies, indicative of wave breaking over the Atlantic and along the western US coast. The SLP composite is also indicative of a prominent positive NAO for high values of PC2. A positive NAO phase has been associated with an increase in subtropical Atlantic AWB in previous studies (Benedict et al. 2004; Woollings et al. 2008). Winters with high JAS AWB activity hint at a horseshoe pattern with positive SST anomalies in the subtropical Atlantic and lower SST anomalies in the tropical MDR (Figure 3.3b). This horseshoe pattern becomes more apparent and statistically significant during AMJ (Figure 3.2f). Figures 3.3c and 3.3d are dominated by wave breaking. This result suggests that for years with enhanced summer wave breaking, there was also enhanced wave breaking in the preceding winter season. In the JFM periods where JAS PC2 was highest, the NAO averaged 0.35 standard deviations, while in the 12 JFM periods where JAS PC2 was lowest, the NAO averaged -0.44 standard deviations. This difference hints at the significant role that the NAO plays in pre-conditioning the atmospheric environment for significant AWB during JAS.

Figure 3.4 shows composites of JFM 850-hPa and 200-hPa geopotential height anomalies for the 12 highest versus the 12 lowest values for the JAS PC2 index. For years with pronounced summer AWB, there is a poleward-shifted subtropical jet and a low-level subtropical high indicative of an anomalous anticyclonic circulation over the Atlantic region. Both features are associated with increased winter wave breaking. The 12 highest height composite also suggests that above-normal summer AWB is associated with a positive-phase winter NAO. By contrast, in years with less summer AWB, 200-hPa height anomalies show little indication of anticyclonically sheared wave breaking. Instead, the 850-hPa subtropical high is anomalously weak (e.g., anomalously low pressure) due to an equatorward shift of the subtropical jet. An equatorward displacement of the subtropical jet is indicative of cyclonic wave breaking on the poleward side of the jet and a negative phase of the NAO. The most significant changes in the composites are situated over the Atlantic

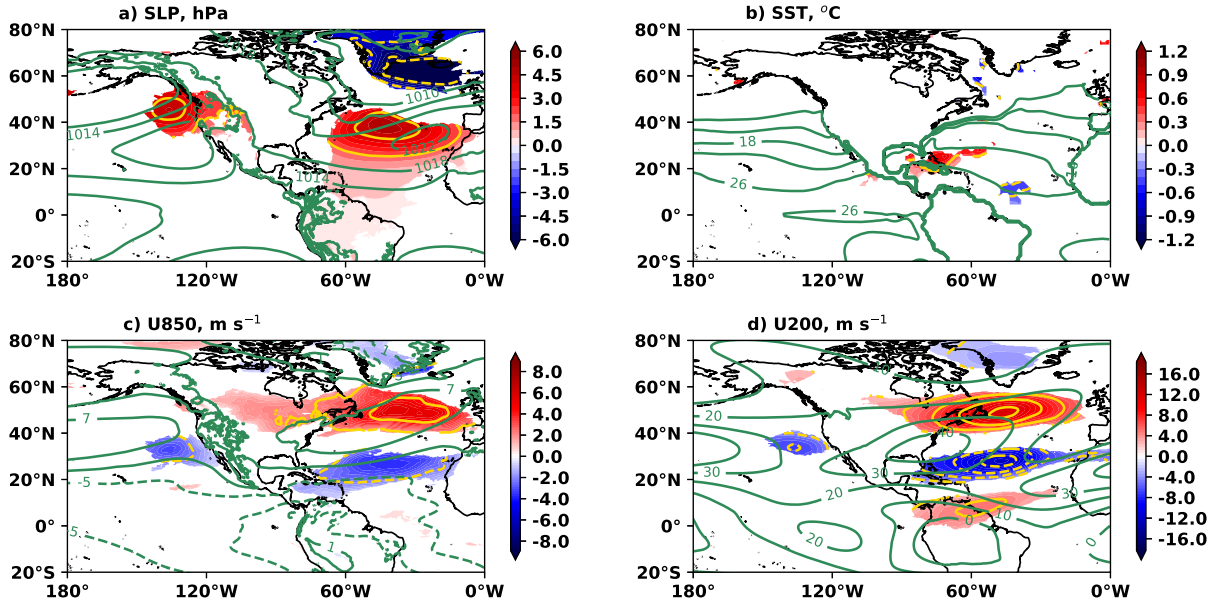

Figure 3.3: Differences in January-March (T-2 seasons) composites of the 12 highest values versus 12 lowest values for the second leading mode of July-September (T-0 seasons) VWS variability (PC2) for (a) sea surface temperatures (SST, ^{o}C), b) sea level pressure (SLP, hPa), c) 850-hPa U (U850, m s^{-1}), and d) 200-hPa U (U200, m s^{-1}).

and the western US coast, indicating that the dynamical difference between the composites is likely due to wave breaking and associated variations in the NAO. We also note that seasonal mean fields show a smooth spatial pattern that prevents us from observing actual RWB events.

Similar patterns are observed for the composites of AMJ 850-hPa and 200-hPa geopotential height anomalies (Fig. 3.5). The composite difference displays a low-level high over the subtropical Atlantic, similar to a positive phase of the NAO, when high values of the JAS PC2 index are present. At upper levels, the anticyclonically sheared signal is less pronounced in the AMJ composites (in contrast to the AMJ composites in Fig. 3.4) and is associated with a prominent low-level high over the subtropical Atlantic region. We note that the lack of an AWB signal in upper-level height anomalies may be due to seasonal shifts in the vertical location of wave breaking frequency (Kunz et al. 2015). Though there are some differences at upper levels for the tropical and extratropical regions, composite differences in the subtropical Atlantic are relatively weak.

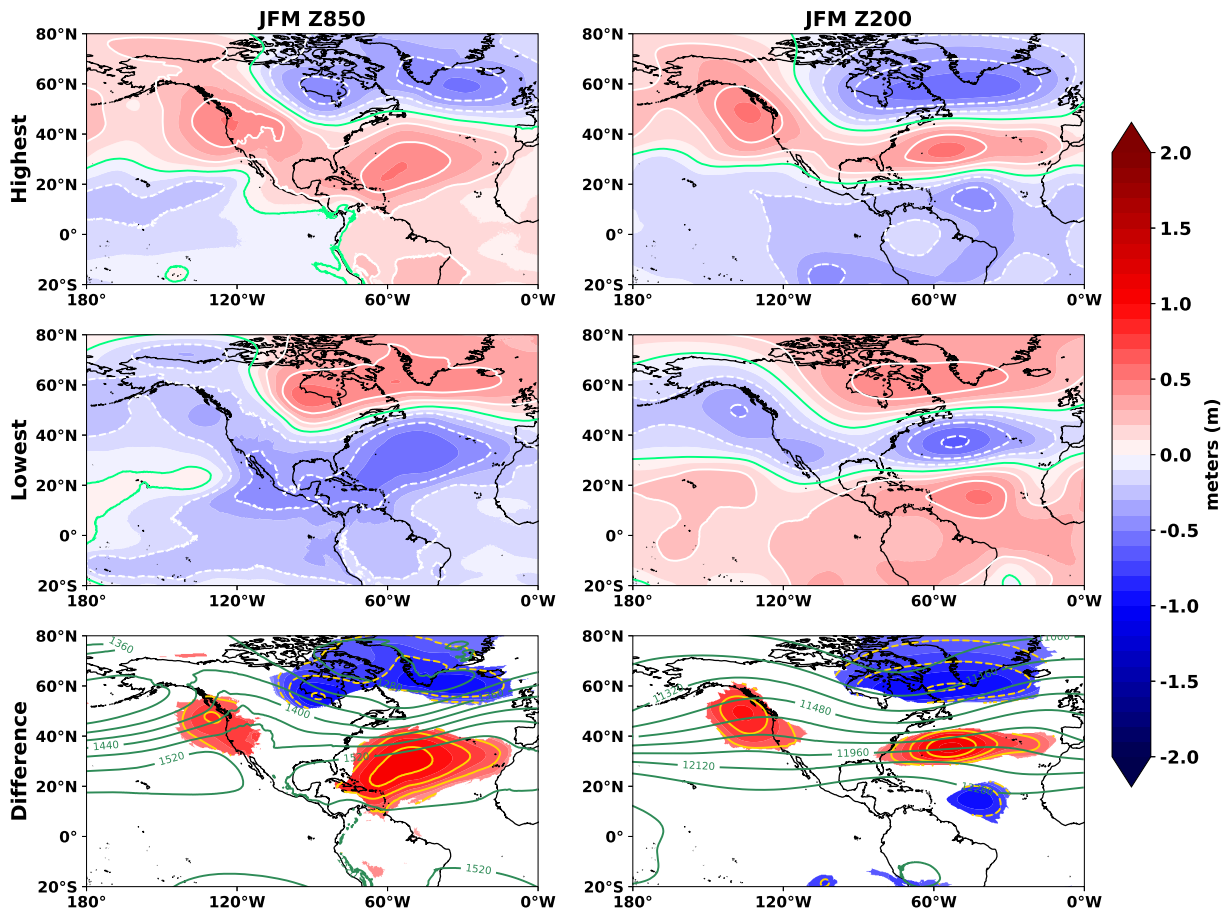

Figure 3.4: Composites of January-March (T-2 seasons) 850-hPa and 200-hPa geopotential height anomalies (in m) for the 12 highest values (top) versus the 12 lowest values (bottom) for the July-September (T-0 seasons) PC2 index. White contours (and gold contours in bottom panels) indicate intervals of 0.2 m; green contours highlight the zero anomaly contour.

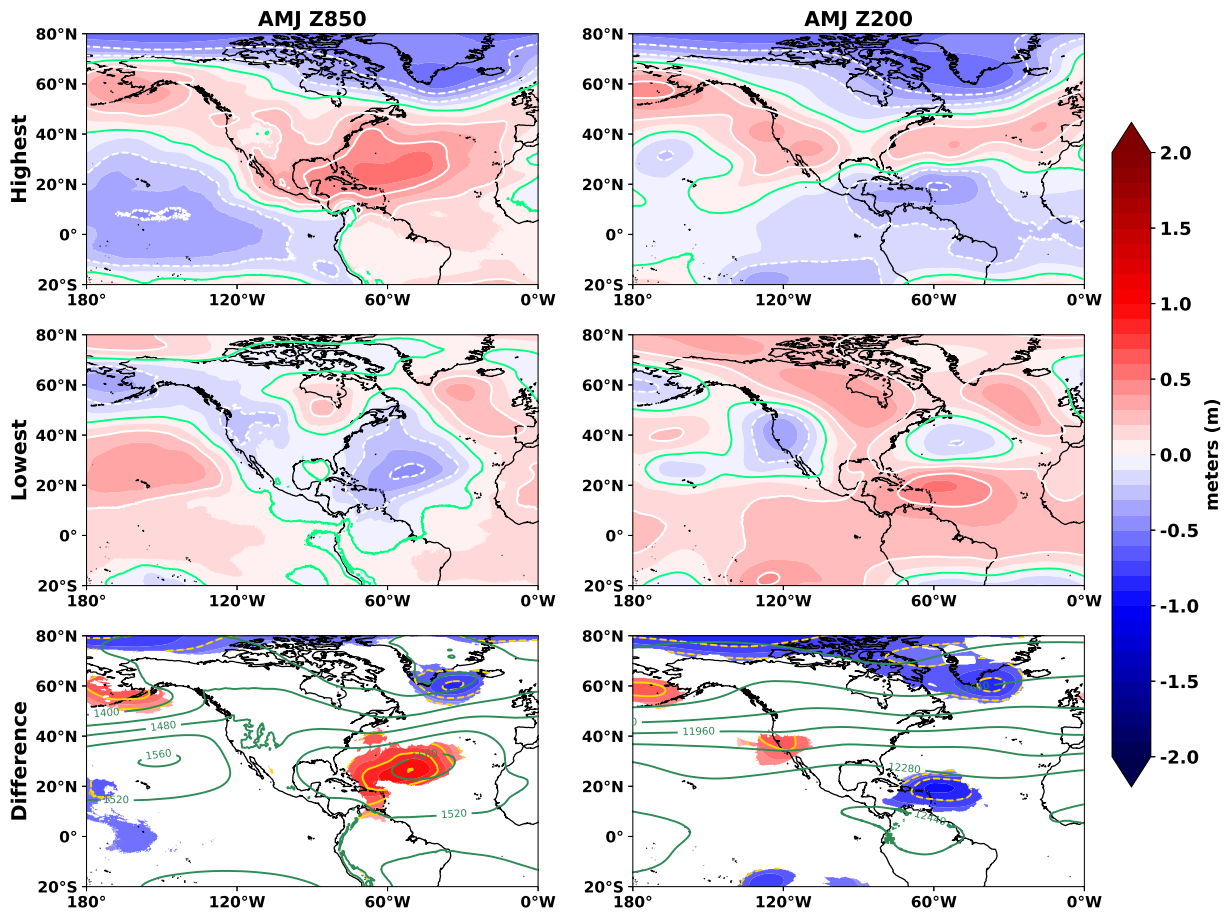

Figure 3.5: Composites of April-June (T-1 season) 850-hPa and 200-hPa geopotential height anomalies (in m) for the 12 highest values (top) versus the 12 lowest values (bottom) for the July-September (T-0 seasons) PC2 index. White contours (and gold contours in bottom panels) indicate intervals of 0.2 m; green contours highlight the zero anomaly contour.

3.3.2 The $U200_{proj}$ index

As described in section 3.2, the strong correlation pattern between JAS AWB-S_{summer} index and JFM zonal wind anomalies (shown in the inset of Figure 3.6) was projected onto an index of JFM subtropical Atlantic 200-hPa zonal winds averaged over 5^oN-80^oN and 80^oW-10^oW using Eq.3.1 and the method outlined in section 2b. Therefore, the subsequent index (hereafter, $U200_{proj}$) is a measure of how strong the winter-summer relationship was for each year. We note here that AWB activity shows strong variability in multiple environmental fields that likely contain a significant winter-summer AWB correlation (e.g., the SLP anomaly fields). For this section, we focus on the evolving pattern of variability in the 200-hPa zonal wind field.

Figure 3.6 compares the $U200_{proj}$ index to the summer AWB-S and PC2 indices. The correlations between these three indices are outlined in Table 3.1. For the period 1979-2019, the $U200_{proj}$ index has correlations of $r = 0.66$ and $r = 0.45$ with JAS PC2 and AWB-S_{summer}, respectively, and illustrates that the winter $U200_{proj}$ index is a good indicator of summer AWB-S variability. Correlations between the $U200_{proj}$ index and the August-October environment are given in Figure 3.7, which indicates that the index's associations are particularly significant in the Caribbean region. The $U200_{proj}$ index is associated with anomalously high SLPs, anomalously cool SSTs and anomalously strong VWS in the Caribbean region. All of these conditions typically suppress Atlantic hurricane activity (Jones et al. 2020). A prominent El Niño signal is also evident in the SST correlations. Jones et al. (2020) and **?** have shown that AWB activity has a positive correlation with ENSO. The patterns shown in Figure 3.7 are consistent with the current understanding of AWB's environmental impacts.

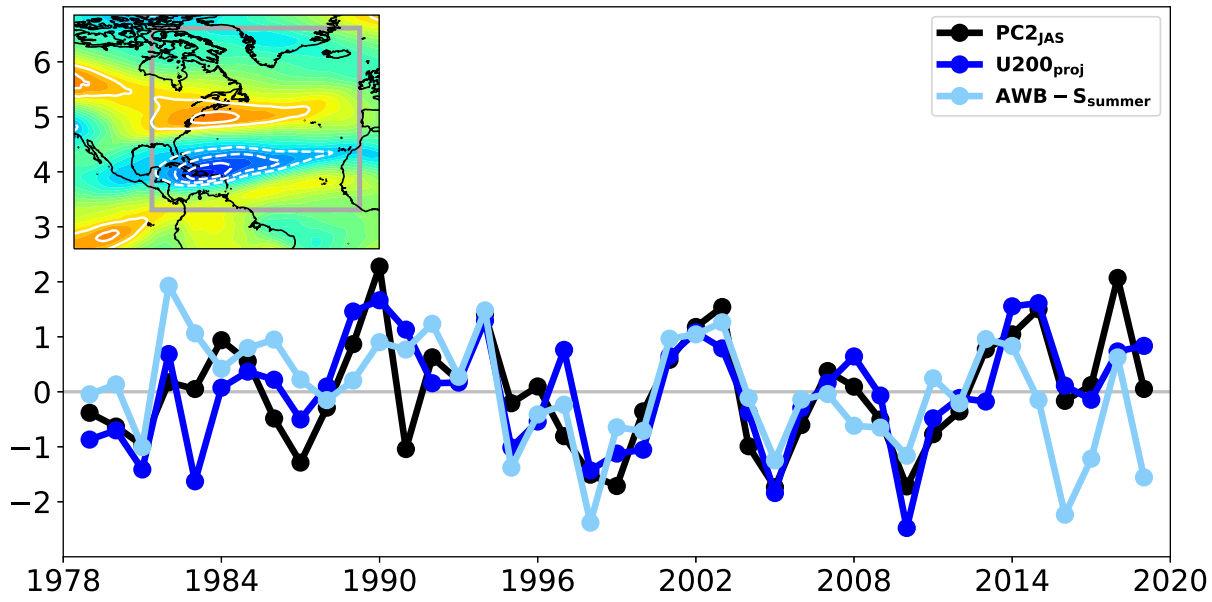

Figure 3.6: Time series comparison of the January-March (T-2 season) AWB-associated vertical wind shear index ($AWBs_{winter}$), July-September (T-0 seasons) AWBs index ($AWBs_{summer}$) and the $U200_{proj}$ index for the period 1979-2019. All indices are standardized over the period 1981-2010.

Table 3.1: Correlation coefficients between 1979-2019 July-September ($AWB\text{-}S_{summer}$) AWB shear indices, the $U200_{proj}$ index, and January-March 200-hPa zonal wind anomalies. Correlations statistically significant at the 95% significance level are highlighted in bold.

	$AWB\text{-}S_{summer}$	$U200_{proj}$	$U200_{subtropical}$
$AWB\text{-}S_{summer}$	-	**0.45**	**-0.40**
$U200_{proj}$	**0.45**	-	**-0.81**
$U200_{subtropical}$	**-0.40**	**-0.81**	-

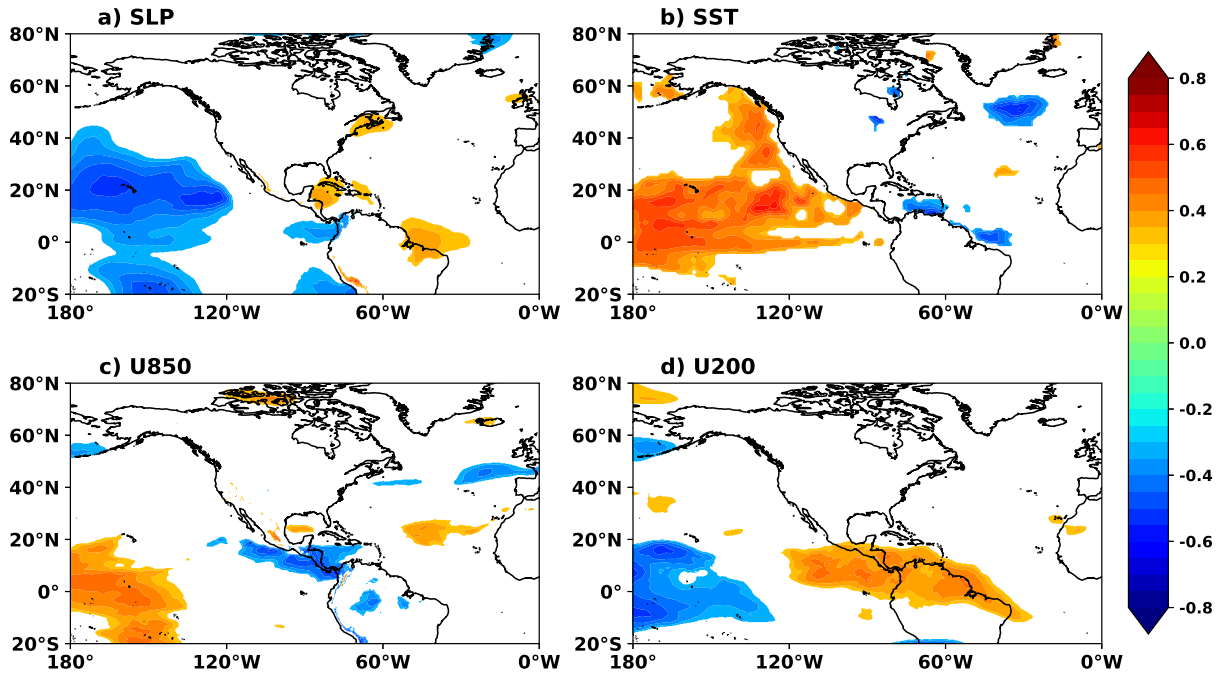

Figure 3.7: Pearson correlation coefficients between the $U200_{proj}$ index and August-October a) SLP, b) SST, c) U850, and d) U200 fields for the period 1979-2019. Colored shading indicates statistical significance at the 95% level.

3.3.3 The role of the NAO in AWB-S persistence

Figure 3.8a shows the monthly time series of $U200_{proj}$, NAO and ENSO indices from 1979 to 2019. At zero-lag, $U200_{proj}$ has insignificant correlations with the NAO ($r_{\text{NAO}} = 0.15$) and ENSO ($r_{\text{Niño3.4}} = 0.06$). The results of the cross-spectrum analyses shown in Figures 3.8b indicate that $U200_{proj}$ and NAO share a period of 3 months with a coherence of 0.49, significant at the 95% confidence level. The quadrature spectrum shows a positive phase difference of 1 month when the $U200_{proj}$ leads the NAO, as shown in Figure 3.8c. Therefore, the strong winter AWB tends to precede a positive NAO by 1 month. The cross-spectrum analysis shows that $U200_{proj}$ is associated with low-frequency variations in the NAO. Furthermore, the persistence of AWB-associated 200 hPa zonal wind anomalies observed earlier in section 3.3.1 is facilitated by AWB's forcing of the NAO on seasonal timescales. This result is consistent with $U200_{proj}$ being a projection of the subtropical component of VWS variability (PC2). The result is also consistent with earlier

observations by Benedict et al. (2004) and Woollings et al. (2008) of AWB forcing low-frequency variations in the NAO.

The phase of the NAO has previously been linked to variations in the location and strength of the Atlantic jet stream (Martius et al. 2008; Woollings et al. 2008, 2010; Zhang et al. 2016). Positive NAO anomalies re-enforce the anticyclonically sheared circulation that triggers further AWB in the vicinity of the subtropical high, while negative anomalies are associated with more cyclonically sheared flow and a decline in AWB, leading to more CWB (Martius et al. 2008). While very few studies have examined the NAO and AWB during AMJ, we infer that positive (negative) AMJ geopotential height anomalies associated with positive (negative) winter AWB-S (shown in Figures 3.4 and 3.5) encourage more (less) AWB in consequent seasons.

3.4 AWB inclusion in an early April extended-range forecast for Atlantic hurricane activity

In Section 3.3, we show that winter AWB activity can be used to estimate the intensity of summer wave breaking activity. We also show that abnormally strong winter AWB activity can force a positive phase of the NAO that lags AWB activity by a month. Franzke et al. (2004) suggested that the AWB-forced NAO anomalies may be sustained well into the summer by continued wave breaking throughout the year (see Figure 3.3). We have therefore interpreted the $U200_{proj}$ index to be a quantitative indication of the persistence of AWB-forcing on upper-level winds via the strength of the winter-summer link. Table **??** shows that $U200_{proj}$ has statistically significant correlations of $r = -0.35$ and $r = -0.41$ with ACE and the number of hurricanes, respectively. These results suggest that the perceived winter-summer persistence in AWB activity via forcing of the low-frequency NAO variability could be used to provide additional skill to extended-range forecasts of seasonal TC activity, particularly for seasons with unusually suppressed TC activity like the 2013 season.

The JFM U200proj index's contribution to skill is best demonstrated with CSU's 2020 early April forecast scheme (Klotzbach et al. 2020a). Below, we compare the performance of the previous 2019 CSU early April forecast statistical scheme to that of the revised 2020 early April scheme (Klotzbach et al. 2019). The 2019 forecast scheme is hereafter referred to as the 'original model',

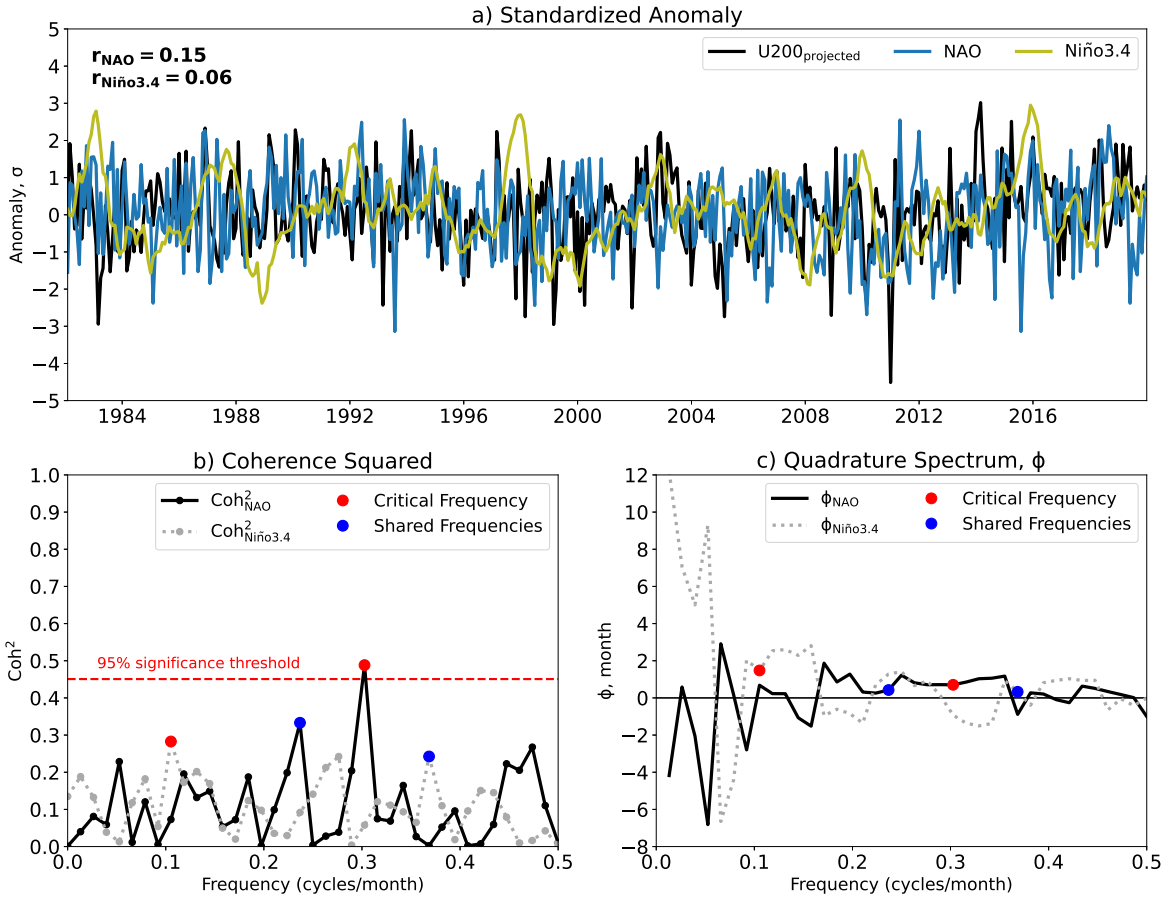

Figure 3.8: Cross-spectrum analyses between standardized monthly variations in the $U200_{proj}$ index, NAO, and Niño 3.4 indices for the period 1979-2019. (a) Time series plots of monthly standardized $U200_{proj}$ (black), NAO (blue), and Niño 3.4 (green) indices. (b) The coherence squared between $U200_{proj}$ and NAO (Coh_{NAO}, solid black line) and $U200_{proj}$ and Niño 3.4 ($Coh_{Niño3.4}$, dashed gray line). The critical frequency at which the coherence squared is strongest in each spectrum is highlighted by the red dot, while shared frequencies are shown in blue. The threshold for 95% significance is highlighted by the dashed red line. (c) Phase difference between the $U200_{proj}$ index and the NAO (solid black line) and Niño 3.4 (dashed gray line) indices. The red dot highlights the phase difference at the critical frequency. Positive (negative) phase differences indicate that $U200_{proj}$ leads (lags) the climate indices.

Table 3.2: Correlation coefficients between 1979-2019 June-November metrics of TC activity (ACE, total number of named storms, total number of hurricanes, total number of major hurricanes, and total number of hurricane and major hurricane days) and the January-March (AWB-S_{winter}) and July-September (AWB-S_{summer}) AWB shear indices, and the $U200_{proj}$ index. Values highlighted in bold indicate correlations statistically significant at the 95% level.

	AWB-S_{summer}	$U200_{proj}$
ACE	**-0.61**	**-0.35**
Named Storms	**-0.54**	-0.27
Hurricanes	**-0.56**	**-0.41**
Hurricane Days	**-0.51**	-0.23
Major Hurricanes	**-0.60**	-0.23
Major Hurricane Days	**-0.51**	**-0.38**

while the 2020 forecast scheme is referred to as the 'revised model'. Table **??** lists the statistical predictors used in Colorado State University's 2019 early April extended range forecast scheme, the regions over which the predictors were averaged, and their correlation with June-November ACE (Klotzbach et al. 2019).

The original statistical scheme includes the following as predictors: January-March SSTs over the North Atlantic region, March Atlantic SLP, February-March Pacific SLP, and forecast values of the September Niño 3 index from the SEAS5 dynamical model from ECMWF (Table 3.3). Anomalously warm Atlantic SSTs in January-March are generally associated with the positive phase of the Atlantic Multidecadal Mode (AMM) and an active TC season (Klotzbach and Gray 2008). Warmer SSTs are also associated with weaker lower and upper tropospheric winds, weaker vertical wind shear, and anomalously low sea level pressure over the Atlantic MDR during August-October. High SLP anomalies are associated with a stronger Azores High and cooler SSTs in the subtropics which is an indication of a less favorable environment for TC development. The third predictor, February-March southeastern tropical Pacific SLPs, is associated with lower SLP anomalies, weaker low-level wind anomalies over the Atlantic MDR and Caribbean regions and cooler SSTs in the eastern equatorial Pacific during August-October. These are conditions consistent with a La Niña event. The fourth predictor, predicted September Niño 3 SSTs, are an indicator of the state

of ENSO during the peak hurricane season and are consequently negatively correlated with TC activity ($r = -0.48$). Warmer Niño 3 SSTs are associated with El Niño conditions and an increase in vertical wind shear over the Atlantic, while cooler Niño 3 SSTs are associated with La Niña conditions and a reduction in vertical wind shear.

Table 3.4 lists the three statistical predictors used for the revised early April model. The revised statistical scheme includes the JFM tropical-subtropical eastern Atlantic SSTs retained from the original scheme, JFM subtropical Atlantic 200-hPa zonal winds, and JFM Coral Sea SSTs. The new JFM subtropical Atlantic U200 predictor correlates well with the $U200_{proj}$ index for the period 1982-2019 ($r = -0.81$, shown in Table **??**) and is associated with a weaker-than-normal Azores High, weaker trade winds, and higher SSTs over the Atlantic MDR. Higher than normal Coral Sea SSTs are typically associated with lower pressure over the western Pacific and higher pressure over the eastern Pacific. This pressure gradient pattern favors enhanced tropical Pacific trade winds, inhibiting El Niño development. The 2020 early April statistical scheme has a correlation of $r = 0.66$ with 1982-2020 ACE, while the ACE correlation for the 2019 early April scheme is $r = 0.54$ for 1982-2020.

Table 3.3: List of predictor domains for the original 2019 CSU early April statistical scheme and the $U200_{proj}$ index, and the correlation r_{ACE} between each predictor and 1982-2020 accumulated cyclone energy (ACE).

Predictors	Region	r_{ACE}
Jan-Mar Atlantic SSTs	5^{o}S-35^{o}N, 40^{o}W-10^{o}W	0.52
March North Atlantic SLP	20^{o}N-40^{o}N, 35^{o}W-20^{o}W	-0.18
Feb-Mar South Pacific SLP	20^{o}S-5^{o}S, 120^{o}W-85^{o}W	0.23
Predicted September Niño 3	5^{o}S-5^{o}N, 150^{o}W-90^{o}W	-0.33

Figure 3.9 shows the individual *F*-values of each predictor in the original and revised forecast schemes. The *F* and p values are determined from the correlation between ACE and each individual predictor. Therefore, the statistical values measure the strength of the relationship between each predictor and ACE. Here, we consider the *F*-value of the predictor to be statistically significant if

$F_{\text{critical}} > 2.01$, yielding a $p < 0.1$. The predictors of the revised forecast scheme all outperform those of the original scheme. The JFM Atlantic SST predictor has the highest F-value with $F = 14$ and $F = 17$ for the original and revised schemes, respectively. In the revised model, the JFM U200 has an F-value of 9 while the Feb-Mar Coral Sea SST has an F-value of 14. Figure **??** compares the predictions made by the original and revised statistical models for the years 1982-2020. Both schemes were trained on 1982-2010 ACE values and then tested on the period 2011-2020. The mean absolute error (MAE) and the explained variance (r^2) scores for the revised 2020 scheme show strong improvements over the original for both the training and testing periods. The original scheme fails to explain any variance in ACE for the 2011-2020 period.

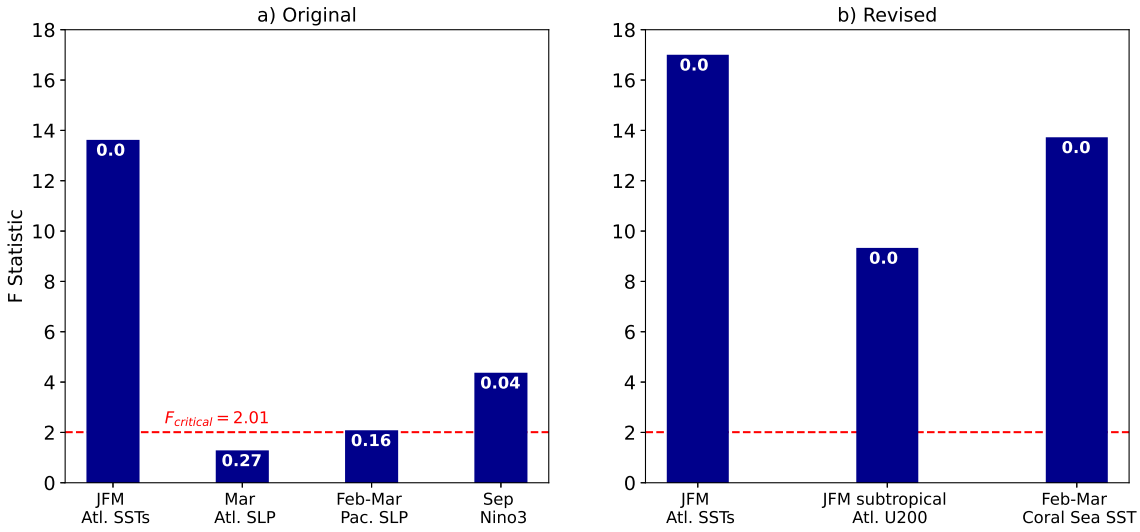

Figure 3.9: F-value statistic for each early April predictor in the a) original CSU 2019 and b) revised 2020 statistical Atlantic hurricane forecast models. Each predictor is labelled with the associated p-value. Statistically significant F-values exceed $F_{\text{critical}} = 2.01$ for $p = 0.1$.

3.5 Discussion and Conclusions

Recent studies have shown that subtropical anticyclonic wave breaking (AWB) influences seasonal North Atlantic tropical cyclone (TC) activity via AWB's forcing of tropical vertical wind

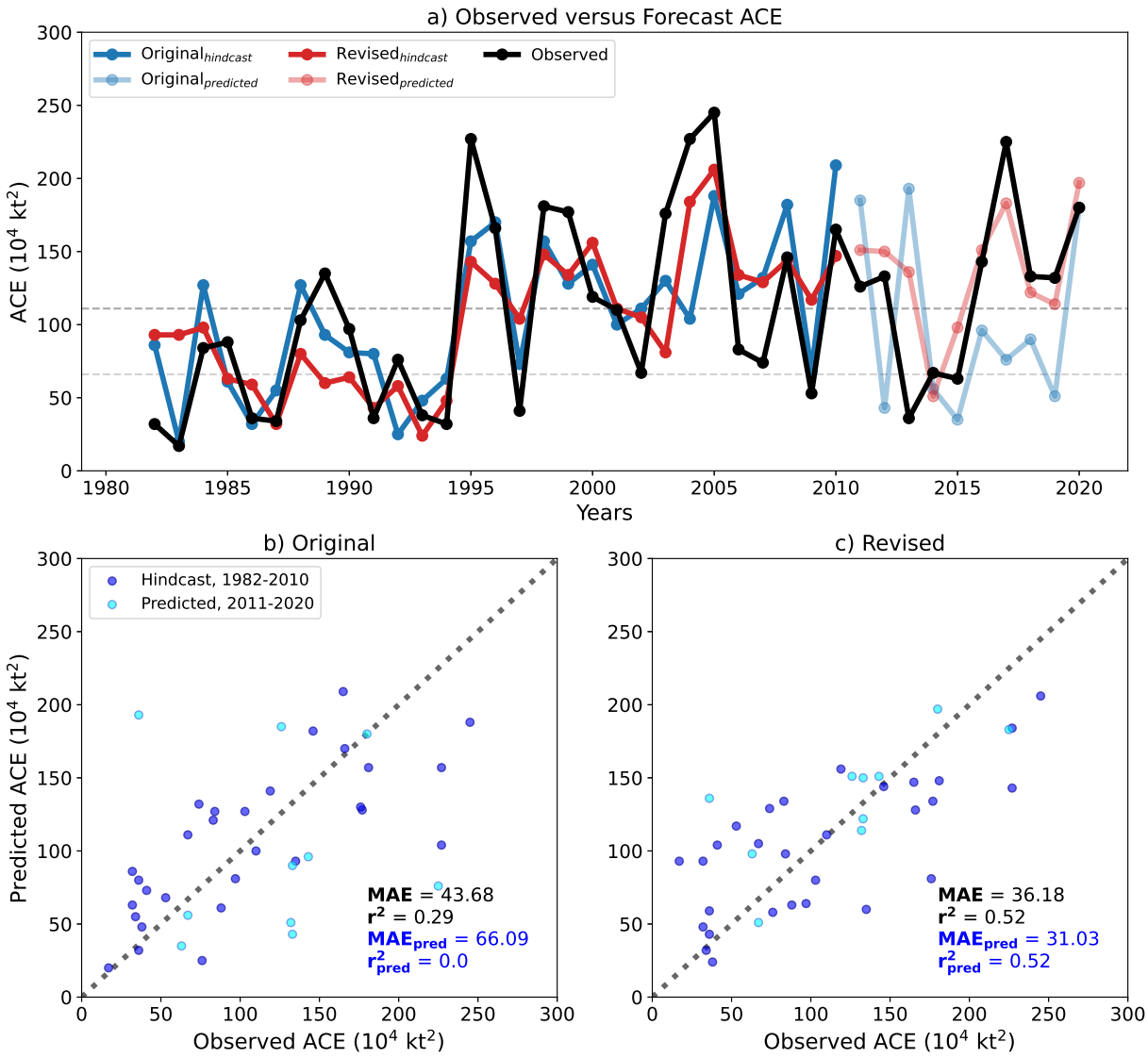

Figure 3.10: Linear regression performance of the original CSU 2019 early April statistical scheme and the revised CSU 2020 early April statistical scheme. a) Seasonal predictions of ACE based on the original early April statistical scheme without AWB (blue) and the revised scheme with AWB (red) versus observed ACE values (in black) from 1982-2020. Solid lines indicate the hindcast/training period from 1982-2010; transparent lines indicate the testing period from 2011-2020. Dark gray lines indicate near-normal activity between 66-111$\times 10^4$ kt^2. Levels exceeding 111$\times 10^4$ kt^2 are classified as above-normal while levels less than 66$\times 10^4$ kt^2 are classified as below-normal. These definitions are based on NOAA's Atlantic hurricane season classification criteria (CPC 2020). b) Scatter plots of ACE forecasted by the original 2019 forecast scheme. The original scheme comprises January-March Atlantic SSTs, March Atlantic SLP, FM Pacific SLP, and the forecast September Niño 3.4 index. c) Scatter plots of ACE forecasted by the revised 2020 forecast scheme. The revised scheme (right panel) consists of JFM Atlantic SSTs, JFM subtropical Atlantic U200, and Feb-Mar Pacific SLP. The mean absolute error (MAE) and variance explained (r^2) is given for the full 1982-2020 period (MAE, r^2) and the training period 2011-2020 (MAE$_{pred}$, r^2_{pred}).

Table 3.4: List of predictor domains for the 2020 CSU early April statistical scheme and the $U200_{proj}$ index, and the correlation r_{ACE} between each predictor and 1982-2020 accumulated cyclone energy (ACE).

Predictors	Region	r_{ACE}
January-March Atlantic SST	5^oS-50^oN, 40^oW-10^oW	0.56
Jan-Mar subtropical Atlantic U200	17.5^oN-27.5^oN, 60^oW-20^oW	0.45
Feb-Mar Coral Sea SST	20^oS-0^o, 145^oE-170^oE	0.52

shear (VWS) (Zhang et al. 2016, 2017; Papin et al. 2020). An index representing summer AWB-associated environmental anomalies provides one way of quantifying AWB's impact on the Atlantic MDR, adding skill to seasonal predictions of TC activity (Jones et al. 2020). In this study, we examine the use of the strong winter environment/summer AWB-shear link to assess the predictability of AWB impacts on seasonal TC activity and show that including the dynamical effects of AWB is useful in seasonal TC predictions. The key findings of our study are as follows:

1. There is a strong association between winter and summer AWB shear impacts. Correlations significant at the 95% confidence level between the July-September (JAS) AWB-shear index and the January-March (JFM) 200 hPa zonal wind field show anticyclonically sheared wind anomalies that indicate wave breaking.

2. The strength of the winter-summer AWB relationship is an indication of wave breaking-induced NAO anomalies. Continuous wave breaking sustains seasonal NAO anomalies and provides a physical explanation for persistence in seasonal AWB shear impacts.

3. Potential impacts of summer wave breaking on TC activity can be estimated by projecting an index of January-March 200-hPa zonal wind anomalies onto the winter-summer AWB relationship, denoted here as $U200_{proj}$.

4. The $U200_{proj}$ index is significantly correlated at -0.35 with ACE and 0.45 with summer AWB-shear indices. The revised early April statistical seasonal hurricane forecast model from CSU including an index closely related to $U200_{proj}$ improves upon CSU's 2019 early April extended-range statistical forecast from 1982-2020.

The results of this study show that AWB-associated 200 hPa zonal wind anomalies are persistent within the environment through their low-frequency covariability with the quasi-stationary NAO. The low-frequency AWB-NAO relationship explains the strong correlations we observed between winter AWB and summer AWB shear impacts, and improves the extended-range skill of seasonal TC predictions. We also suspect that the $U200_{proj}$ index can account for above or below-normal subtropical Atlantic TC variability and offer added skill in years with ENSO-neutral conditions where the predictability of the large-scale environment is reduced (Saunders et al. 2020; Wood et al. 2020).

One limitation of the $U200_{proj}$ index is due to the strong nonlinear component of AWB variability. This means that the winter-summer link and the $U200_{proj}$ index do not always account for the magnitude of summer wave breaking impacts. The $U200_{proj}$ index only accounts for 16% of the explained variance in the summer AWB-shear index and may be underwhelming as a predictor in multiple linear regressions alongside the strong forcing from ENSO-related predictors. This limitation raises a key question about TC prediction: *Are current schemes sophisticated enough to pick up the subtle dynamical forcing (e.g., for AWB) that may drive the large-scale atmospheric circulation, especially during ENSO-neutral conditions?* We intend to investigate the use of nonlinear regression techniques for Atlantic TC prediction in future work to answer this question.

Chapter 4

An Examination of Seasonal North Atlantic Vertical Wind Shear Variability in the CESM1 Large Ensemble

4.1 Introduction

Global climate models or general circulation models (GCMs) have previously been used to examine many aspects of TC-like variability within the general circulation (Camargo and Wing 2016). Initial work documented the ability of early models to capture the structure of hurricane-like vortices, their climatology and modulation by known large-scale climate phenomena, and demonstrated the versatility of model simulations.

Many consequent studies following the aforementioned works have expanded our understanding of TC variability with changes in large-scale drivers such as El Niño-Southern Oscillation (ENSO; Camargo et al. 2007; Patricola et al. 2018), the dynamic and thermodynamic structure of TC vortices (Moon et al. 2018, Wing et al. 2019), and projected changes in TC variability with a warming climate (Ting et al. 2019, Emanuel 2020, Murakami et al. 2020, Walsh et al. 2020). More recently, studies such as Wang et al. (2018) and Stansfield et al. (2020) have also shown that GCMs can be used to examine variations in TC-associated rainfall and their response to climate change.

As GCM model physics improve and resolution increases, these models have provided useful information for the prediction of subseasonal to multiyear TC activity through earth system prediction (Camargo and Wing 2016). Therefore, GCMs can provide forecasts of the global or regional state of the earth system from which forecasters can estimate TC activity. An example of this is the UK Met Office's Global Seasonal Forecast System 5 (GloSEA5; Camp et al. 2015) that is based on their coupled Hadley Center Global Environment Model version 3 (HadGEM3)

GCM. Klotzbach et al. (2020)'s hybrid statistical-dynamical model utilizes SEAS5 forecasts from ECMWF of July 2-m air temperature, and 10-m and 200-hPa zonal wind speeds to predict seasonal North Atlantic TC activity. Other GCMs used to predict TC activity include the Geophysical Fluid Dynamics Laboratory(GFDL) High-Resolution Atmospheric Model (HiRAM; Gao et al. 2018, 2019) and the Japan Meteorological Agency/Meteorological Institute-Coupled Prediction System (JMA/MRI-CPS2; Takaya et al. 2010, 2017).

Much of the seasonal TC prediction skill provided by GCMs is a result of a robust canonical ENSO signal within the tropical atmospheric circulation (Camargo et al. 2007; Shaevitz et al. 2014; Wang et al. 2014; Camp et al. 2015). ENSO's modulation of the large-scale atmosphere is particularly important for the variability in one key environmental predictor - vertical wind shear (e.g. Gao et al. 2019). As mentioned earlier in Chapter 1 (Introduction), Gray (1968) found that TCs tended to form in regions and seasons of climatologically low VWS. He noted in later work (Gray 1984) that North Atlantic VWS, and thus North Atlantic TC activity, was strongly modulated by ENSO. During El Niño events, there was an increase in VWS and lower-level divergence over the North Atlantic resulting in a suppression of TC activity, while La Niña events were associated with a decrease in VWS and low-level convergence over the North Atlantic region. Therefore, the persistence of ENSO's variability and its strong modulation of the large-scale circulation accounts for much of the predictability in VWS (Aiyyer and Thorncroft 2006, 2011).

But, as shown in Chapter 2, seasonal North Atlantic VWS has distinct modes of variability that are associated with both tropical and subtropical large-scale drivers. Other than ENSO, large-scale VWS drivers include Atlantic SST variability, subtropical North Atlantic anticyclonic AWB, the Walker Circulation and African Sahel rainfall. In Chapter 3, we further showed that subtropical drivers of VWS such as anticyclonic Rossby wave breaking (AWB) and its covariability with the North Atlantic Oscillation (NAO) provide alternative sources of TC predictability. While many studies have discussed the impact of ENSO on TCs via VWS variability, few have looked at the impact of other large-scale drivers on VWS. Given that ENSO is not the only source of VWS

predictability, can non-ENSO drivers provide additional skill for TC prediction models during ENSO-neutral phases?

To answer this question, we require a large sample size, as reanalysis datasets provide a limited sample of environments driven by independent phenomena (Jones et al. 2020). The most reliable reanalysis datasets extend only back to 1979 - the era of global satellite coverage. One solution is to use 'big data' or large ensembles of earth system model output. Climate model ensembles are useful for providing multiple representations of the environment along with an increase in sample size. For example, Krishnamurthy et al. (2016) used the long-control simulations of the GFDL FLOR to examine the impact of ENSO strength on TC activity in the Western North Pacifc, Eastern North Pacific and North Atlantic basins.

In this study, a similar strategy is employed, in which we examine seasonal drivers of VWS over the Atlantic Main Development Region (MDR) in the Community Earth System model version 1.1 Large Ensemble (CESM1-LE). The analysis outlined in Chapters 2 is applied to the CESM1-LE and is later used to examine non-ENSO associated VWS variability during ENSO neutral conditions. The key science questions in this chapter are as follows:

- What drives tropical North Atlantic vertical wind shear within the CESM1 Large Ensemble?
- How do known climate phenomena other than ENSO impact VWS, especially during ENSO-neutral conditions?
- What can this tell us about the predictability of TCs during ENSO-neutral TC seasons?

This chapter is outlined as follows: section 4.2 describes the CESM1-LE in more detail and the methods used. Section 4.3 outlines the characteristics of VWS variability within the large ensemble and how it compares with reanalysis. Section 4.4 characterizes the modes of variability in the CESM1-LE and the state of VWS variability during ENSO neutral conditions. Section 4.5 provides a brief discussion of the analysis results and presents some conclusions.

4.2 Data and Methods

4.2.1 Data

As in Chapter 3, the ECMWF's fifth generation global reanalysis dataset (ERA5) is used to represent the present-day large-scale atmospheric circulation. Recall that the ERA5 reanalysis has a horizontal resolution of 0.25^o x 0.25^o for the atmosphere and 0.5^o x 0.5^o for ocean waves and spans January 1979 to the present (Hersbach et al. 2020). The present study uses monthly 1979-2019 850-hPa and 200-hPa zonal winds to calculate deep-layer VWS.

The CESM1 CAM5 BGC Large Ensemble (hereafter referred to as CESM1-LE) consists of multiple representations of the CESM1.1 coupled GCM (Hurrell et al. 2013; Kay et al. 2015). The atmospheric component (CAM5) of the CESM1-LE has a nominal 1^o latitude-longitude resolution (1.2^ox0.9^o) with 32 vertical levels. CESM1-LE comprises:

- a 1000-year control run initialized in 1850
- 40 historical runs extending from 1850 to 2005; Run 1 is initialized from the 1850-control run while runs 2-35 are initialized from 1920.
- 40 forced runs from 2006 to 2100 under RCP8.5

For this analysis, the first 35 historical runs are used to calculate 1920-2005 Atlantic VWS. The historical runs are used to increase the sample size of seasonal VWS and provide multiple representations of large-scale atmospheric impacts on shear. Monthly fields of reference height temperature (TREFHT), zonal wind (U), 10-m horizontal winds (U10), sea level pressure (PSL), and convective precipitation rate (PRECC) are used in this analysis to derive and resolve known climate phenomena, and generate model proxies for the climate indices listed in Table 4.1 below.

VWS is defined as the difference between 200-hPa and 850-hPa zonal winds. The low pass-filtered data are subtracted from the original data to remove signals with periods larger than 4 months. To remove the seasonal cycle, anomaly fields are calculated relative to the 1979-2019 period for the ERA5 Reanalysis and 1920-2005 for the CESM1-LE.

4.2.2 Climate Indices

In this study, we considered five key climate indices based on Chapters 2 and 3: the El Niño-Southern Oscillation (ENSO), the Atlantic Meridional Mode (AMM), Atlantic Main Development Region (MDR) SSTs relative to the 30^{o}S-30^{o}N tropical belt (RSST), the North Atlantic Oscillation (NAO), and African Sahel rainfall. For comparisons with ERA5 reanalysis fields, we obtained the climate indices from the NOAA Climate Prediction Center's (CPC) and Physical Sciences Library's (PSL) online platform, publically available at https://psl.noaa.gov/data/climateindices/. Definitions for each climate index and key references are outlined in Table 4.1. All indices are given as standardized anomalies relative to the time period covered by the index, therefore 1979-2019 for observed indices and 1920-2005 for model-derived indices. The indices are also detrended to remove non-stationarity of the data over time.

Table 4.1: List of climate phenomena calculated for each CESM1-LE run, the domain over which they are defined and key references for their definitions.

Climate Index	Domain	Key Reference(s)
El Niño-Southern Oscillation (ENSO)	5^{o}S-5^{o}N, 170^o-120^{o}W	Trenberth (2020)
Atlantic Meridional Mode (AMM)	21^{o}S-32^{o}N, 74^{o}W-15^{o}E	Chiang and Vimont (2004) Kossin and Vimont (2007)
Main Development Region Relative SSTs (RSST)	10^o-20^{o}N, 85^o-20^{o}W minus 30^{o}S-30^{o}N	Johnson and Xie (2010)
North Atlantic Oscillation (NAO)	Azores High: 36^o-40^{o}N, 28^o-20^{o}W Icelandic Low: 63^o-70^{o}N, 25^o-16^{o}W	Smith et al. (2020)
African Sahel Rainfall	10^o-20^{o}N, 120^{o}W-10^{o}E	Mitchell (2013)

Consistent with the analysis of Chapter 2, ENSO variations are represented using the Niño 3.4 index over the region 5^{o}S-5^{o}N and 170^o-120^{o}W (Trenberth 2020). The Niño 3.4 SST index accounts for the first leading mode of VWS variability and is positively correlated with VWS over the Atlantic MDR ($r = 0.73$ from Table 2.2). For the CESM1-LE ensemble runs, TREFHT fields

(temperatures at model surface level height) serve as a proxy for SST fields and are used to derive a standardized Niño 3.4 index for each model run.

Another major driver of Atlantic VWS is the AMM (Chiang and Vimont 2004; Kossin and Vimont 2007). The AMM is defined as the leading mode of a maximum covariance analysis (MCA) applied to SST and U10 fields over the region 21^oS-32^oN and 74^oW-15^oE. A positive-phase AMM is generally associated with reduced VWS over the Atlantic MDR, while a negative-phase AMM is associated with increased MDR shear. Also, Kossin and Vimont (2007) and Patricola et al. (2014) both show that the AMM impacts VWS as much as ENSO and combined forcing by the two phenomena modulate VWS variability over the MDR. ENSO has a stronger modulation of VWS in the western tropical Atlantic/Caribbean while the AMM has a stronger modulation of VWS in the eastern tropical Atlantic (Kossin and Vimont 2007). TREFHT and U10 anomaly fields are used to calculate model representations of the AMM for each run.

Atlantic MDR RSSTs is the mean SST variability averaged over the region 10^o-20^oN and 85^o-20^oW relative to 30^oS-30^oN-averaged SST mean. As the globe warms, it is suggested that the SST threshold for tropical deep convection is steadily rising concurrently with increasing tropical mean SST (Johnson and Xie 2010). Therefore, RSST has become an important variable to consider for the ENSO modulation of convection (Williams and Patricola 2018) and tropical cyclogenesis (Villarini et al. 2011; Camargo et al. 2014). Increased RSSTs are associated with reduced VWS over the MDR.

Few studies draw links between the NAO and summer tropical Atlantic VWS variability. However, Chapter 3 shows that the NAO is also a source of VWS predictability and is associated with subtropical sources of VWS such as Rossby wave breaking. The positive phase of the NAO is associated with persistent anticyclonic wave breaking (AWB) leading to increases in VWS over the MDR, while the negative phase of the NAO indicates weaker AWB and reduced VWS (Jones et al. 2021). Another possible link to VWS is via the NAO's modulation of sea level pressure. Higher North Atlantic SLP anomalies are generally associated with a stronger Icelandic low, a

northeastward-shifted subtropical high, and stronger westerly trade winds over the MDR (Elsner et al. 2000; Wang and Lee 2007) resulting in higher VWS.

Aiyyer and Thorncroft (2006, 2011) show that African Sahel rainfall is also a key driver of tropical Atlantic VWS, particularly on multidecadal timescales. Jones et al. (2020) showed that African Sahel rainfall accounted for 8% of interannual VWS variability. A drier-than-normal Sahel is associated with a strengthening of upper-level westerlies and increased VWS over the MDR, while a wetter-than-normal Sahel is associated with a weakening of upper-level westerlies and reduced VWS (Landsea and Gray 1992). African Sahel rainfall indices were calculated from the CESM1-LE model ensembles by averaging PRECC anomalies over the African Sahel region (10^o-20^oN, 120^oW-10^oE).

Throughout the chapter, references are made to both linear and nonlinear components of VWS variability. Here, linear VWS variability is defined as having correlations greater than |0.2| with climate indices, while nonlinear variability is defined as that having weaker correlations less than |0.2|.

4.2.3 Characterizing Modes of VWS Variability

To characterize the modes of VWS variability within the model environment, the methods outlined previously in Section 2.2.2 were reapplied to the CESM1-LE. The first method applied is a composite analysis of July-September (JAS) VWS variability for the 525 highest versus 525 lowest values (15 highest and 15 lowest values per ensemble run) for each climate index listed in Table 4.1. The composites generated from the CESM1-LE are compared to those from the ERA5. VWS variability during neutral ENSO conditions is also examined. We also performed a residual analysis via linear regression to examine the independent spatial patterns of VWS variability associated with each climate index. Global JAS VWS anomalies from 1920-2005 from each CESM1-LE historical run were regressed against model representations of the climate indices. Mean correlations between the climate indices and CESM1-LE ensemble runs were calculated by taking the individual correlation for each run, then averaging across all runs for a mean value.

The second method was an eigenanalysis applied to July-September tropical VWS anomalies over the region 10^o-30^oN and 90^o-20^oW for the period 1920-2005 in each CESM1-LE run. The first four empirical orthogonal functions (EOFs) were obtained and compared to the patterns of VWS variability observed in ERA5.

4.3 VWS variability in the CESM1-LE

4.3.1 VWS Climatology

Figure 4.1 shows a comparison between the CESM1-LE ensemble mean 86-year (1920-2005) and 28-year (1979-2005) monthly North Atlantic VWS climatology and the 1979-2005 VWS climatology derived from ERA5. The monthly VWS climatology as represented by the 1979-2005 CESM1-LE is comparable to that shown by ERA5. Generally, in the CESM1-LE, mean tropical VWS is higher than ERA-5 from March to July. Unlike in ERA5, CESM1-LE's monthly climatological low in VWS is in September rather than August.

Figure 4.2 compares the mean 1979-2005 July-October VWS field for the ERA5 and CESM1-LE ensemble mean. While there is generally good agreement between the CESM1-LE and ERA5, VWS in the CESM1-LE tends to be higher over the western tropical Atlantic and subtropical Atlantic regions. However, VWS over the easternmost section of the Atlantic region is lower than observed. In general, the underlying VWS climatology in the CESM1-LE is comparable to reanalysis.

4.4 Model VWS Variability associated with Climate Phenomena

4.4.1 Composite Analysis

First, we examine what patterns of variability can be observed in simple VWS composites that are associated with the climate indices listed in Table 4.1 for ERA5 and CESM1-LE. Figure 4.3 shows scatter plots of VWS versus standardized indices of ENSO, RSST, AMM, NAO, and African Sahel rainfall for the period 1979-2019. Hereafter, we refer to VWS's relationships and correlations with the five climate indices as ENSO-VWS, RSST-VWS, AMM-VWS, NAO-VWS, and Sahel-VWS. Tropical Atlantic VWS anomalies in ERA5 show strong relationships

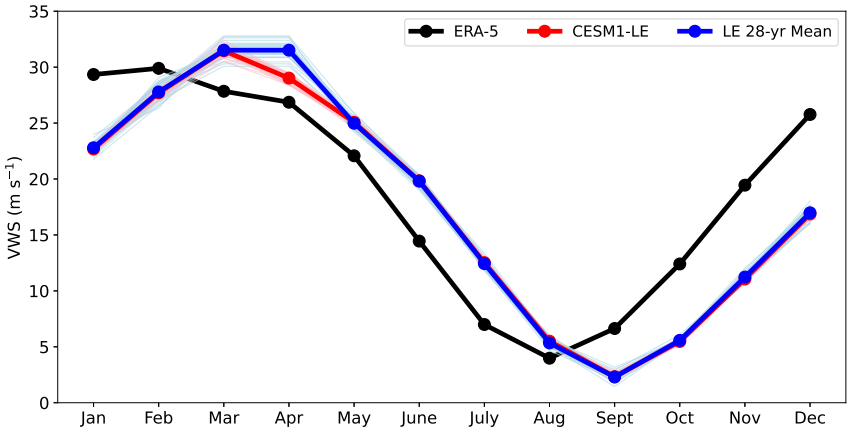

Figure 4.1: Monthly VWS climatology calculated over the Atlantic MDR derived from the CESM1-LE over the 86-year period 1920-2005 (pink) and 28-year period 1979-2005 (blue), compared to the ERA5 climatology over the period 1979-2005 (black). The ensemble mean is outlined in red. The monthly climatologies were generated using unfiltered data and model output.

with both ENSO and Atlantic SST variability. VWS's correlations with ENSO ($r = 0.55$), RSST ($r = -0.63$), AMM ($r = -0.46$), NAO ($r = 0.17$), and African Sahel rainfall ($r = -0.38$) are consistent with the analyses of Chapters 2 and 3 (see Table 2.2). Here, Figure 4.3 shows clearly the relationships of ENSO-VWS, RSST-VWS, AMM-VWS, NAO-VWS, and Sahel-VWS.

Figure 4.4 is similar to Figure 4.3, except for the CESM1-LE. Scatter plots of VWS versus the model standardized climate indices are highlighted in black, while the least squares lines of best fit are highlighted in red. While for ERA5, ENSO, RSST, AMM, and Sahel rainfall are key drivers of VWS variability, Figure 4.4 indicates that ENSO may be the only dominant driver of VWS in the CESM1-LE. ENSO-VWS and Sahel-VWS show similar correlations to those in Figure 4.3. ENSO-VWS, AMM-VWS, and Sahel-VWS have ensemble mean correlations of $r_{mean} = 0.51$, $r_{mean} = -0.31$ and $r_{mean} = -0.31$, respectively. RSST-VWS and NAO-VWS have weaker correlations. However, the weaker correlations do not necessarily rule out the RSST and the NAO as drivers of VWS in the CESM1-LE.

Figure 4.5 shows ERA5-VWS composites for the 10 highest versus the 10 lowest values of each of the five climate indices. As noted previously, ENSO is one of the strongest drivers of VWS. While there are robust RSST-VWS and AMM-VWS relationships, their highest and lowest com-

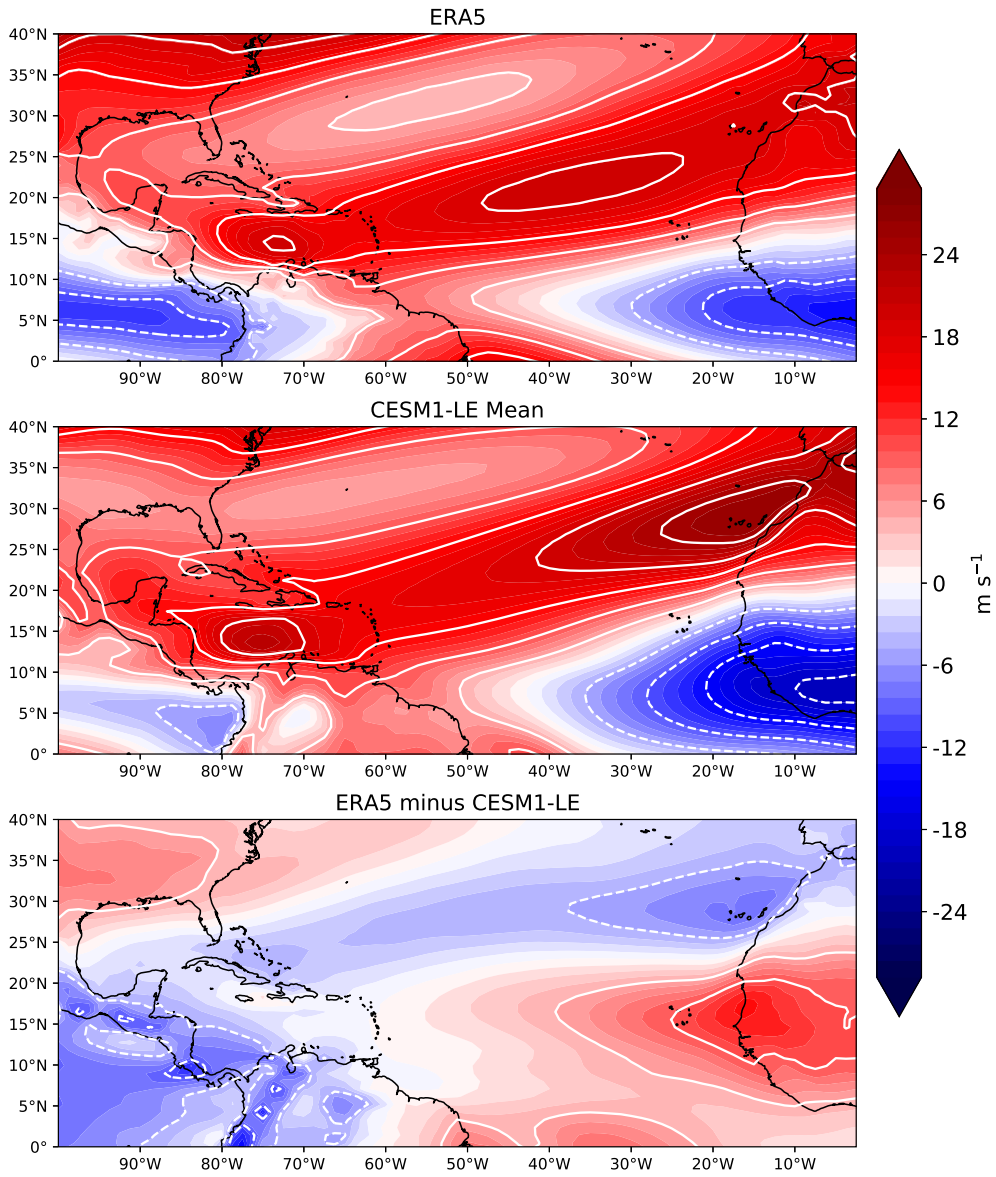

Figure 4.2: Mean July-October VWS (in m s^{-1}) averaged from 1979-2005 as represented by the a) ERA-5 reanalysis, b) CESM1-LE (mean of all 35 runs); c) difference between ERA-5 and the CESM1-LE. White contours are set at intervals of 8 m s^{-1}.

posites tend to overlap with those of ENSO, indicated by strong zonal VWS anomalies within the 20^{o}S-20^{o}N latitude band and significant VWS modulations in the western Atlantic and Caribbean. This pattern is expected for RSST due to the subtraction of the 30^{o}S-30^{o}N tropical mean and is driven by ENSO. This may be attributed to the small sample size for independent samples of each climate index over the period 1979-2019. Figure 4.5 highlights an important limitation of using

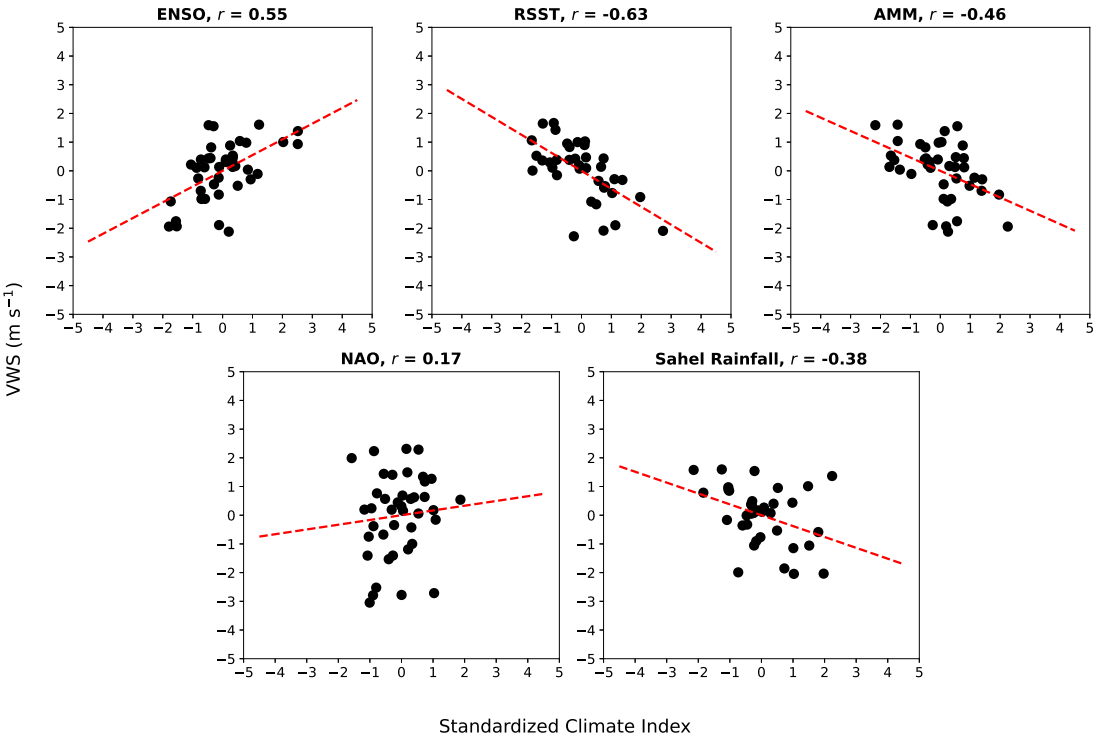

Figure 4.3: Scatter plots of 1979-2019 VWS anomalies generated from ERA5 versus standardized indices of ENSO, RSST, AMM, NAO, and African Sahel rainfall. The RSST scatter plot is for the period 1982-2019. Red dashed lines indicate the least squares line of best fit of the scatter plots.

reanalyses datasets to obtain samples of the environment, given the relatively limited number of years since ERA5 began in 1979.

Figure 4.6 shows the CESM1-LE equivalent of Figure 4.5. Each composite comprises 15 samples per ensemble run. This makes a total of 525 samples per composite. The signatures of each climate index are more distinct than those in Figure 4.5 and show clear differences from the characteristic ENSO signature. Also, while the overall correlations with tropical Atlantic VWS are weak, Figure 4.6 shows that there are stronger signals for subregional VWS variations. ENSO, RSST and Sahel rainfall show strong signals of VWS over the tropical western Atlantic and Caribbean. The AMM-VWS relationship is stronger in the eastern Atlantic region, while the NAO-VWS relationship is stronger over the subtropical and extratropical Atlantic region. Though there are distinct patterns attributable to the composites of each climate index in the CESM1-LE, it is evident that ENSO is the strongest driver of VWS.

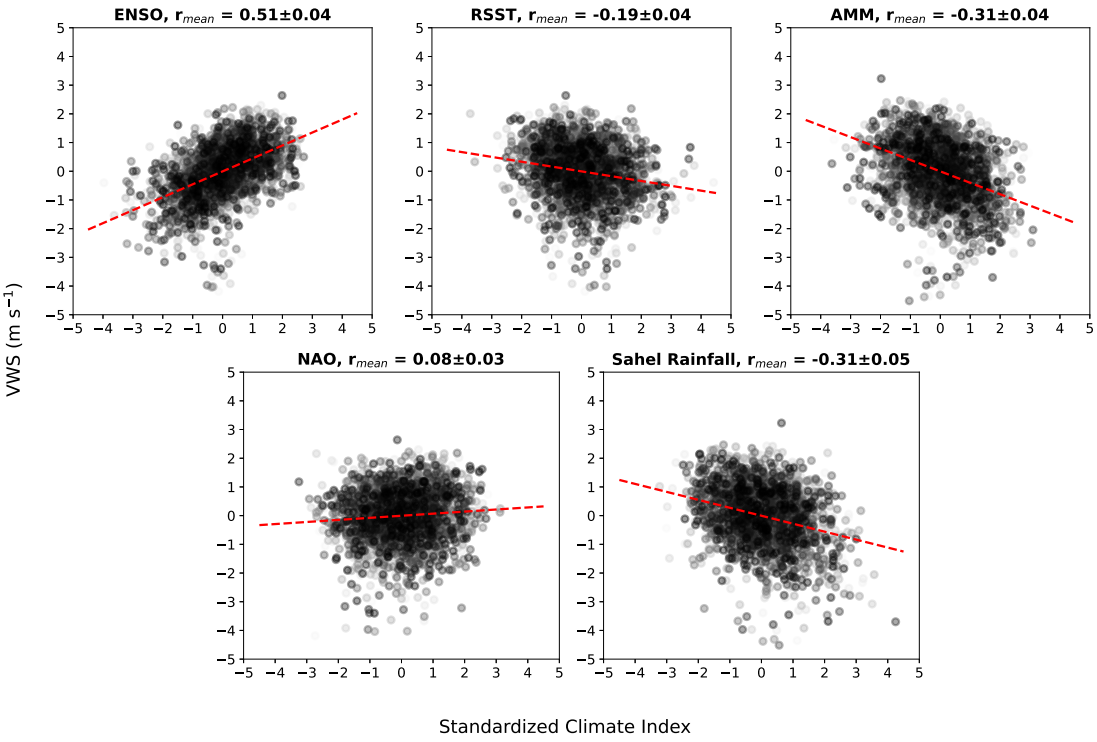

Figure 4.4: Scatter plots of 1920-2005 VWS anomalies versus standardized indices of ENSO, RSST, AMM, NAO, and African Sahel rainfall generated from each of the 35 runs in the CESM1-LE. Red dashed lines indicate the least squares line of best fit for all ensemble runs in each scatter plot. The correlation along with the 95% confidence bounds in the title of each subplot is the average correlation over all 35 runs. The confidence bounds ensemble mean correlations are calculated using the Fisher-Z transformation test for non-zero correlations.

4.4.2 EOF Analysis

Next we consider the modes of VWS variability from the perspective of an eigenanalysis of 1920-2005 CESM1-LE JAS VWS anomalies (Figs. 4.7, 4.8) and examine how each pattern contributes to the structured variance in model VWS. The eigenanalysis shows more evidence that ENSO is the dominant driver of VWS within CESM1-LE. Figure 4.7 shows both the ensemble mean spectrum of variance and distribution of the individual spectra for all 35 CESM1-LE runs. The first four EOFs (EOFs 1-4) account for an ensemble mean variance of 35%, 20%, 12%, and 9%, respectively. These variances are similar to those observed for ERA-Interim's VWS eigenanalysis (see Figure 2.5). However, there is considerable overlap of the variance for all EOFs

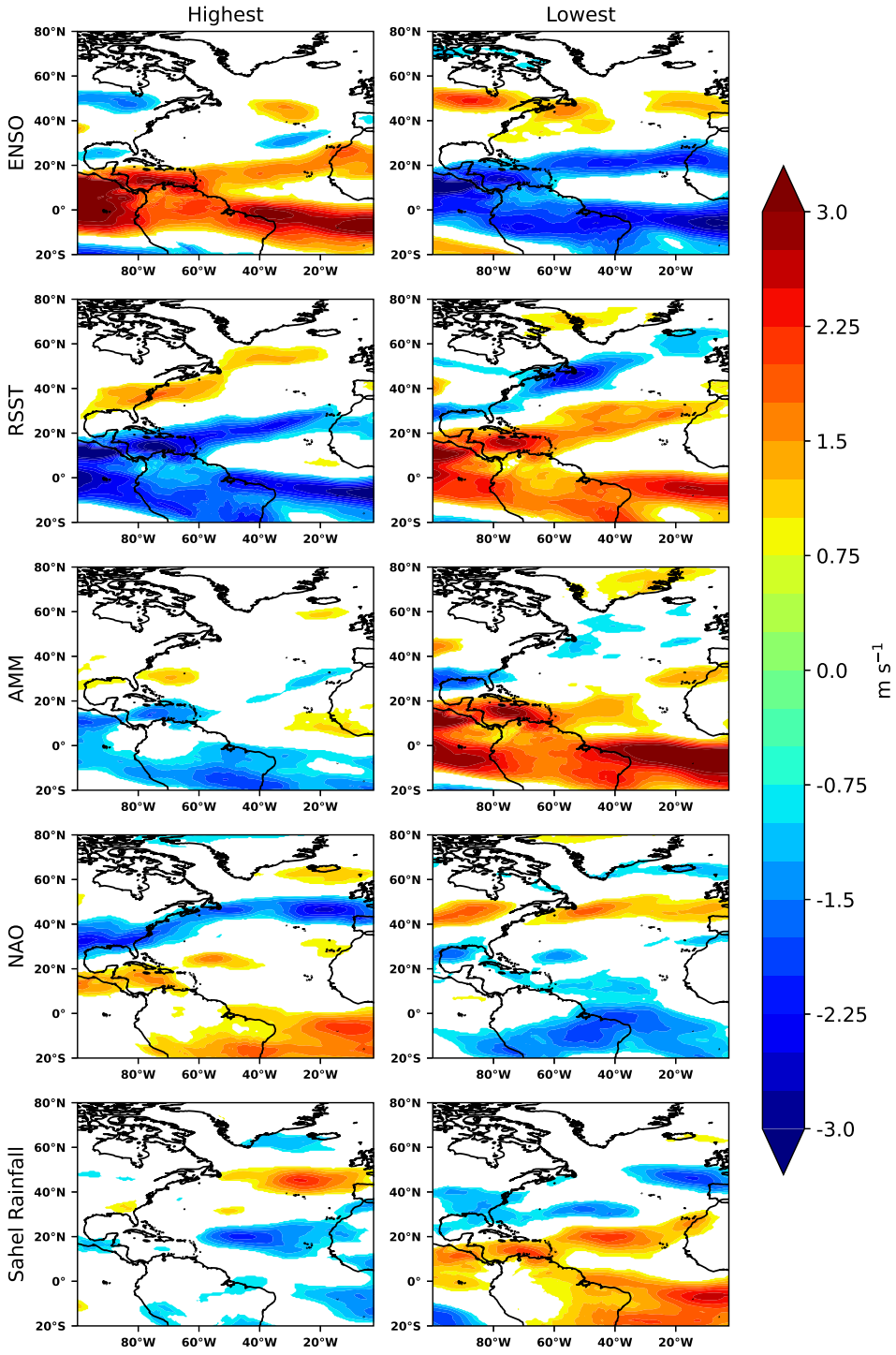

Figure 4.5: Composites of 1979-2019 VWS anomalies generated from ERA5 for the 10 highest versus 10 lowest values of the July-September ENSO, RSST, AMM, NAO, and African Sahel rainfall indices. Shaded regions indicate anomalies $\geq$0.8 m s^{-1}.

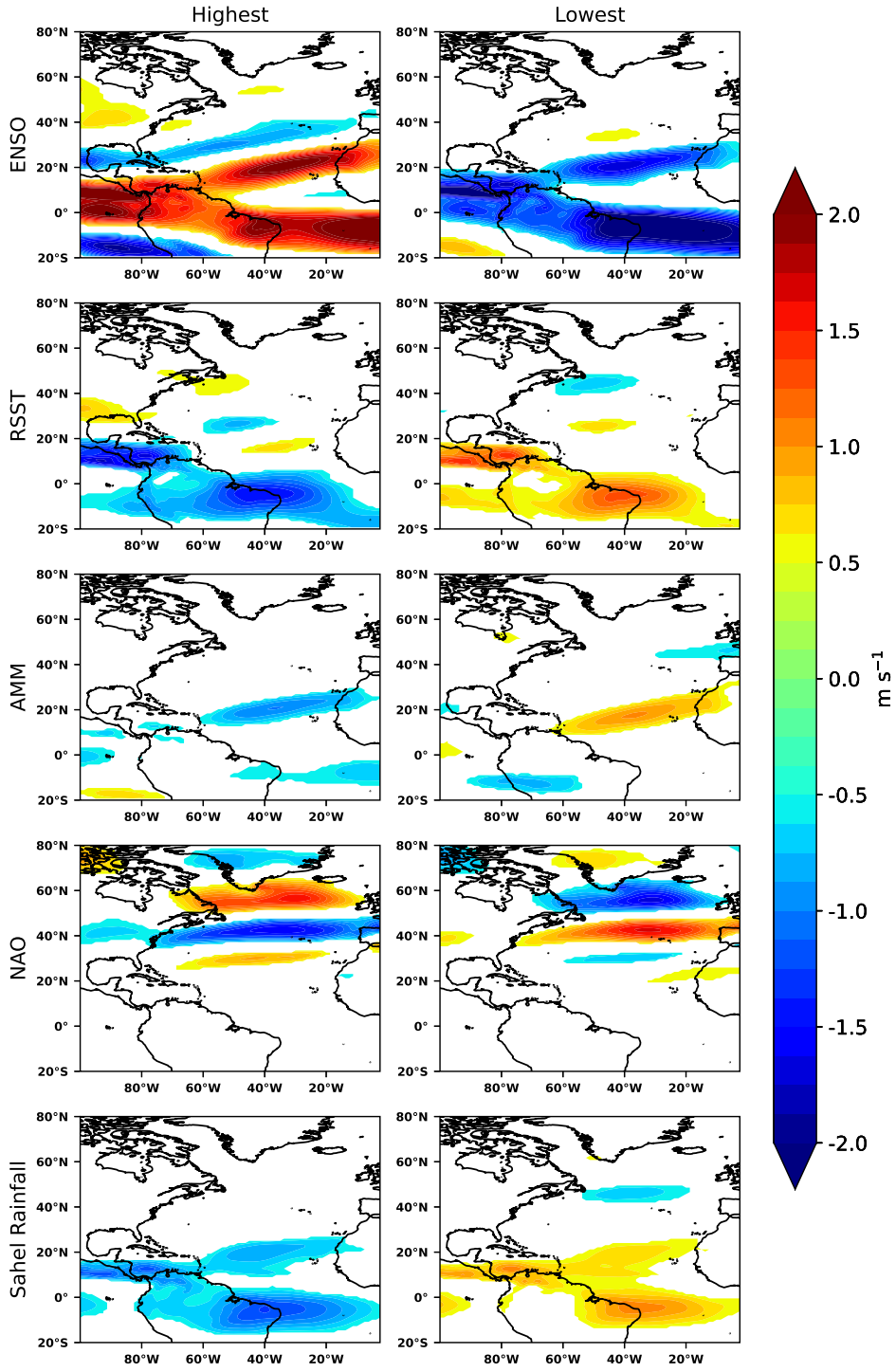

Figure 4.6: Ensemble mean composites of 1920-2005 VWS anomalies generated from CESM1-LE for the 525 highest versus 525 lowest values in the July-September ENSO, RSST, AMM, NAO, and African Sahel rainfall indices. Shaded regions indicate anomalies $\geq$0.5 m s^{-1}. Note that the scale for the current figure is different from that shown in Figure 4.5 due to the increase in sample size.

except EOF1. By North et al. (1982)'s "rule-of-thumb", EOF1 would be the dominant mode of variability. However, for consistency with Chapter 2's analysis, we retain EOFs 1-4.

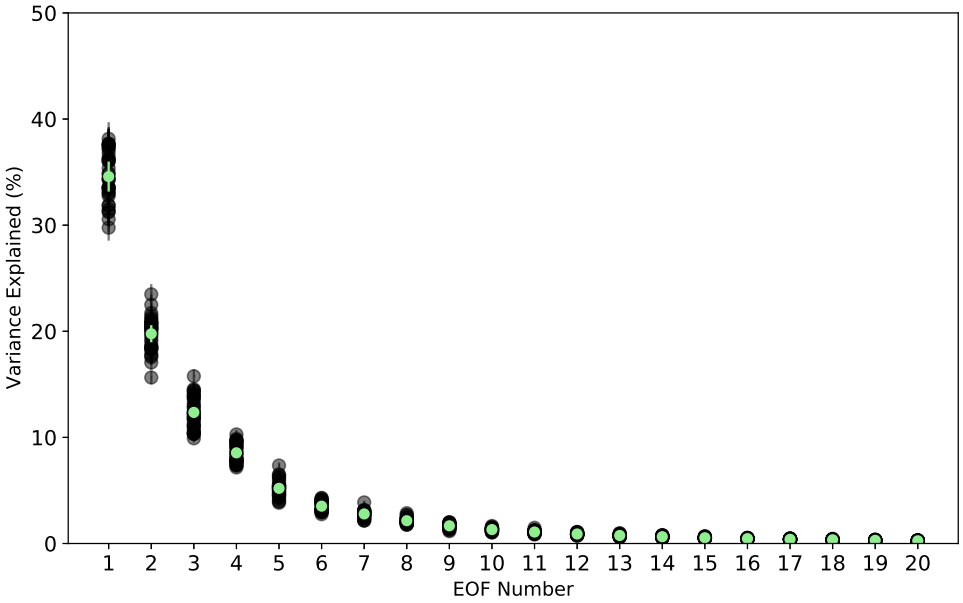

Figure 4.7: Distributions of the variance explained (in %, including error bars) by EOFs 1-20 for all 35 CESM1-LE runs. Green dots indicate the ensemble mean variance explained for each EOF.

Figure 4.8 illustrates the regression of global JAS VWS anomalies against EOFs 1-4 averaged over all ensembles at each grid point. The mean regression fields highlight the most robust EOF patterns among the ensemble runs. ENSO is a clear signal within EOF1, but is apparent in EOFs 2 and 3 as well. EOF 2 is almost a mirror of EOF 1, while EOF 3 shows a much weaker ENSO signal. EOF 4 shows a distinct pattern from EOFs 1-3 that is reminiscent of the NAO pattern shown in Figure 4.5 above. This result suggests that EOFs 1 and 2 are degenerate. Degenerate EOFs are EOF patterns that, despite the orthogonality imposed by the eigenanalysis, show similar patterns. These degenerate EOFs are likely a combination of multiple modes of variability, and there is also likely a non-trivial correlation between the EOFs (Storch 1999).

To confirm that EOFs 1 and 2 are degenerate, we calculate the ensemble mean principal components (PCs). Principal components are the leading modes of variability in the time dimension

and correspond to each EOF pattern. The ensemble mean correlation of PC1 with PCs 2 and 3 are $r_{mean} = 0.76$ and $r_{mean} = 0.43$. Additionally, ENSO has the largest correlation of the climate indices for the retained PCs. Table 4.2 shows the mean correlation between VWS, PCs 1-4 and the five climate indices. PCs 1 and 2 have a mean correlation of 0.49 and 0.45 with ENSO, respectively. While the correlations with ENSO weaken for PCs 3 and 4, ENSO's correlations are still comparable to the other 4 climate indices.

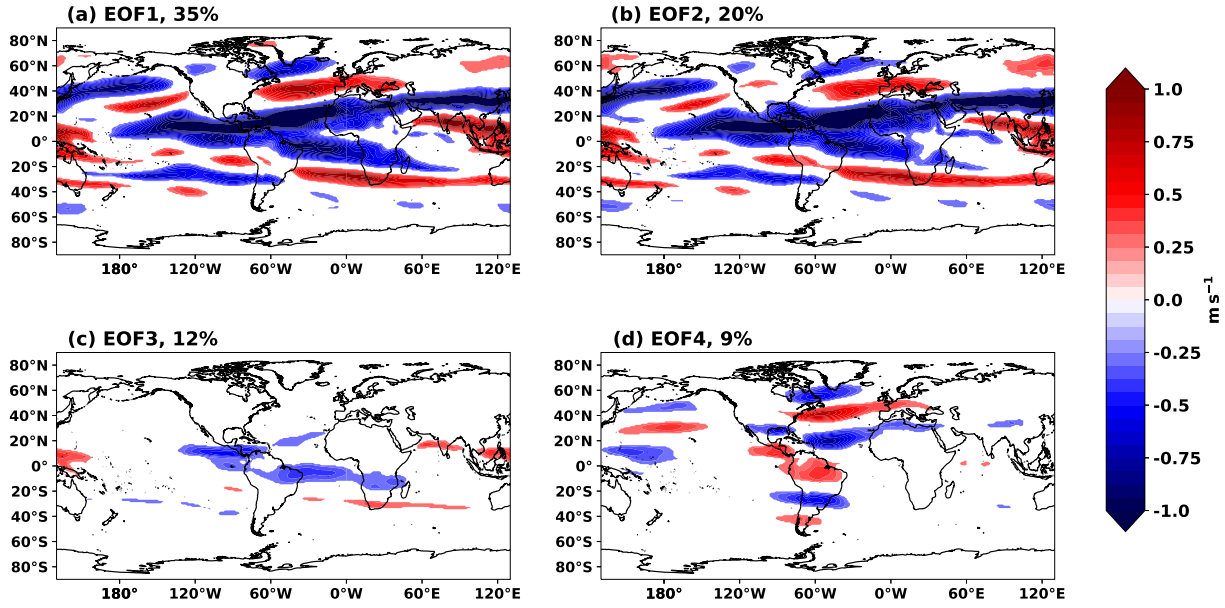

Figure 4.8: Ensemble mean regression of the first four principal components onto global zonal VWS anomalies (in m s^{-1}) from the CESM1-LE. Shaded regions indicate values $\geq$0.25 m s^{-1}. Red shaded (solid) regions indicate westerly (positive) shear anomalies, and blue shaded (dashed) regions indicate easterly (negative) shear anomalies.

Figure 4.9 shows histograms of correlations between VWS, PCs 1-4 and the climate indices ENSO, RSST, AMM, NAO, and African Sahel rainfall for all 35 runs. The figure also shows the ensemble spread around the correlation means given in Table 4.2. The white bars indicate PCs of model VWS fields without the ENSO signature removed, while red bars indicate PCs of VWS fields with the ENSO signature removed prior to the eigenanalysis. As with the correlations in Table 4.2, correlations remain non-trivial for all PCs in most ensemble runs. The correlation with ENSO shifts closer to zero with PCs 3 and 4, but remain >0.4 for some ensemble runs. While correlations with the NAO are weak in general, PC4 shows stronger associations with the NAO than PCs 1-3.

Since the degenerate EOFs tend to be associated with ENSO, we examine how the distribution of PC correlations with the RSST, AMM, NAO, and Sahel rainfall indices change when the ENSO signature is removed via the least squares linear fit prior to the EOF analysis. The results are represented by the red histograms in Figure 4.9. The ENSO-removed histograms only slightly shift the correlation distribution. Some distributions show more robust correlations. For example, the AMM-VWS and AMM-PC4 correlation distributions show noticeable improvement. But overall, there is little change relative to the original correlation distributions (in white) and the correlation between PCs 1 and 2 remain high ($r_{mean} = 0.81$). Similarly, reconstructing the VWS data without PCs 1 and 2 (not shown) does not remove the degeneracy. Furthermore, when considering EOFs 5 and 6 (patterns that were initially not retained in the analysis), there is a repetition of the patterns shown in EOFs 3 and 4. This may suggest that there are only two discernible modes of VWS variability in the CESM1-LE that may be associated with ENSO and NAO variability according to the eigenanalysis.

Table 4.2: Ensemble mean Pearson correlations of VWS and PCs 1-4 with ENSO, RSST, AMM, NAO, and African Sahel rainfall from 1920-2005.

	ENSO	RSST	AMM	NAO	Sahel
VWS	0.51	-0.19	-0.31	0.08	-0.31
PC1	0.49	-0.23	-0.29	0.1	-0.31
PC2	0.45	-0.20	-0.26	0.08	-0.29
PC3	0.28	-0.16	-0.17	0.1	-0.21
PC4	0.20	-0.14	-0.18	0.12	-0.13

4.5 VWS variations during ENSO-neutral conditions

In this section, we apply the modes of variability identified previously in Section 4.4 to characterize VWS variability under ENSO-neutral conditions. Here, ENSO-neutral is defined as a standardized anomaly between -0.5 to +0.5^{o}C in the JAS ENSO index. Figures 4.10 and 4.11 show similar scatter plots to Figures 4.3 and 4.4, but only for ENSO-neutral seasons. Though the sample size is smaller, Figure 4.10 shows that the RSST-VWS, AMM-VWS, and Sahel-VWS relationships maintain robust correlations, while the NAO-VWS relationship strengthens slightly. In reality, some linear relationships remain that can be accounted for by non-ENSO associated variability. On the other hand, Figure 4.11 loses any robust linear signal during ENSO-neutral conditions. Here, linearity is defined as variability having correlations greater than |0.2| with climate indices, while nonlinearity is defined as that having weaker correlations less than |0.2|.

Figures 4.12 and 4.13 show VWS composites for the 10 highest versus 10 lowest values for climate indices selected from ENSO-neutral seasons for ERA5 and CESM1-LE, respectively. Figure 4.12 shows that the RSST, AMM, NAO, and Sahel indices show more distinct VWS patterns when ENSO's strong influence is reduced. Though the sample size is small, Figures 4.10 and 4.12 indicate that non ENSO-related oscillations are the main sources of variability under ENSO-neutral conditions. However, this does not mean that ENSO has no influence on VWS during ENSO-neutral phases.

Figure 4.13 shows similar results with slight differences. ENSO's 'lowest' composite shows a more robust VWS pattern than ENSO's 'highest' composite. Also, non-linearity seems to be a key

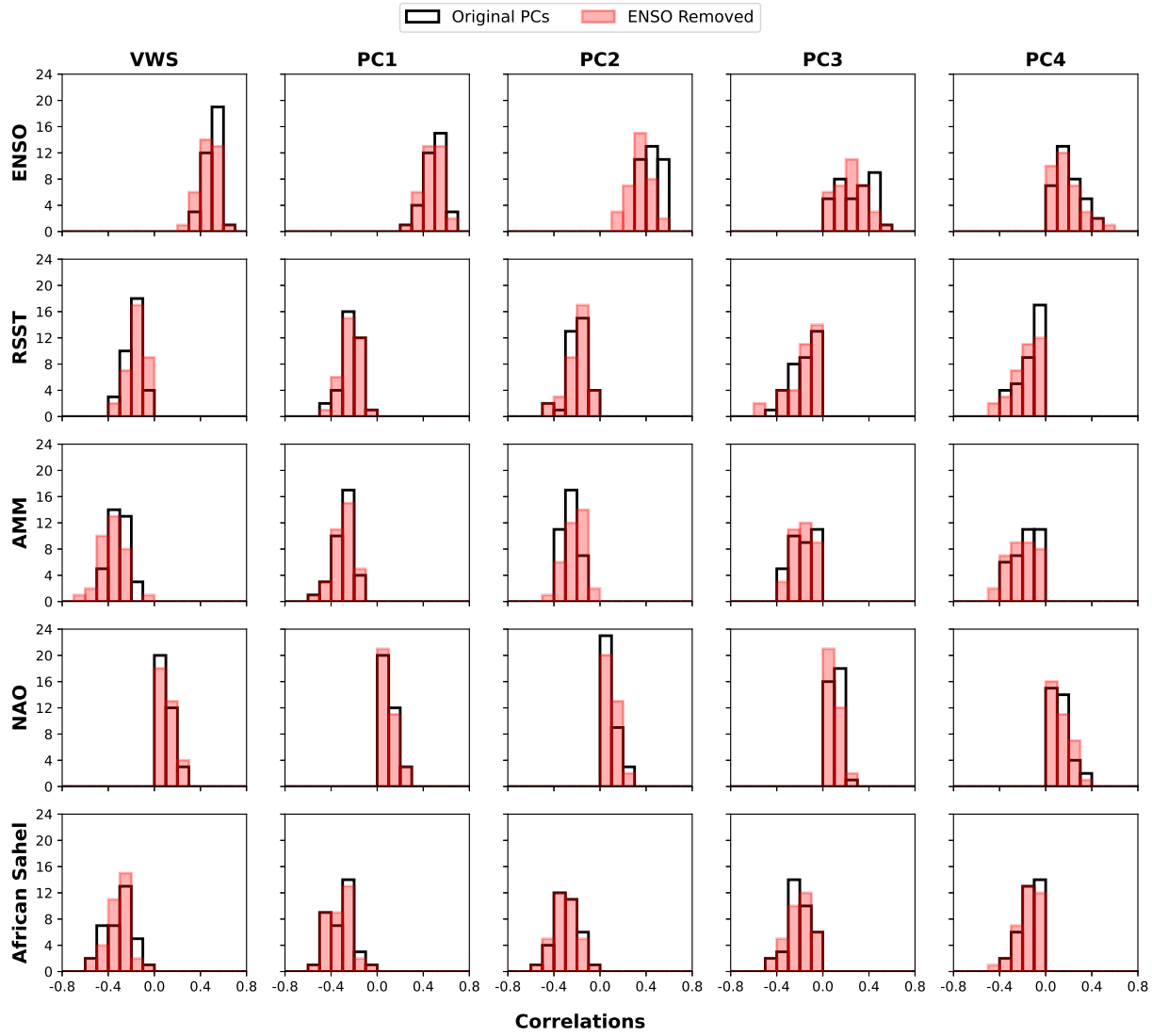

Figure 4.9: Histogram of correlations between July-September VWS and its first four principal components (PCs) with model-derived climate indices in all 35 CESM1-LE ensemble runs: El Niño Southern Oscillation (ENSO), Atlantic MDR SSTs relative to the 30^{o}S-30^{o}N tropical mean (RSST), Atlantic Meridional Mode (AMM), North Atlantic Oscillation (NAO), and African Sahel rainfall.

feature for VWS variability under ENSO-neutral conditions. There is no symmetry between the highest and lowest composites for both Figures 4.12 and 4.13. Another interesting feature of the ENSO-neutral composites is that the NAO-VWS relationship accounts for larger VWS anomalies for both ERA5 and CESM1-LE. For CESM1-LE, the NAO-VWS relationship is a strong driver for both its 'highest' and 'lowest' composites.

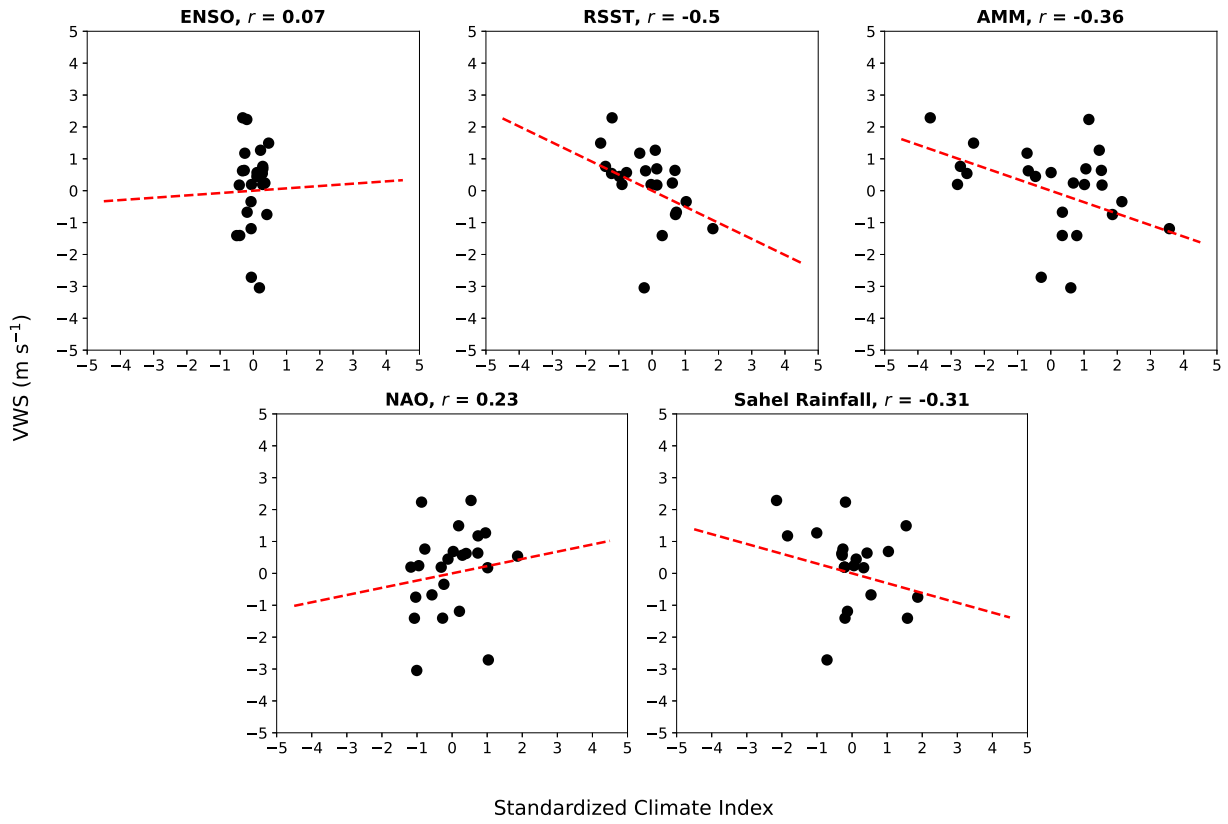

Figure 4.10: As in Figure 4.3, but for ENSO-neutral seasons. Red dashed lines indicate the least squares line of best fit for each scatter plot. ENSO-neutral seasons are defined as having a seasonal mean value $\leq \pm 0.5$ in the NOISSTv2 ENSO index.

4.6 Discussion and Conclusion

In conclusion, Chapter 4 examined the impact of large-scale drivers of seasonal tropical North Atlantic VWS variability in the CESM1-LE. We applied composite and EOF analyses to JAS VWS averaged over 10^o-30^oN and 90^o-20^oW and characterized the main drivers of VWS variability for the CESM1-LE. Additionally, we leveraged the large sample size of the CESM1-LE to examine distinct patterns of VWS variability during summer ENSO-neutral seasons. The key findings of Chapter 4 are as follows:

1. The CESM1-LE shows patterns of summer tropical Atlantic VWS variability that are physically consistent with those observed in the ERA5 reanalysis. With a larger sample size,

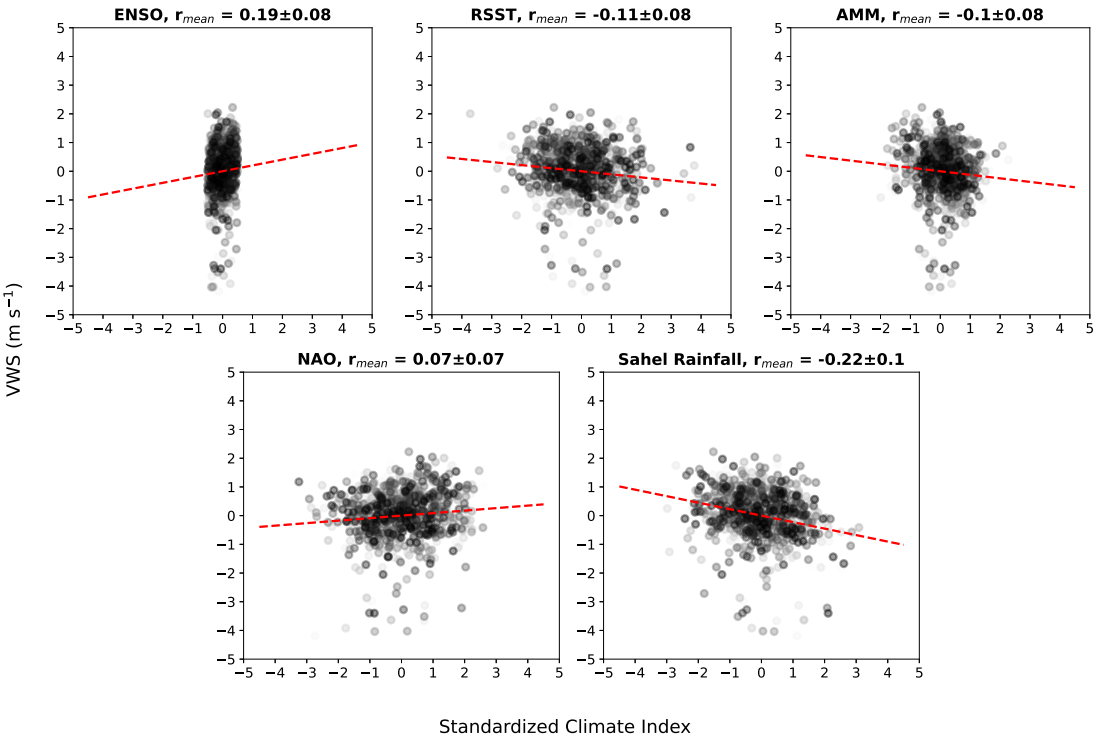

Figure 4.11: As in Figure 4.4, but for ENSO-neutral seasons for each of the 35 runs in the CESM1-LE. Red dashed lines indicate the least squares line of best fit for all ensemble runs in each scatter plot. ENSO-neutral seasons are defined as having a seasonal mean value $\leq |0.5|$ in each model's standardized ENSO index. The 95% confidence bounds are given along with mean correlation and are calculated using the Fisher-Z transformation test for non-zero correlations.

patterns associated with ENSO, MDR SSTs relative to the tropical mean (RSST), AMM, NAO, and African Sahel rainfall can be observed.

2. ENSO accounts for the first leading mode of tropical VWS; the mean variance explained by the 35 ensemble runs was 35%. The principal components of tropical Atlantic VWS are degenerate and suggest that the modes of variability are difficult to separate.

3. The CESM1-LE can be used to examine which patterns of variability drive VWS during ENSO-neutral seasons. VWS composites reveal that the patterns associated with the same climate drivers have different characteristics under ENSO-neutral conditions. The VWS patterns tend to be different for the highest versus the lowest values of each climate index

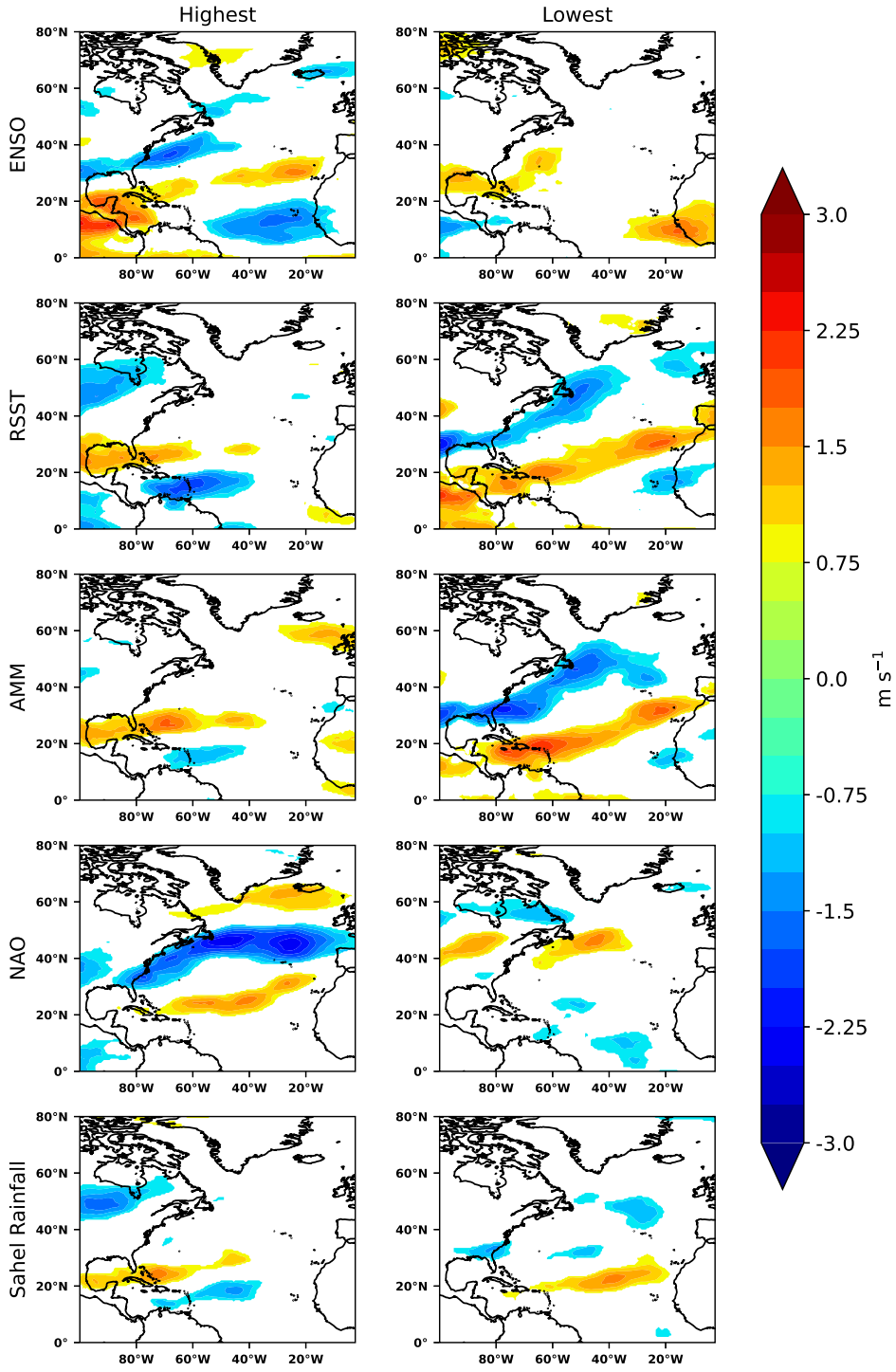

Figure 4.12: Composites of ENSO-neutral VWS anomaly for the 10 highest versus 10 lowest values in observed ENSO, RSST, AMM, NAO, and African Sahel rainfall indices. Shaded regions indicate values greater than |0.8| m s^{-1}.

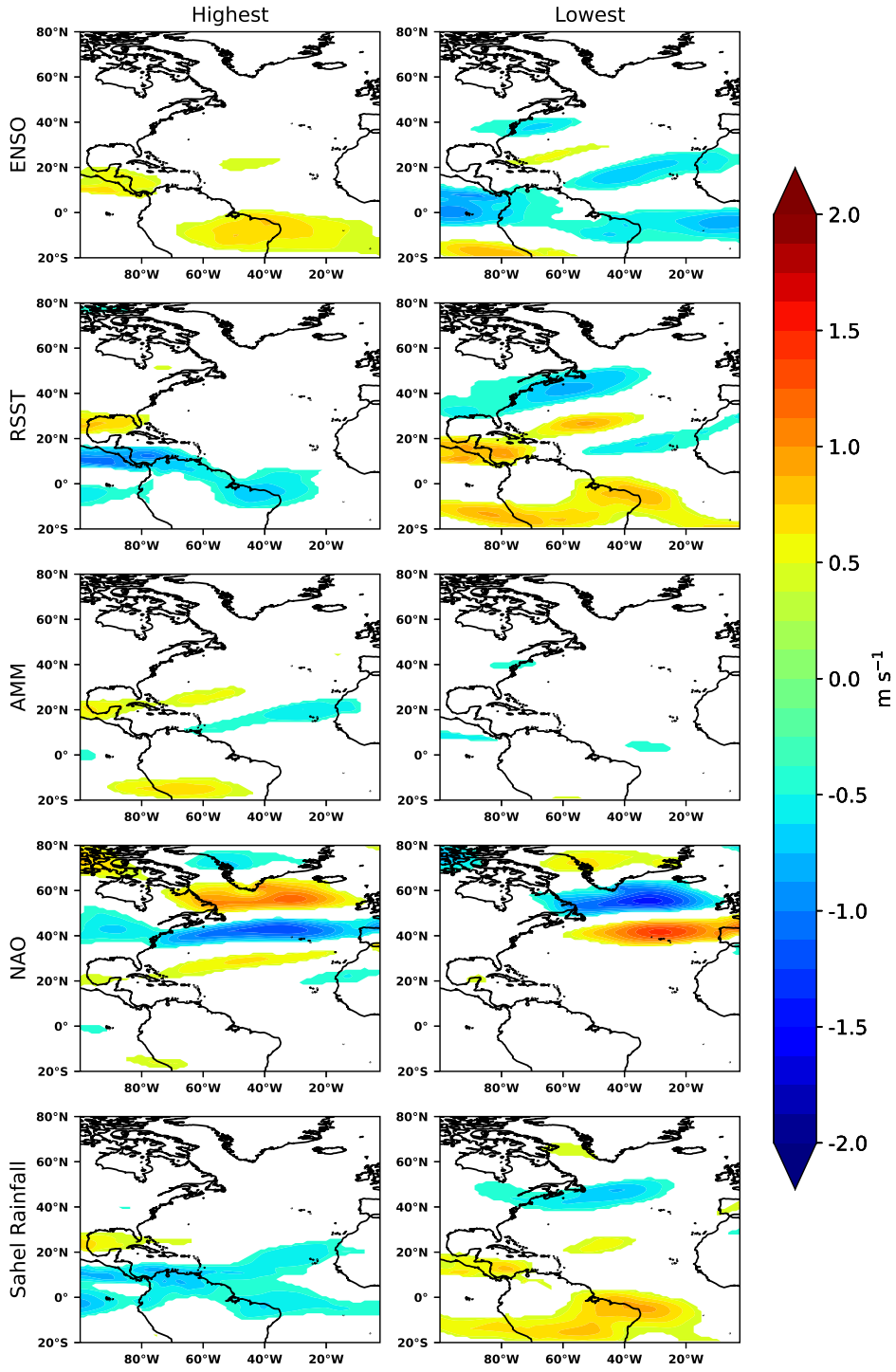

Figure 4.13: Composites of ENSO-neutral VWS anomaly for the 350 highest versus 350 lowest values in model ENSO, RSST, AMM, NAO, and African Sahel rainfall indices for each CESM1-LE run. Each composite comprises a total of 350 samples. Shaded regions indicate values greater than |0.4| m s^{-1}.

and are associated with lower correlations with VWS. This result suggests that ENSO-neutral VWS variability is less linear.

The CESM1-LE provides large samples of the large-scale circulation that are useful for examining various known climate indices in VWS. Assuming that the chosen climate indices are physically consistent with reality, we can then procure large samples of tropical Atlantic VWS for use in seasonal prediction. Collecting large samples of VWS modes of variability has key implications for seasonal TC prediction. As mentioned above, larger samples of robust VWS modes give us the tools to detect and account for sources of predictability during ENSO-neutral TC seasons. Another key implication and potential future work is in the use of machine learning techniques for seasonal prediction. Understanding the modes of VWS variability associated with extreme precipitation in GCMs and GCM large ensembles is key for successful interpretation of machine learning predictions. This results of this study provides valuable understanding of what drives tropical Atlantic deep-layer VWS. This understanding will go a long way in interpreting TC dynamics and variability predicted by GCMs.

Chapter 5

Conclusions and Future Work

To conclude, this dissertation examined the impacts of large-scale atmospheric and oceanic drivers on seasonal deep-layer vertical wind shear in reanalysis and global climate models. Chapter 2 showed that anticyclonic Rossby wave breaking (AWB) accounts for the second leading mode of July-September tropical North Atlantic VWS variability. Chapter 3 showed that an AWB-associated VWS index can add skill to an extended-range tropical cyclone statistical model with leads up to 3 months prior to the start of the Atlantic hurricane season. Chapter 4 extended the study of tropical North Atlantic VWS to the CESM1 Large Ensemble (CESM1-LE) and its variability during ENSO-neutral conditions.

In **Chapter 2**, we identified both tropical and extratropical contributions to the variability of seasonal 200-850 hPa zonal vertical wind shear in the tropical North Atlantic region using compositing and EOF analysis. The key findings of Chapter 2 are as follows:

1. The first leading mode of variability in tropical North Atlantic zonal VWS accounts for 36% of the structured variance and is driven by interannual variations in ENSO and the AMM, suggesting that tropical sources of shear are the dominant contributor to VWS.

2. AWB activity is shown to be associated with the second EOF mode and accounts for 23% of the structured variance. While not as strong as ENSO, this extratropical source of shear is a significant contributor to VWS variability and TC activity.

3. The third leading mode is associated with the pressure gradient likely modulated by the Walker Circulation, accounting for 12% of tropical VWS.

4. African Sahel rainfall is associated with the fourth mode of variability in high-frequency variations of tropical North Atlantic zonal VWS, accounting for 8% of the structured variance.

Chapter 3 showed that subtropical AWB influences seasonal North Atlantic TC activity via AWB's forcing of tropical VWS (Zhang et al. 2016, 2017; Papin et al. 2020). An index representing summer AWB-associated environmental anomalies provides one way of quantifying AWB's impact on the tropical and subtropical Atlantic MDR and yields additional skill to seasonal predictions of TC activity (Jones et al. 2020). In this study, we examined the use of the strong winter environment/summer AWB-shear link to assess the predictability of AWB impacts on seasonal TC activity and show that including the dynamical effects of AWB is useful in seasonal TC predictions. The key findings of Chapter 3 are as follows:

1. There is a strong association between winter and summer AWB shear impacts. Correlations significant at the 95% confidence level between the July-September (JAS) AWB-shear index and the January-March (JFM) 200 hPa zonal wind field show anticyclonically sheared wind anomalies that indicate wave breaking.

2. The strength of the winter-summer AWB relationship is an indication of wave breaking-induced NAO anomalies. Continuous wave breaking sustains seasonal NAO anomalies and provides a physical explanation for persistence in seasonal AWB shear impacts.

3. Potential impacts of summer wave breaking on TC activity can be estimated by projecting an index of January-March 200-hPa zonal wind anomalies onto the winter-summer AWB relationship, denoted here as $U200_{proj}$.

4. The $U200_{proj}$ index is significantly correlated at -0.35 with ACE and 0.45 with summer AWB-shear indices. The revised early April statistical seasonal hurricane forecast model from CSU including an index closely related to $U200_{proj}$ improves upon CSU's 2019 early April extended-range statistical forecast from 1982-2020.

Chapter 4 examined model representations of known climate phenomena and their physical impact on VWS variability within the CESM1-LE. Using similar analyses as that of Chapter 2, ENSO is shown to be responsible for most of the variability within the large ensemble. Also, with the large sample size of CESM1-LE, VWS variability during ENSO-neutral conditions are examined. The key findings in Chapter 4 were as follows:

1. The CESM1-LE shows patterns of summer tropical Atlantic VWS variability that are physically consistent with those observed in the ERA5 reanalysis. With a larger sample size, patterns associated with ENSO, MDR SSTs relative to the tropical mean (RSST), AMM, NAO, and African Sahel rainfall can be observed.

2. ENSO accounts for the first leading mode of tropical VWS; mean variance explained by the 35 ensemble runs was 35%. The principal components of tropical Atlantic VWS are degenerate and suggest that the modes of variability are difficult to separate.

3. The CESM1-LE can be used to examine which patterns of variability drive VWS during ENSO-neutral seasons. VWS composites reveal that the patterns associated with the same climate drivers have different characteristics under ENSO-neutral conditions. The VWS patterns tend to be different for the highest versus the lowest values of each climate index and are associated with lower correlations with VWS. This result suggests that ENSO-neutral VWS variability is less linear.

Overall, the analyses and results presented in this dissertation improves our understanding of the large-scale tropical VWS variability by characterizing patterns of just a handful of large-scale drivers in tropical Atlantic VWS and demonstrates a few ways in which this insight into VWS can be used to address key challenges in seasonal TC prediction. The results suggest that subtropical contributions to VWS explain some variance not yet accounted for in current statistical TC forecast schemes. We also gain a better picture of how these large-scale drivers influence the North Atlantic atmospheric circulation during ENSO-neutral conditions. Capturing non-linear

variability is key for prediction of the large-scale environment, and consequently TC activity, in ENSO-neutral seasons.

These findings raise some exciting prospects for future work. One application of this research is to characterize and identify VWS patterns associated with several other large-scale drivers not addressed in this dissertation, for example the Madden Julian Oscillation (MJO; Hansen et al. 2020), a key source of large-scale subseasonal-to-seasonal climate predictability, and the Indian Ocean Dipole (IOD; Wood et al. 2020). As we have done for AWB activity in Chapters 2 and 3 above, we can further characterize the impacts these large-scale oscillations may have on both subseasonal and seasonal TC variability and possibilities for predictions.

Another implication is in the application of machine learning techniques for prediction. With the aid of a large sample size as that provided by the CESM1-LE, larger samples of each mode of VWS variability can be achieved. Such a large sample of patterns is useful for the interpretation of machine learning results and for examining non-linear sources of predictability, especially in ENSO-neutral summer seasons.

References

Abatzoglou, J. T., and G. Magnusdottir, 2006a: Opposing effects of reflective and nonreflective planetary wave breaking on the NAO. *J. Atmos. Sci.*, **63 (12)**, 3448–3457, https://doi.org/10.1175/JAS3809.1.

Abatzoglou, J. T., and G. Magnusdottir, 2006b: Planetary wave breaking and nonlinear reflection: Seasonal cycle and interannual variability. *J. Climate*, **19 (23)**, 6139–6152, https://doi.org/10.1175/JCLI3968.1.

Aiyyer, A., and C. Thorncroft, 2011: Interannual-to-multidecadal variability of vertical shear and tropical cyclone activity. *J. Climate*, **24 (12)**, 2949–2962, https://doi.org/10.1175/2010JCLI3698.1.

Aiyyer, A. R., and C. Thorncroft, 2006: Climatology of vertical wind shear over the tropical atlantic. *J. Climate*, **19 (12)**, 2969–2983, https://doi.org/10.1175/JCLI3685.1.

Arkin, P. A., 1982: The relationship between interannual variability in the 200 mb tropical wind field and the Southern Oscillation. *Mon. Wea. Rev.*, **110 (10)**, 1393–1404, https://doi.org/10.1175/1520-0493(1982)110<1393:TRBIVI>2.0.CO;2.

Ashok, K., S. K. Behera, S. A. Rao, H. Weng, and T. Yamagata, 2007: El Niño Modoki and its possible teleconnection. *J. Geophys. Res.*, **112 (C11)**, https://doi.org/10.1029/2006JC003798.

Bach, E., S. Motesharrei, E. Kalnay, and A. Ruiz-Barradas, 2019: Local atmosphere–ocean predictability: Dynamical origins, lead times, and seasonality. *J. Climate*, **32 (21)**, 7507–7519, https://doi.org/10.1175/JCLI-D-18-0817.1.

Baldwin, M. P., D. B. Stephenson, and I. T. Jolliffe, 2009: Spatial weighting and iterative projection methods for EOFs. *J. Climate*, **22 (2)**, 234–243, https://doi.org/10.1175/2008JCLI2147.1.

Barnes, E. A., and D. L. Hartmann, 2012: Detection of Rossby wave breaking and its response to shifts of the midlatitude jet with climate change. *J. Geophys. Res.*, **117 (D9117)**, https://doi.org/10.1029/2012JD017469.

Barnston, A. G., and R. E. Livezey, 1987: Classification, seasonality and persistence of low-frequency atmospheric circulation patterns. *Mon. Wea. Rev.*, **115 (6)**, 1083–1126, https://doi.org/10.1175/1520-0493(1987)115<1083:CSAPOL>2.0.CO;2.

Bell, G. D., and Coauthors, 2000: Climate assessment for 1999. *Bull. Amer. Meteor. Soc.*, **81 (6)**, S1–S50, https://doi.org/10.1175/1520-0477(2000)81[s1:CAF]2.0.CO;2.

Benedict, J. J., S. Lee, and S. B. Feldstein, 2004: Synoptic view of the North Atlantic Oscillation. *J. Atmos. Sci.*, **61 (2)**, 121–144, https://doi.org/10.1175/1520-0469(2004)061<0121:SVOTNA>2.0.CO;2.

Berrisford, P., P. Kållberg, S. Kobayashi, D. Dee, S. Uppala, A. Simmons, P. Poli, and H. Sato, 2011: Atmospheric conservation properties in ERA-Interim. *Quart. J. Roy. Meteor. Soc.*, **137 (659)**, 1381–1399, https://doi.org/10.1002/qj.864.

Bowley, K. A., J. R. Gyakum, and E. H. Atallah, 2019: A new perspective toward cataloging Northern Hemisphere Rossby wave breaking on the dynamic tropopause. *Mon. Wea. Rev.*, **147 (2)**, 409–431, https://doi.org/10.1175/MWR-D-18-0131.1.

Camargo, S. J., K. A. Emanuel, and A. H. Sobel, 2007: Use of a genesis potential index to diagnose ENSO effects on tropical cyclone genesis. *J. Climate*, **20 (19)**, 4819–4834, https://doi.org/10.1175/JCLI4282.1.

Camargo, S. J., and A. H. Sobel, 2010: Revisiting the influence of the Quasi-Biennial Oscillation on tropical cyclone activity. *J. Climate*, **23 (21)**, 5810–5825, https://doi.org/10.1175/2010JCLI3575.1.

Camargo, S. J., M. K. Tippett, A. H. Sobel, G. A. Vecchi, and M. Zhao, 2014: Testing the performance of tropical cyclone genesis indices in future climates using the HiRAM model. *J. Climate*, **27 (24)**, 9171–9196, https://doi.org/10.1175/JCLI-D-13-00505.1.

Camargo, S. J., and A. A. Wing, 2016: Tropical cyclones in climate models. *WIREs Climate Change*, **7 (2)**, 211–237, https://doi.org/10.1002/wcc.373.

Camp, J., M. Roberts, C. MacLachlan, E. Wallace, L. Hermanson, A. Brookshaw, A. Arribas, and A. A. Scaife, 2015: Seasonal forecasting of tropical storms using the Met Office GloSea5 seasonal forecast system. *Quart. J. Roy. Meteor. Soc.*, **141 (691)**, 2206–2219, https://doi.org/10.1002/qj.2516.

Chand, S. S., K. J. Tory, J. L. McBride, M. C. Wheeler, R. A. Dare, and K. J. Walsh, 2013: The different impact of positive-neutral and negative-neutral ENSO regimes on Australian tropical cyclones. *J. Climate*, **26 (20)**, 8008–8016, https://doi.org/10.1175/JCLI-D-12-00769.1.

Chelliah, M., and G. D. Bell, 2004: Tropical multidecadal and interannual climate variability in the NCEP–NCAR reanalysis. *J. Climate*, **17 (9)**, 1777–1803, https://doi.org/10.1175/1520-0442(2004)017<1777:TMAICV>2.0.CO;2.

Chiang, J., and D. Vimont, 2004: Analogous Pacific and Atlantic meridional modes of tropical atmosphere-ocean variability. *J. Climate*, **17 (21)**, 4143–4158, https://doi.org/10.1175/JCLI4953.1.

Corbosiero, K. L., and J. Molinari, 2002: The effects of vertical wind shear on the distribution of convection in tropical cyclones. *Mon. Wea. Rev.*, **130 (8)**, 2110–2123, https://doi.org/10.1175/1520-0493(2002)130<2110:TEOVWS>2.0.CO;2.

Corbosiero, K. L., and J. Molinari, 2003: The relationship between storm motion, vertical wind shear, and convective asymmetries in tropical cyclones. *J. Atmos. Sci.*, **60 (2)**, 366–376, https://doi.org/10.1175/1520-0469(2003)060<0366:TRBSMV>2.0.CO;2.

CPC, 2020: Background Information: North Atlantic hurricane season. NOAA Center for Weather and Climate Prediction, accessed 24 February 2021, https://www.cpc.ncep.noaa.gov/products/outlooks/Background.html.

Czaja, A., A. W. Robertson, and T. Huck, 2003: *The role of Atlantic ocean-atmosphere coupling in affecting North Atlantic Oscillation variability*, 147–172. American Geophysical Union (AGU), https://doi.org/10.1029/134GM07.

Dee, D. P., and Coauthors, 2011: The ERA-Interim reanalysis: configuration and performance of the data assimilation system. *Quart. J. Roy. Meteor. Soc.*, **137 (656)**, 553–597, https://doi.org/10.1002/qj.828.

DeHart, J. C., R. A. Houze, and R. F. Rogers, 2014: Quadrant distribution of tropical cyclone inner-core kinematics in relation to environmental shear. *J. Atmos. Sci.*, **71 (7)**, 2713–2732, https://doi.org/10.1175/JAS-D-13-0298.1.

Dommenget, D., T. Bayr, and C. Frauen, 2013: Analysis of the non-linearity in the pattern and time evolution of El Niño Southern Oscillation. *Climate Dyn.*, **40 (11-12)**, 2825–2847, https://doi.org/10.1007/s00382-012-1475-0.

Drouard, M., G. Rivière, and P. Arbogast, 2013: The North Atlantic Oscillation response to large-scale atmospheric anomalies in the northeastern Pacific. *J. Atmos. Sci.*, **70 (9)**, 2854–2874, https://doi.org/10.1175/JAS-D-12-0351.1.

Drouard, M., G. Rivière, and P. Arbogast, 2015: The link between the North Pacific climate variability and the North Atlantic Oscillation via downstream propagation of synoptic waves. *J. Climate*, **28 (10)**, 3957–3976, https://doi.org/10.1175/JCLI-D-14-00552.1.

Dunion, J. P., 2011: Rewriting the climatology of the tropical North Atlantic and Caribbean Sea atmosphere. *J. Climate*, **24 (3)**, 893–908, https://doi.org/10.1175/2010JCLI3496.1.

Elsner, J. B., T. Jagger, and X.-F. Niu, 2000: Changes in the rates of north atlantic major hurricane activity during the 20th century. *Geophys. Res. Lett.*, **27 (12)**, 1743–1746, https://doi.org/10.1029/2000GL01145.

Franzke, C., S. Lee, and S. B. Feldstein, 2004: Is the North Atlantic Oscillation a breaking wave? *J. Atmos. Sci.*, **61 (2)**, 145–160, https://doi.org/10.1175/1520-0469(2004)061<0145:ITNAOA>2.0.CO;2.

Galarneau, T. J., R. McTaggart-Cowan, L. F. Bosart, and C. A. Davis, 2015: Development of North Atlantic tropical disturbances near upper-level potential vorticity streamers. *J. Atmos. Sci.*, **72 (2)**, 572–597, https://doi.org/10.1175/JAS-D-14-0106.1.

Gao, K., J.-H. Chen, L. Harris, Y. Sun, and S.-J. Lin, 2019: Skillful prediction of monthly major hurricane activity in the north atlantic with two-way nesting. *Geophys. Res. Lett.*, **46 (15)**, 9222–9230, https://doi.org/10.1029/2019GL083526.

Goldenberg, S. B., C. W. Landsea, A. M. Mestas-Nuñez, and W. M. Gray, 2001: The recent increase in atlantic hurricane activity: Causes and implications. *Science*, **293 (5529)**, 474–479, https://doi.org/10.1126/science.293.5537.1997.

Goldenberg, S. B., and L. J. Shapiro, 1996: Physical mechanisms for the association of El Niño and west African rainfall with Atlantic major hurricane activity. *J. Climate*, **9 (6)**, 1169–1187, https://doi.org/10.1175/1520-0442(1996)009<1169:PMFTAO>2.0.CO;2.

Gray, W. M., 1968: GLOBAL VIEW OF THE ORIGIN OF TROPICAL DISTURBANCES AND STORMS. *Mon. Wea. Rev.*, **96 (10)**, 669–700, https://doi.org/10.1175/1520-0493(1968)096<0669:GVOTOO>2.0.CO;2.

Gray, W. M., 1984: Atlantic Seasonal Hurricane Frequency. Part I: El Niño and 30 mb Quasi-Biennial Oscillation Influences. *Mon. Wea. Rev.*, **112 (9)**, 1649–1668, https://doi.org/10.1175/1520-0493(1984)112<1649:ASHFPI>2.0.CO;2.

Gray, W. M., C. W. Landsea, P. W. Mielke Jr, and K. J. Berry, 1994: Predicting Atlantic basin seasonal tropical cyclone activity by 1 June. *Wea. Forecasting*, **9 (1)**, 103–115.

Grossmann, I., and P. J. Klotzbach, 2009: A review of North Atlantic modes of natural variability and their driving mechanisms. *J. Geophys. Res. Atmos.*, **114 (D24)**.

Ha, Y., Z. Zhong, X. Yang, and Y. Sun, 2013: Different Pacific Ocean warming decaying types and Northwest Pacific tropical cyclone activity. *J. Climate*, **26 (22)**, 8979–8994, https://doi.org/10.1175/JCLI-D-13-00097.1.

Hansen, K. A., S. J. Majumdar, and B. P. Kirtman, 2020: Identifying Subseasonal Variability Relevant to Atlantic Tropical Cyclone Activity. *Wea. Forecasting*, **35 (5)**, 2001–2024, https://doi.org/10.1175/WAF-D-19-0260.1.

Hersbach, H., and Coauthors, 2020: The ERA5 global reanalysis. *Quart. J. Roy. Meteor. Soc.*, **146 (730)**, 1999–2049, https://doi.org/10.1002/qj.3803.

Homeyer, C. R., and K. P. Bowman, 2013: Rossby Wave Breaking and Transport between the Tropics and Extratropics above the Subtropical Jet. *J. Atmos. Sci.*, **70 (2)**, 607–626, https://doi.org/10.1175/JAS-D-12-0198.1.

Horii, T., and K. Hanawa, 2004: A relationship between timing of El Niño onset and subsequent evolution. *Geophys. Res. Lett.*, **31 (6)**, https://doi.org/10.1029/2003GL019239.

Hurrell, J. W., and Coauthors, 2013: The Community Earth System Model: A framework for collaborative research. *Bull. Amer. Meteor. Soc.*, **94 (9)**, 1339–1360.

Janicot, S., A. Harzallah, B. Fontaine, and V. Moron, 1998: West African monsoon dynamics and eastern equatorial Atlantic and Pacific SST anomalies (1970–88). *J. Climate*, **11 (8)**, 1874–1882, https://doi.org/10.1175/1520-0442(1998)011<1874:WAMDAE>2.0.CO;2.

Janicot, S., S. Trzaska, and I. Poccard, 2001: Summer Sahel-ENSO teleconnection and decadal time scale SST variations. *Climate Dyn.*, **18 (3-4)**, 303–320, https://doi.org/10.1007/s003820100172.

Johnson, N. C., and S.-P. Xie, 2010: Changes in the sea surface temperature threshold for tropical convection. *Nat. Geosci.*, **3 (12)**, 842–845, https://doi.org/10.1038/NGEO1008.

Jones, J., M. Bell, P. Klotzbach, and E. Barnes, 2021: Wintertime Rossby Wave Breaking Persistence in Extended-range seasonal Forecasts of Atlantic Tropical Cyclone Activity. *J. Climate*, *In Review*.

Jones, J. J., M. M. Bell, and P. J. Klotzbach, 2020: Tropical and subtropical North Atlantic vertical wind shear and seasonal tropical cyclone activity. *J. Climate*, **33 (13)**, 5413–5426, https://doi.org/10.1175/JCLI-D-19-0474.1.

Jones, S. C., 1995: The evolution of vortices in vertical shear. I: Initially barotropic vortices. *Quart. J. Roy. Meteor. Soc.*, **121 (524)**, 821–851, https://doi.org/10.1002/qj.49712152406.

Karnauskas, K. B., and L. Li, 2016: Predicting Atlantic seasonal hurricane activity using outgoing longwave radiation over Africa. *Geophys. Res. Lett.*, **43 (13)**, 7152–7159, https://doi.org/10.1002/2016GL069792.

Kay, J. E., and Coauthors, 2015: The Community Earth System Model (CESM) Large Ensemble Project: A community resource for studying climate change in the presence of internal climate variability. *Bull. Amer. Meteor. Soc.*, **96 (8)**, 1333 – 1349, //https:/doi.org/10.1175/BAMS-D-13-00255.1.

Klotzbach, P., M. Bell, and J. Jones, 2019: Extended range forecast of Atlantic seasonal hurricane activity and landfall strike probability for 2019. Accessed 30 August 2020, https://tropical.colostate.edu/Forecast/Archived_Forecasts/2010s/2019-04.pdf.

Klotzbach, P., M. Bell, and J. Jones, 2020a: Extended range forecast of Atlantic seasonal hurricane activity and landfall strike probability for 2020. Colorado State University, accessed 30 April 2020, https://tropical.colostate.edu/Forecast/2020-04.pdf.

Klotzbach, P., and W. Gray, 2013: Summary of 2013 Atlantic tropical cyclone activity and verification of Authors' seasonal and two-week forecasts. Accessed 30 July 2020, https://tropical.colostate.edu/Forecast/Archived_Forecasts/2010s/2013-11.pdf.

Klotzbach, P., W. Gray, and W. Thorson, 2007: Summary of 2007 Atlantic tropical cyclone activity and verification of Authors' seasonal and two-week forecasts. Accessed 30 July 2020, https://tropical.colostate.edu/media/sites/111/2016/07/2007-11.pdf.

Klotzbach, P. J., L.-P. Caron, and M. M. Bell, 2020b: A statistical/dynamical model for North Atlantic seasonal hurricane prediction. *Geophys. Res. Lett.*, **47 (20)**, https://doi.org/10.1029/2020GL089357.

Klotzbach, P. J., and W. M. Gray, 2004: Updated 6-11-Month Prediction of Atlantic Basin Seasonal Hurricane Activity. *Wea. Forecasting*, **19 (5)**, 917–934, https://doi.org/10.1175/1520-0434(2004)019<0917:UMPOAB>2.0.CO;2.

Klotzbach, P. J., and W. M. Gray, 2008: Multidecadal variability in North Atlantic tropical cyclone activity. *J. Climate*, **21 (15)**, 3929–3935, https://doi.org/10.1175/2008JCLI2162.1.

Klotzbach, P. J., M. A. Saunders, G. D. Bell, and E. S. Blake, 2017: North atlantic seasonal hurricane prediction: Underlying science and an evaluation of statistical models. *Climate Extremes: Patterns and Mechanisms, Geophys. Monogr*, **226**, 315–328.

Kossin, J. P., and D. J. Vimont, 2007: A more general framework for understanding Atlantic hurricane variability and trends. *Bull. Amer. Meteor. Soc.*, **88 (11)**, 1767–1782, https://doi.org/10.1175/BAMS-88-11-1767.

Krishnamurthy, L., G. A. Vecchi, R. Msadek, H. Murakami, A. Wittenberg, and F. Zeng, 2016: Impact of strong enso on regional tropical cyclone activity in a high-resolution climate model in

the north pacific and north atlantic oceans. *J. Climate*, **29 (7)**, 2375 – 2394, //https:/doi.org/10.1175/JCLI-D-15-0468.1.

Kunz, A., M. Sprenger, and H. Wernli, 2015: Climatology of potential vorticity streamers and associated isentropic transport pathways across PV gradient barriers. *J. Geophys. Res.*, **120 (9)**, 3802–3821, https://doi.org/10.1002/2014JD022615.

Landsea, C. W., and J. L. Franklin, 2013: Atlantic hurricane database uncertainty and presentation of a new database format. *Mon. Wea. Rev.*, **141 (10)**, 3576–3592, https://doi.org/10.1175/MWR-D-12-00254.1.

Landsea, C. W., and W. M. Gray, 1992: The strong association between western Sahelian monsoon rainfall and intense Atlantic hurricanes. *J. Climate*, **5 (5)**, 435–453, https://doi.org/10.1175/1520-0442(1992)005<0435:TSABWS>2.0.CO;2.

Larkin, N. K., D. E. Harrison, N. K. Larkin, and D. E. Harrison, 2002: ENSO Warm (El Niño) and Cold (La Niña) Event Life Cycles: Ocean Surface Anomaly Patterns, Their Symmetries, Asymmetries, and Implications. *J. Climate*, **15 (10)**, 1118–1140, https://doi.org/10.1175/1520-0442(2002)015$\lesssim$1118:EWENOA$\gtrsim$2.0.CO;2.

Lau, N.-C., and M. J. Nath, 1996: The role of the "atmospheric bridge" in linking tropical pacific enso events to extratropical sst anomalies. *J. Climate*, **9 (9)**, 2036–2057, https://doi.org/10.1175/1520-0442(1996)009<2036:TROTBI>2.0.CO;2.

Lee, I., and K. Preacher, 2013: Calculation for the test of the difference between two dependent correlations with one variable in common [computer software]. Available from http://quantpsy.org/.

Li, W., Z. Wang, G. Zhang, M. S. Peng, S. G. Benjamin, and M. Zhao, 2018: Subseasonal variability of Rossby wave breaking and impacts on tropical cyclones during the North Atlantic warm season. *J. Climate*, **31**, https://doi.org/10.1175/JCLI-D-17-0880.1.

Madden, R. A., and P. R. Julian, 1972: Description of global-scale circulation cells in the tropics with a 40-50 day period. *J. Atmos. Sci.*, **29 (6)**, 1109 – 1123, https://doi.org/10.1175/1520-0469(1972)029<1109:DOGSCC>2.0.CO;2.

Mariotti, A., and Coauthors, 2020: Windows of opportunity for skillful forecasts subseasonal to seasonal and beyond. *Bull. Amer. Meteor. Soc.*, **101 (5)**, E608–E625, https://doi.org/10.1175/BAMS-D-18-0326.1.

Martius, O., C. Schwierz, and M. Sprenger, 2008: Dynamical tropopause variability and potential vorticity streamers in the northern hemisphere—a climatological analysis. *Adv. Atmos. Sci.*, **25 (3)**, 367–380.

Matthews, A. J., and G. N. Kiladis, 1999: Interactions between ENSO, transient circulation, and tropical convection over the Pacific. *J. Climate*, **12 (10)**, 3062–3086.

McIntyre, M. E., and T. Palmer, 1983: Breaking planetary waves in the stratosphere. *Nature*, **305 (5935)**, 593, https://doi.org/10.1038/305593a0.

Mitchell, T., 2013: Sahel Precipitation Index. Joint Institute for the Study of the Atmosphere and Ocean, University of Washington, https://doi.org/10.6069/H5MW2F2Q.

Nolan, D. S., and M. G. McGauley, 2012: Tropical cyclogenesis in wind shear: Climatological relationships and physical processes. Nova Science Publishers Happauge, New York, 1–36 pp.

North, G. R., T. L. Bell, R. F. Cahalan, and F. J. Moeng, 1982: Sampling errors in the estimation of empirical orthogonal functions. *Mon. Wea. Rev.*, **110 (7)**, 699–706, https://doi.org/10.1175/1520-0493(1982)110<0699:SEITEO>2.0.CO;2.

Ogi, M., Y. Tachibana, and K. Yamazaki, 2003: Impact of the wintertime North Atlantic Oscillation (NAO) on the summertime atmospheric circulation. *Geophys. Res. Lett.*, **30 (13)**, 1704, https://doi.org/10.1029/2003GL017280.

Papin, P. P., 2017: Variations in Potential Vorticity Streamer Activity: Development Pathways, Environmental Impacts, and Links to Tropical Cyclone Activity in the North Atlantic Basin. Ph.D. thesis, 225 pp., State University of New York at Albany.

Papin, P. P., L. F. Bosart, and R. D. Torn, 2020: A feature-based approach to classifying summertime potential vorticity streamers linked to Rossby wave breaking in the North Atlantic basin. *J. Climate*, **33 (14)**, 5953–5969, https://doi.org/10.1175/JCLI-D-19-0812.1.

Patricola, C. M., S. J. Camargo, P. J. Klotzbach, R. Saravanan, and P. Chang, 2018: The influence of ENSO flavors on western North Pacific tropical cyclone activity. *J. Climate*, **(2018)**, https://doi.org/10.1175/JCLI-D-17-0678.1.

Patricola, C. M., P. Chang, and R. Saravanan, 2016: Degree of simulated suppression of Atlantic tropical cyclones modulated by flavour of El Niño. *Nat. Geosci.*, **9 (2)**, 155, https://doi.org/10.1038/NGEO2624.

Patricola, C. M., R. Saravanan, and P. Chang, 2014: The impact of the El Niño–Southern Oscillation and Atlantic Meridional Mode on seasonal Atlantic tropical cyclone activity. *J. Climate*, **27 (14)**, https://doi.org/10.1175/JCLI-D-13-00687.1.

Postel, G. A., and M. H. Hitchman, 1999: A Climatology of Rossby Wave Breaking along the Subtropical Tropopause. *J. Atmos. Sci.*, **56 (3)**, 359–373, https://doi.org/10.1175/1520-0469(1999)056<0359:ACORWB>2.0.CO;2.

Reynolds, R. W., N. A. Rayner, T. M. Smith, D. C. Stokes, and W. Wang, 2002: An improved in situ and satellite sst analysis for climate. *J. Climate*, **15 (13)**, 1609–1625.

Rios-Berrios, R., and R. D. Torn, 2017: Climatological analysis of tropical cyclone intensity changes under moderate vertical wind shear. *Mon. Wea. Rev.*, **145 (5)**, 1717–1738, https://doi.org/10.1175/MWR-D-16-0350.1.

Saunders, M., and A. Lea, 2014: Summary of 2013 Atlantic tropical cyclone season and verification of Authors' seasonal forecasts. Tropical Storm Risk, retrieved from https://www.tropicalstormrisk.com.

Saunders, M. A., P. J. Klotzbach, A. S. R. Lea, C. J. Schreck, and M. M. Bell, 2020: Quantifying the probability and causes of the surprisingly active 2018 North Atlantic hurricane season. *Earth Space Sci.*, **7 (3)**, e2019EA000 852, https://doi.org/10.1029/2019EA000852.

Scaife, A. A., and Coauthors, 2014: Skillful long-range prediction of european and north american winters. *Geophys. Res. Lett.*, **41 (7)**, 2514–2519, https://agupubs.onlinelibrary.wiley.com/doi/pdf/10.1002/2014GL059637.

Shaevitz, D. A., and Coauthors, 2014: Characteristics of tropical cyclones in high-resolution models in the present climate. *J. Adv. Model. Earth Syst.*, **6 (4)**, 1154–1172, https://doi.org/10.1002/2014MS000372.

Smith, D. M., and Coauthors, 2020: North Atlantic climate far more predictable than models imply. *Nature*, **583 (7818)**, 796–800, https://doi.org/10.1038/s41586-020-2525-0.

Storch, H. v. H. v., 1999: *Statistical analysis in climate research*. Cambridge University Press, Cambridge ;.

Strong, C., and G. Magnusdottir, 2008: How rossby wave breaking over the pacific forces the north atlantic oscillation. *Geophys. Res. Lett.*, **35 (10)**.

Takaya, Y., Y. Kubo, S. Maeda, and S. Hirahara, 2017: Prediction and attribution of quiescent tropical cyclone activity in the early summer of 2016: case study of lingering effects by preceding strong El Niño events. *Atmos. Sci. Lett.*, **18 (8)**, 330–335, https://doi.org/10.1002/asl.760.

Takaya, Y., T. Yasuda, T. Ose, and T. Nakaegawa, 2010: Predictability of the mean location of typhoon formation in a seasonal prediction experiment with a coupled general circulation model. *J. Meteorol. Japan. Ser. II*, **88 (5)**, 799–812, https://doi.org/10.2151/jmsj.2010-502.

Thorncroft, C., B. Hoskins, and M. McIntyre, 1993: Two paradigms of baroclinic-wave life-cycle behaviour. *Quart. J. Roy. Meteor. Soc.*, **119 (509)**, 17–55, https://doi.org/10.1002/qj.49711950903.

Trenberth, K., 2020: The Climate Data Guide: Niño SST indices (Niño 1+2, 3, 3.4, 4; ONI and TNI). National Center for Atmospheric Research, accessed 23 July 2020, https://climatedataguide.ucar.edu/climate-data/nino-sst-indices-nino-12-3-34-4-oni-and-tni.

Velden, C. S., and J. Sears, 2014: Computing deep-tropospheric vertical wind shear analyses for tropical cyclone applications: Does the methodology matter? *Wea. Forecasting*, **29 (5)**, 1169–1180, https://doi.org/10.1175/WAF-D-13-00147.1.

Villarini, G., G. A. Vecchi, T. R. Knutson, M. Zhao, and J. A. Smith, 2011: North Atlantic tropical storm frequency response to anthropogenic forcing: Projections and sources of uncertainty. *J. Climate*, **24 (13)**, 3224–3238, https://doi.org/10.1175/2011JCLI3853.1.

Vimont, D. J., and J. P. Kossin, 2007: The Atlantic meridional mode and hurricane activity. *Geophys. Res. Lett.*, **34 (7)**, https://doi.org/10.1029/2007GL029683.

Wang, C., 2004: ENSO, Atlantic climate variability, and the Walker and Hadley circulations. *The Hadley Circulation: present, past and future*, Springer, 173–202, https://doi.org/10.1007/978-1-4020-2944-8_7.

Wang, C., and S.-k. Lee, 2007: Atlantic warm pool, caribbean low-level jet, and their potential impact on atlantic hurricanes. *Geophys. Res. Lett.*, **34 (2)**, L02 703, https://doi.org/10.1029/2006GL028579.

Wang, C., Z. Song, F. Qiao, and S. Dong, 2010: What signals are removed and retained by using an anomaly field in climatic research? *Int. J. Oceanogr.*, **2009 (329754)**, https://doi.org/10.1155/2009/329754.

Wang, H., and Coauthors, 2014: How well do global climate models simulate the variability of atlantic tropical cyclones associated with enso? *J. Climate*, **27 (15)**, 5673 – 5692, //https:/doi.org/10.1175/JCLI-D-13-00625.1.

Wernli, H., and M. Sprenger, 2007: Identification and ERA-15 climatology of potential vorticity streamers and cutoffs near the extratropical tropopause. *J. Atmos. Sci.*, **64 (5)**, 1569–1586, https://doi.org/10.1175/JAS3912.1.

Wilks, D. S., 2011: *Statistical Methods in the Atmospheric Sciences*. Academic Press, 676 pp.

Williams, I. N., and C. M. Patricola, 2018: Diversity of ENSO events unified by convective threshold sea surface temperature: A nonlinear ENSO index. *Geophys. Res. Lett.*, **45 (17)**, 9236–9244, https://doi.org/10.1029/2018GL079203.

WMO, 2017: WMO guidelines on the calculation of climate normals. World Meteorological Organization Geneva, Switzerland.

Wood, K. M., P. J. Klotzbach, J. M. Collins, L.-P. Caron, R. E. Truchelut, and C. J. Schreck, 2020: Factors affecting the 2019 Atlantic hurricane season and the role of the Indian Ocean Dipole. *Geophys. Res. Lett.*, **47 (13)**, e2020GL087 781, https://doi.org/10.1029/2020GL087781.

Woollings, T., A. Hannachi, and B. Hoskins, 2010: Variability of the North Atlantic eddy-driven jet stream. *Quart. J. Roy. Meteor. Soc.*, **136 (649)**, 856–868, https://doi.org/10.1002/qj.625.

Woollings, T., B. Hoskins, M. Blackburn, and P. Berrisford, 2008: A new Rossby wave-breaking interpretation of the North Atlantic Oscillation. *J. Atmos. Sci.*, **65 (2)**, 609–626, https://doi.org/10.1175/2007JAS2347.1.

Zavadoff, B. L., and B. P. Kirtman, 2019: North Atlantic summertime anticyclonic Rossby wave breaking: Climatology, impacts, and connections to the Pacific Decadal Oscillation. *J. Climate*, **32 (2)**, 485–500, https://doi.org/10.1175/JCLI-D-18-0304.1.

Zhang, G., and Z. Wang, 2019: North Atlantic Rossby wave breaking during the hurricane season: Association with tropical and extratropical variability. *J. Climate*, **32 (13)**, 3777 – 3801, https://doi.org/10.1175/JCLI-D-18-0299.1.

Zhang, G., Z. Wang, T. J. Dunkerton, M. S. Peng, and G. Magnusdottir, 2016: Extratropical impacts on Atlantic tropical cyclone activity. *J. Atmos. Sci.*, **73 (3)**, 1401–1418, https://doi.org/10.1175/JAS-D-15-0154.1.

Zhang, G., Z. Wang, M. S. Peng, and G. Magnusdottir, 2017: Characteristics and impacts of extratropical Rossby Wave breaking during the Atlantic hurricane season. *J. Climate*, **30 (7)**, 2363–2379, https://doi.org/10.1175/JCLI-D-16-0425.1.

Zhang, R., and T. L. Delworth, 2006: Impact of Atlantic multidecadal oscillations on India/Sahel rainfall and Atlantic hurricanes. *Geophys. Res. Lett.*, **33 (17)**, https://doi.org/10.1029/2006GL026267.